Aakash Moncy

Mechanics of Cairo lattices

School of Engineering

Thesis submitted for examination for the degree of Master of Science in Technology.

Espoo 07.09.2017

Thesis supervisor and advisor:

Prof. DSc.(Tech) Luc St-Pierre

Aalto University
School of Engineering

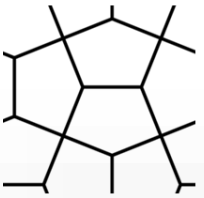

Mechanics of
Cairo lattices

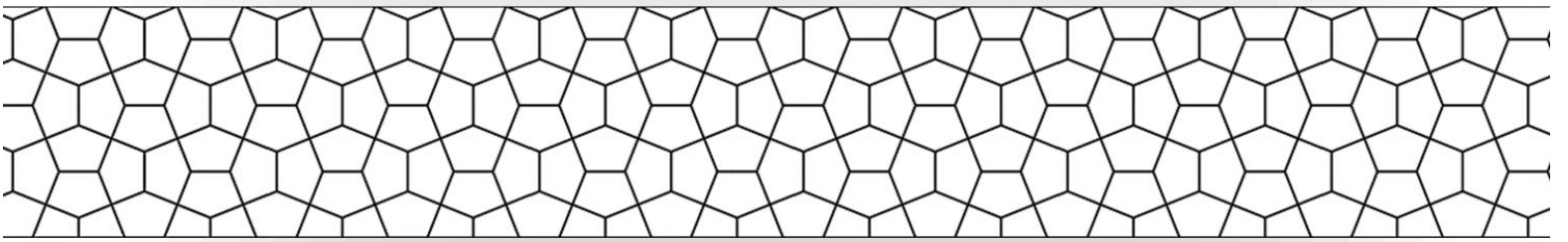

The universe it too big for a halt, never stop exploring.

AALTO UNIVERSITY
SCHOOL OF ENGINEERING

ABSTRACT OF THE
MASTER'S THESIS

Author: Aakash Moncy

Title: Mechanics of Cairo lattices

Date: 07.09.2017 Language: English Number of pages: 8+77

Department of Mechanical Engineering

Professorship: Mechanical Engineering Code: IA3027

Supervisor and instructor: Prof. DSc.(Tech) Luc St-Pierre

A tessellation made up of equal sided pentagons, called the Cairo lattice, is being investigated for its applicability as a structural 2D planar lattice. The strength and the stiffness for the infinite lattice has been formulated where the lattice is found to be *stretching* dominated under uni-axial stress fields. For any other type of external loading, the Cairo lattice is expected to be *bending* dominated. The analytical formulations have been verified with FE simulations of a unit cell. Experiments with 3D printed PLA specimens have been conducted on the finite Cairo lattice where the existence of strain producing mechanisms were discovered. A patching scheme is found to reverse the softened response of the finite Cairo lattice by inhibiting these strain producing mechanisms. A matrix method has been utilized for studying the states of *self-stress* and mechanisms to further investigate the rigidity of the Cairo lattice without patching. Under periodicity, the Cairo tessellation has a higher elastic buckling strength than the Kagome and the triangular lattice by 4.8% and 76% respectively. The Cairo lattice is also stronger than the diamond honeycomb, but has less stiffness compared to all these three tessellations.

Keywords: Cairo tessellation, Lattice materials, Cellular Materials, Finite Element Analysis, Additive Manufacturing, Mechanics and Structural Analysis

Acknowledgements

Just like the pillars of a building, there are a few people who have played a supportive role in the development of this thesis. Firstly I would like to express my gratitude to my supervisor, Prof. Luc St-Pierre for providing me with this opportunity and introducing me to lattice materials. I highly appreciate his sincere guidance and support throughout my thesis through weekly discussions. It always helped me clear my doubts and have a good vision for the upcoming week. Honestly, I couldn't ask for a better supervisor.

I also would like to thank my parents who have been always supportive during the entire project, Kim Widell for ensuring that I was able to complete the experiments at a very short notice, Tomas Their for helping me with the first 3D prints and finally Kalyani Avasak for providing me with important tips and especially introducing me to LaTeX - if anyone finds this thesis to look good, you are the reason behind it.

Aakash Moncy

Otaniemi, 07.09.2017

Contents

Symbols and abbreviations

Symbols

$\bar{\rho}$	Relative density
$\mathbf{A}$	Equilibrium matrix
$\mathbf{t}$	Vector of bar tensions
$\mathbf{f}$	Vector of external forces
b	Number of bars in a truss
j	Number of joints in a truss
k	Kinematic constraints
$\mathbf{B}$	Kinematic matrix
$\mathbf{d}$	Vector of displacements
$\mathbf{e}$	Vector of bar elongations
s	Number of states of *self-stresses*
m	Number of inextensional mechanisms
r	Rank of the equilibrium matrix
Z	Joint connectivity
S	An element of the compliance matrix
E	Youngs modulus [MPa]
ν	Poisson's ratio
G	Shear modulus [MPa]
ϵ	Strain
σ	Stress [MPa]
u	Displacement [mm]
P	Axial force for the virtual work derivation [N]
A	Cross-section area of the struts [mm^2]
M	Bending moment for the virtual work derivation [N·mm]
V	Shear force for the virtual work derivation [N]
I	Moment of inertia [mm^4]
l	Length of each strut [mm]
t	Thickness of each strut [mm]
h	Out of plane thickness of the strut [mm]
T	Force [N]
R	Reaction forces in the struts [N]
T_{crit}	Euler's critical buckling load [N]

Abbreviations

2D	2 Dimensional
3D	3 Dimensional
FE	Finite Element analysis
AM	Additive Manufacturing
FDM	Fused Deposition Modeling
CAM	Computer Aided Manufacturing
SLS	Selective Laser Sintering
SLM	Selective Laser Melting
DMLS	Direct Metal Laser Sintering
EBM	Electron Beam Melting
SHS	Selective Heat Sintering
UAM	Ultrasonic Additive Manufacturing
LOM	Laminated Object Manufacturing
PLA	Polylactic acid
NLGEOM	Non-Linear Geometry
CAE	Computer Aided Engineering
PCL	Polycaprolactone
PA	Polyamide

1 Introduction

Materials are everywhere. At any given time, if you look around, you would realize that you are in an exhibition for materials - comprising of metals, ceramics, glass, plastics etc. Let alone finding naturally occurring materials, we as the most intelligent species to be on Earth in known history, have learned to engineer new materials on our own. A recent example is the Boeing 787 Dreamliner which has its airframe and various other primary structures made out of composite materials, thus helping the aircraft save 20% of its weight when compared to the more conventional aluminium designs.

The thesis starts with a brief history of materials, appreciating the important discoveries in material research. With this thesis an attempt is made to learn more about the future of materials.

1.1 History of materials in brief

The earlier known materials were more commonly devoted to making tools and weapons. About 300,000 or more years ago, bones and stones were used to suffice this purpose. Human civilization began flourishing and even more exotic metals were started to be discovered. Gold and Silver were unearthed, and they were found to be ductile, which meant that they could be beaten into intricate shapes. By 4000 BC, it was learnt that metals could be melted and casted, leading to the development of exotic ornaments. The introduction of furnaces by 3500 BC helped implement copper for manufacture weapons. Around 3000 BC, *bronze* was born due to the accidental inclusion of tin based mineral, *cassiterite* in copper ores. But, around 1450 BC, bronze gave way to iron for its greater stiffness, strength and hardness.

At around AD 1500, the introduction of the blast furnace led to the widespread use of cast iron. Before, casting of iron was difficult as it requires a temperature of about 1600°C. During the industrial age, cast iron helped build bridges, railway and civil buildings. It was during the 1940's and 1950's the demand of aircraft's increased due to the prevailing World War II and a subsequent demand of lightweight materials were born.

Emphasis shifted to lightweight alloys like Aluminium and even materials which could withstand high temperature like Titanium. Not long after, super alloys were introduced. They are heavily alloyed iron, nickle and cobalt based materials which have the capability of withstanding temperatures as high as 1200°C.

More recently, Silicon has made a revolution in the electronics industry and modern computer science. Also, the field of biomaterials is growing rapidly in the last two decades mainly as implant materials. There is also the modern avatar of nanotechnology which has been born due to the discovery of various forms of carbon such as the C60 molecule and carbon nanotubes. Today, there is a lot of interest in understanding how nature builds materials where new technologies are being used to replicate the process, molecule by molecule, thus trying to make them far more better - such that machines and structures in which they are used can venture into applications never thought before.

1.2 Dawn of engineered lightweight materials - composites

Wood always was used for construction purposes as they were naturally occurring lightweight material capable of carrying significant loads as compared to any materials available hundreds of years ago. They were used to build ships and houses. But fast forward to the twentieth century, the very idea of lightweight materials was about to change because the polymer revolution was about to happen - *Bakelite* and synthetic butyl rubber were developed in 1909 and 1922 respectively.

Polymer science flourished. The biggest success includes polypropylene, polyethylene, polyvinyl chloride and polyurethane. And soon the age of composites dawned. Polymeric fibres which other wise lacked stiffness in the transverse direction, now when reinforced with a matrix material, had the capability of being far stronger and very lightweight. The major advantage of composites was to engineer the material based on the loads it should sustain. But the idea of composite is not a knew one, as steel-reinforced concrete was being used long before composites, for civil construction purposes, but they were not lightweight.

Carbon fibres lead to a bigger revolution than the previously engineered glass fibres, but that came with added costs. Even though they have very high stiffness and strength per unit weight, their cost made them possible to be used only in select applications like high performance sports equipments, the *Formula One* racing cars or in the aerospace industry to name a few.

1.3 Overview of the material space

All the materials known to us can be plotted on material property charts, the most popular being for stiffness and strength. Figure 1 shows a material property chart for strength as an example. The material charts have places which are filled with materials and places which are empty. Though, its difficult to fill all the empty places, but an attempt is being made to fill as much as possible. There are three possible ways with which the spaces could filled as narrated by Fleck et al. [2] - using *chemistry* where new alloys, polymers and composites are made; manipulation of *micro-structure* where the distribution of phases and defects within a material is controlled; and with *architecture* where micro-trusses are manufactured based on a certain tessellation.

For lightweight materials, the requirement is to have lesser density but higher strength, hence in Figure 1 we could see that composites which are widely used in the aerospace industry are lighter than metals (hence to the left of metals), but stronger than other lightweight materials such as foams and polymers (hence above them).

1.4 Lattice materials/Micro-truss materials

. The law of nature as we known it - 'Survival of the fittest', has finally made its way in materials, where we are now taking inspiration from tessellations occurring naturally. It has been observed that these tessellations like the solid component of

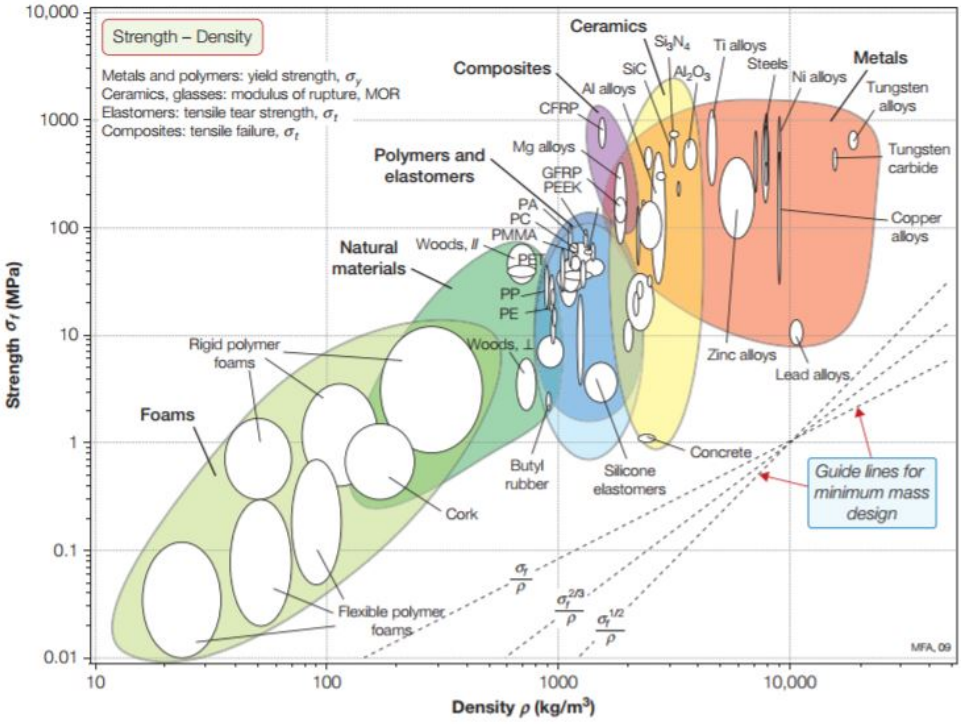

Figure 1: Material property chart for strength [17].

wood (a composite of cellulose, lignin, and other polymers) are prismatic shaped because during their evolution over centuries, the tress have optimized themselves for stiffness and strength [17].

Some of the most commonly found microscopic shapes in nature is seen in Figure 2. All of these shapes have one common trait, they are optimized for mechanical efficiency.

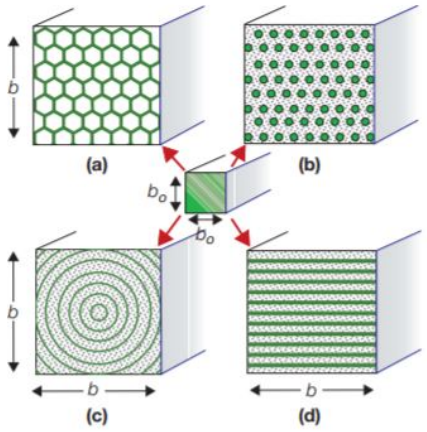

Figure 2: (a) Prismatic cells, (b) Fibers in a foamed matrix, (c) Concentric cylindrical shells and (d) Parallel plates separated by foamed. [17]

One of the most commonly seen tessellation is the hexagonal honeycombs which are increasingly being used as the core of sandwich panels. But such 2D and periodic structures are the strongest when they are loaded in the out-of-plane direction. It is of high research interest to study the in-plane properties of the tessellations as they are believed to be the biggest hurdle for a lattice material to be widely accepted.

1.5 Scope of this study

The aim of this thesis is to explore the mechanics of a unique tessellation made up of *equal-sided* pentagons, more commonly known as the Cairo tessellation (Figure 3). The strength and the stiffness of this lattice would be developed analytically and compared with the Finite Element (FE) simulation results. Experiments are carried out to verify the findings and finally the mechanics is compared with the other commonly used tessellations for structural applications.

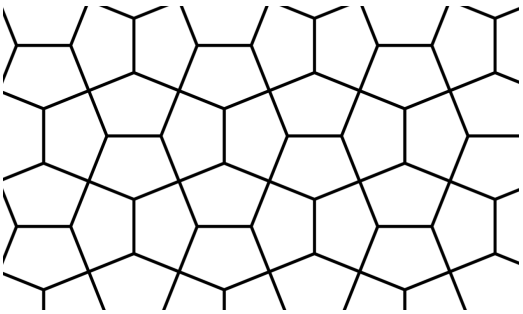

Figure 3: The Cairo tessellation.

The research questions to be answered are:

- Is the Cairo tessellation *stretching* dominated or *bending* dominated?
- How does the tessellation perform when compared with other commonly used tessellations?
- Does being a non-*similarly situated* topology have a significant effect on the mechanics? If yes, is it an improvement or degradation?
- Can today's low cost 3D printers used generally for prototyping, be used for printing lattice tessellations for structural applications?

2 Reviewing existing literature

Cellular materials are unique in nature as their geometry greatly influences its macroscopic properties. In the last few decades a lot of research has been carried out with the aim of finding the geometry which provides one with great stiffness and strength, but at the same time be very lightweight. In this chapter, lattice materials and the important terminologies associated with them have been introduced. In addition, the rigidity of finite trusses is reviewed and extended to infinite trusses, the Cairo tessellation is presented, the work on existing topologies is discussed and finally some of the research already conducted in 3D printing of lattice materials is explored.

2.1 Foundations of cellular materials

Cellular materials are nothing but porous materials. They can be divided into two main types - lattice materials and foams. The former are *architectured* micro-trusses which can be 2D or 3D (e.g. hexagonal honeycombs) and the latter are irregular 3D structures (e.g. sponge) most commonly modelled on the Voronoi diagram (Figures 4 and 5). The main focus would be on the lattice materials for this thesis.

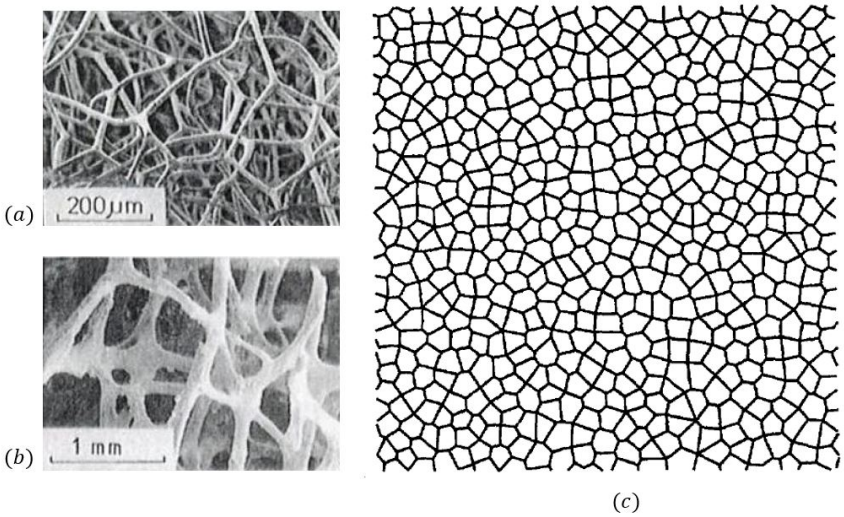

Figure 4: Naturally occurring cellular materials (a) sponge and (b) cancellous bone [3].; (c) Voronoi cells [43].

To categorize any type of cellular material, the most important parameter is the *relative density*, $\bar{\rho}$. It is basically the ratio of the foam density to the density of the solid from which the cellular structure is made. For lattice materials they are formulated in terms of the thickness t and the length l of the struts. It is represented as,

$$\bar{\rho} = A \cdot \frac{t}{l} \tag{1}$$

Where A is a constant which would be determined in Chapter 3 for the Cairo tessellation.

Lower the relative density, lighter is the structure and thinner are the members, if the length of all the members remain unchanged. Cellular structures rarely depend on the *cell size* but the *cell shape* matters more. *Connectivity* of the structure i.e. the number of members meeting at a node has been proven to have a profound effect on the mechanics of lattices [5].

2.1.1 Classification of lattice materials

The lattice materials can be classified based on the topology and also based on the deformation mechanism. For the former, the lattice material are categorized as *regular*, *semi-regular* and *others* (Figure 5). *Regular* lattices such as the hexagonal honeycombs, triangular honeycombs and square honeycombs, as their name suggests use regular polygons - hexagons, triangles and squares (with equal sides and equal internal angles) respectively. In *semi-regular* lattices, more than one regular polygons are used, such as the Kagome lattice. The *regular* and the *semi-regular* lattices are made to have the same nodal connectivity. Finally, all the remaining possible tessellations are classified under *other* lattices. The Cairo tessellation falls in the *other* category.

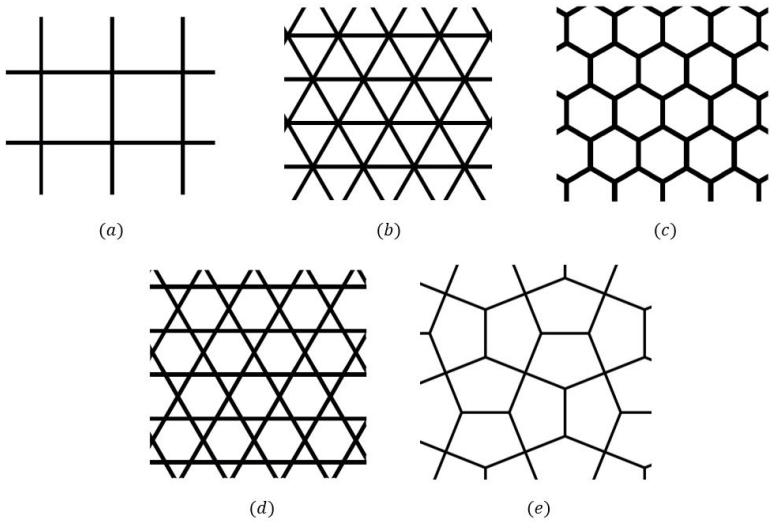

Figure 5: The *regular* lattices are honeycombs of (a) Square, (b) Triangle and (c) Hexagon [42].; An example of *semi-regular* lattice is (d) Kagome [42].; An example of *other* lattice is (e) Cairo.

Also, based on the deformation mechanism, lattice materials could be classified into two groups, namely, *stretching* dominated and *bending* dominated. In the former, the lattice is expected to deform by axial extension or compression of all its members and in the latter the members undergo bending.

2.1.2 Stress-Strain response of lattices

The cell walls of lattice materials are very thin and are treated as beam or a column as a result of which simple beam theory can be implemented to derive the mechanical

properties of lattice materials with periodic unit cells. Timoshenko's beam theory is a good starting point to explore the mechanics. Wang et al.[1] studied the mechanics of seven different cell types to determine their in-plane stiffness and strength. It was found that the hexagonal honeycomb cells undergo cell wall bending while the triangular honeycomb undergo cell wall stretching. This makes the former *bending* dominated and the latter *stretching* dominated.

In general, the in-plane compression stress-strain response of a lattice material is characterized by mainly three regions. *Region I* is dominated by linear elasticity, *Region II* can be a plateau or exhibits post yield softening due to the onset of plasticity in one or members and *Region III* represents densification due to the cells walls touching each other at very high strains.

Though the *Region I* and *Region III* are no different for *stretching* and *bending* dominated lattices, it is the *Region II* which helps us in understanding the failure mechanism that the lattice has undergone. For *bending* dominated lattices, the structure collapses with a nearly constant stress. The lattice at the end of *Region I* can either undergo plasticity, buckling or fracture. The failure mechanism which requires the least stress, takes place. A typical response for *bending* dominated lattice is shown in Figure 6a.

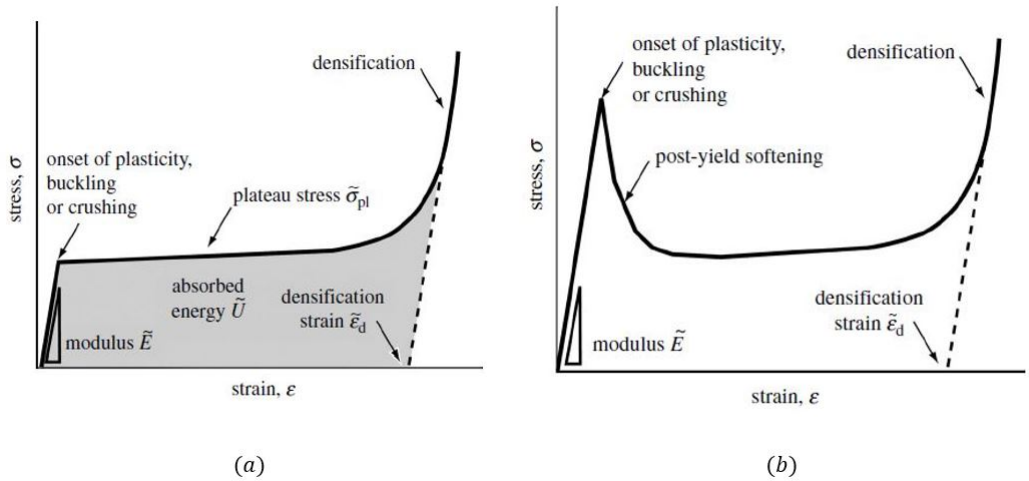

Figure 6: A typical stress-strain response of a (a) *bending* dominated lattice and (b) *stretching* dominated lattice [18].

A typical response of *stretching* dominated lattices is shown in Figure 6b. Unlike the *bending* dominated response, the lattice here does not have a constant stress in *Region II*. Elastomeric materials undergo elastic buckling, metals either undergo elastic buckling or plastic buckling (depending on the relative density) and brittle materials undergo crushing under uni-axial compression.

Even though the elastic modulus and the initial collapse strength of the *stretching* dominated lattices are greater than *bending* dominated lattices, both of them have there own good applications. The *stretching* dominated lattices are much preferred in structural applications while the *bending* dominated lattices are preferred as energy absorbers.

2.2 *Stretching* and *Bending* dominated lattice materials

With the extensive research already carried out on the various cell topologies, it is with great confidence one could define the stiffness and the strength of *stretching* and *bending* dominated lattices as [9],

$$Stretching\ dominated \begin{cases} Strength \propto \bar{\rho}^1 \\ Stiffness \propto \bar{\rho}^1 \end{cases}$$

$$Bending\ dominated \begin{cases} Strength \propto \bar{\rho}^{1.5} \\ Stiffness \propto \bar{\rho}^2 \end{cases}$$

Looking at the above relations and subsequently carrying out a simple calculation leads to the result that, for a relative density of 0.1, the *stretching* dominated lattices are 10 times stiffer and approximately 3 times stronger than the *bending* dominated lattices. These difference are more prominent at very low relative densities but as the relative density approached unity, the differences vanish as we now have a continuum solid material.

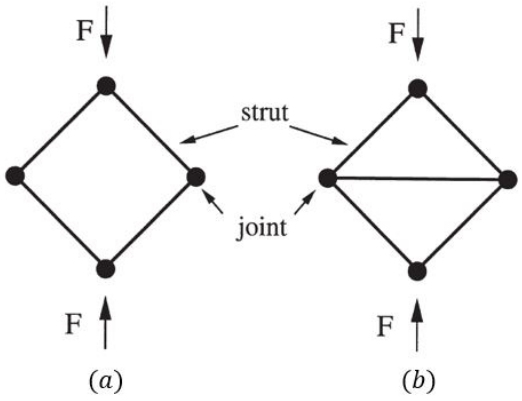

Figure 7: (a) A mechanism and (b) A structure [5].

As stated earlier, a *stretching* dominated lattice primarily has only pure axial deformation and *bending* dominated lattice deforms by bending of the struts. As an example, if a frame with pin-joints shown in Figure 7a is considered, it can easily collapse under a force F, without offering any resistance to motion. Whereas the frame in Figure 7b is a structure as the struts have the capability of sustaining the force F by virtue of inducing axial forces (tensile or compressive) within the struts. Now if the joints are considered to be rigid, for the first frame, the loading would induce bending moments at the joints, making the struts themselves bend. But the second frame would still induce axial forces like in the previous case. Thus the rigid jointed frame in Figure 7a is a *bending* dominated structure, and the latter frame is

stretching dominated structure. The second frame is insensitive to the type of joints. Therefore, for the analysis of *stretching* dominated lattices, one could approximate a rigid structure to be a pin jointed structure for calculating the forces in the members as the analysis then becomes simpler.

2.3 Rigidity of lattice materials

In order to analytically evaluate the performance of a lattice under a certain macroscopic stress field, the lattice is considered as a network of interconnected members with pin-joints for simplicity. But it is known that in reality, the lattices neither are completely rigid-jointed nor completely pin-jointed [4], rather have *nearly* rigid joints. But pin-joints are a good consideration for the structural analysis of the micro-truss especially for *stretching* dominated lattices. For *bending* dominated lattices, the bending moments of the struts about the *nearly* rigid joints have to be considered.

Initially, the rigidity of finite trusses are revisited and the concepts are extended to infinite trusses. Since a lattice tessellation is nothing but a truss, the existing concepts of finite trusses prove to be quite useful for developing its mechanics. But for theoretical analysis, the lattice is also considered to be infinite. With the help of this assumption, if a unit cell for a certain tessellation is assumed, the effect of the surrounding infinite lattice is taken into consideration as periodic boundary walls of the unit cell. Thus, periodicity along with truss analysis are used together for developing the mechanics of infinite Cairo lattices.

2.3.1 Finite trusses

For a finite truss with b bars and j joints to be rigid, it has to be *statically* determinate, where the axial forces in the members should be able to be defined solely from the equilibrium equations depending on the external forces applied to it. This implies that the number of known equilibrium equations are equal to the number of unknown forces. A truss is said to be in *kinematic* determinate if the location of all the nodes can be determined by the length of the members. Thus, by Maxwell, for a 2D structure to be *statically* and *kinematically* determinate, a *necessary* but not a *sufficient* condition is [6],

$$b - 2j + 3 = 0 \tag{2}$$

A truss is *statically* indeterminate, if now an extra bar is added to the already *statically* determinate structure, such that a state of *self-stress* is generated. An easier way of imagining this would be to consider the extra bar to be shorter or longer than required. Thus to make the extra bar fit between two joints, it will induce a state of stress within itself. These joints itself will induce further forces to the immediate members connected to them. Thus, there is a set of internal forces in static equilibrium with zero external nodal forces.

Figure 8 shows a clear example between static determinacy and indeterminacy. If the pin jointed structure only has four members (Figure 8a), Maxwell's rule for

rigidity is not satisfied and the structure is a *mechanism* or *statically* unstable. In Figure 8b, an addition of a diagonal member makes the Maxwell rule valid for the structure to be rigid. Indeterminacy creeps in if an additional diagonal bar is imagined to be present (Figure 8c). If this additional bar is longer or shorter than required, then there would be a state of *self stress*. But, the Maxwell's rule, (Equation 2), does not show the number of states of *self-stress*, s and *mechanisms*, m, which are quite essential in structural analysis.

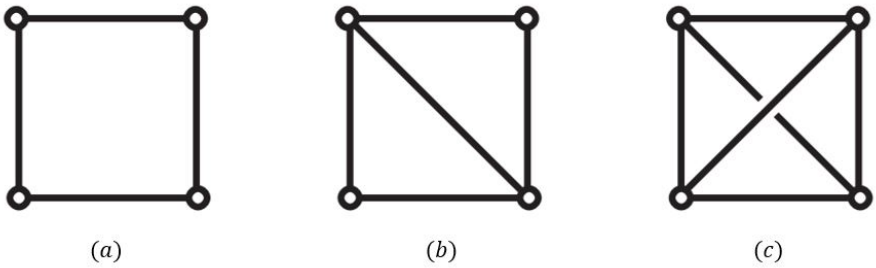

Figure 8: (a) *Statically* unstable, (b) *Statically* determinate and (c) *Statically* indeterminate structure.

Pellegrino and Calladine [7] devised a generalised Maxwell's rule where m and s are related to the rank r of an *equilibrium* matrix $\mathbf{A}$, for a 2D case as,

$$s = b - r \tag{3}$$

$$m = 2j - k - r \tag{4}$$

and,

$$s - m = b - 2j + k \tag{5}$$

For the analysis of static determinacy, an *equilibrium* matrix $\mathbf{A}$ is introduced [7] which basically houses information about the distances between the joints in a truss. Again, a truss with j joints, b bars and k kinematic constraints to rigid foundations; would also give us a vector $\mathbf{t}$ of bar *tensions* and a vector $\mathbf{f}$ of *external force*. The size of the matrix $\mathbf{A}$, vector $\mathbf{t}$ and vector $\mathbf{f}$ are $(2j-k) \times b$, $b \times 1$ and $(2j-k) \times 1$ respectively, for a 2D case. These terms are related as,

$$\mathbf{A} \cdot \mathbf{b} = \mathbf{f} \tag{6}$$

Similarly, the kinematic conjugate is given by,

$$\mathbf{B} \cdot \mathbf{d} = \mathbf{e} \tag{7}$$

where $\mathbf{B}$ is the *kinematic matrix*, $\mathbf{e}$ is a vector with bar *elongations* and $\mathbf{d}$ is a vector with *displacement* components. Their sizes are $b \times (2j-k)$, $b \times 1$ and $(2j-k) \times 1$ respectively for a 2D case.

Further with virtual work, we have,

$$\mathbf{B} = \mathbf{A}^T \tag{8}$$

The information of s and m is basically found in the *four fundamental vector subspaces* of the *equilibrium matrix* $\mathbf{A}$ (Table 1).

Name	Dimension
Rowspace of $\mathbf{A}$	r_A, rank of $\mathbf{A}$
Nullspace of $\mathbf{A}$	s
Coloumn space of $\mathbf{A}$	r_A, rank of $\mathbf{A}$
Left Nullspace of $\mathbf{A}$	m

Table 1: Fundamental vector subspaces of the *equilibrium* matrix $\mathbf{A}$.

The Rowspace and the Nullspace of $\mathbf{A}$ belong to the bar space b. The Coloumn space and Left Nullspace of $\mathbf{A}$ belong to the joint space *(2j-k)* for a 2D case. The generalized Maxwell's rule (Equation 5) gives a far better picture on the rigidity of finite trusses than the Maxwell's original rule itself (Equation 2). The matrix analysis helps in further drawing a more accurate conclusion about a lattice either being *stretching* or *bending* dominated based on their rigidity.

2.3.2 Infinite trusses

For periodic trusses, Maxwell's rule can be extended to define *nodal connectivity, Z*. Deshpande et al. [5] found that the minimum connectivity in *similarly situated* planar lattices which is *necessary* for rigidity is $Z = 4$. This number was reached, when the average number of bars in a lattice which is formulated as $\approx jZ/2$ is used with Equation 5, where $k = 0$ in case of periodicity and $s - m = 0$ for *statical* and *kinematical* determinacy. *Similarly situated* truss implies that the truss appears to be same when viewed from any joint, like the fully triangulated planar truss, for which Z takes the value of 6. With this a conclusion was made by Deshpande et al. that $Z = 4$ for 2D lattices is the *necessary* condition but not a *sufficient* condition for rigidity. But $Z = 6$ for 2D lattices is the *necessary* and *sufficient* condition for rigidity. In other words with a $Z < 4$, the infinite lattice is expected to be *bending* dominated, with $4 \leq Z < 6$, the lattice can be either *stretching* or *bending* dominated, and with $Z \geq 6$ the infinite lattice is *stretching* dominated.

The matrix method introduced by Pellegrino and Calladine can be extended to periodic trusses to further evaluate its rigidity, but their direct usage ends with the determination of the number of states of *self-stress* and mechanisms. The states of *self-stress* in the infinite lattice suggests the type of stress fields a lattice could sustain [8]. Also, the mechanisms calculated from the matrix analysis are in-fact periodic mechanisms which do not induce macroscopic strains in the lattice. These periodic mechanisms are also called *in-extensional* mechanisms. If the lattice is *stretching* dominated, the collapse takes place with periodic mechanisms and if the lattice is *bending* dominated, the collapse is macroscopic strain producing [4]. Guest

and Hutchinson [8] has shed more light on the usage of the matrix **A** and **B** in *similarly situated* periodic trusses by the statics and kinematics approach, as well as stated that an infinite lattice cannot be simultaneously *statically* and *kinematically* determinate at the same time.

Since the Cairo tessellation is not *similarly situated*, these conclusions cannot be directly utilized. But, the matrix analysis with the determination of the states of *self-stress* and mechanisms can be implemented to study the rigidity on its own.

2.4 Developing the mechanics of lattice materials

There is a lot of research available today on lattice materials, some of which has positively contributed to this thesis. It has been observed, that with the advancement in FE solvers and computer processors, it has become easier today for researchers to numerically study the various possible lattice tessellations.

In 1981, Gibson [3] for her PhD thesis at the University of Cambridge developed the mechanics of hexagonal honeycomb lattices and verified them with experiments. It was shown that the hexagonal honeycomb is *bending* dominated. Taking the example of hexagonal honeycombs, Ashby et al. [23] stressed on the influence of nature to desire optimal lightweight materials. Warren et al. [25] further made a conclusion that nature settles with a morphology which minimizes the surface energy and prefers bending to be the dominant deformation mechanism. They worked on a theoretical model for the linear elastic response of 2D and spatially periodic lattices in simple shear and pure strain. The hexagonal symmetry used for their analysis had varying thicknesses along its length.

Overaker et al. [22] later proved that the relative density of the hexagonal honeycomb is subjective to the unit cell morphology, and changes with the orientation of the struts. Chen et al. [26] studied the elastic moduli of honeycombs with asymmetrical hexagonal cells and concluded that in order to calculate the equivalent elastic moduli, one needs to take into consideration shear deformation along with bending and tensile deformation. An interesting research question is about the effect of slight changes to a tessellation on its mechanics. As an example, Tantikom et al. [30] studied the in-plane compression of a hexagonal close-packed structure analytically and experimentally. The effect of the contact between the adjacent circular topology, in terms of the ratio of contact radius to the wall thickness was studied over the deformation mechanism.

One of the earliest summarization of *stretching* and *bending* dominated behaviour of 2D and 3D lattices is found in a research paper by Christensen [21]. He discusses the mechanical properties for stiffness and strength, and presents an open question for future work which deals with finding the optimal topology. Wang et.al. [1] made a good comparison of the mechanical properties of various honeycombs such as square, hexagonal, triangular, Kagome and diamond to name a few. The results from their research helps in differentiating the methodology towards their mechanics which makes them either *stretching* or *bending* dominated lattices. Deshpande et al. [29] studied the mechanics of the octet-truss lattice analytically, with FE analysis and experimentally. The octet-truss has a connectivity of 12 which acts as the

sufficient condition for *stretching* dominated behaviour in 3D.

With the advancement of FE methods, the mechanics of the hexagonal honeycombs were further studied where Chen et al. [34] showed that for in-plane uniaxial compression with finite boundary conditions there are two behaviours namely Type I and Type II which are characterized by the wall thickness, the strain-hardening coefficient and the yielding stress. Also, Tankasala et al. [35] studied the tensile behaviour of triangular, Kagome, hexagonal and diamond honeycombs using FE analysis. With FE, new tessellations are being investigated where as an example Zhang et al. [33] developed the mechanics of N-Kagome and SI-square lattice.

In finite lattices, the mechanics is strongly effected by imperfections or deformation instances which are otherwise not present in infinite lattices. Grenestedt [24] showed that imperfections such as waviness influence the properties of cellular materials by degrading their elastic stiffness. Also, Chen et al. [36] studied the role of imperfections like waviness, non-uniform cell wall thickness, cell-size, fractured walls, misalignment's and missing cell walls on the yielding behaviour of 2D honeycombs. It has been observed that such imperfections can make a *stretching* dominated lattice become *bending* dominated. Phani et al. [32] investigated the presence of an elastic boundary layer in finite lattices. This layer is basically a localized elastic deformation taking place at the free edges of the lattice.

2.5 The Cairo tessellation

Cairo tessellation is a five point geometrical pattern based on pentagons, otherwise also called Cairo pentagonal pattern because of its origins in Egypt. It has been realized that such a tessellation has not been investigated as a potential geometry for a lattice material. But certainly among architects, the Cairo tessellation is of great interest with respect to modern design.

There are many ways of generating the Cairo pentagon [37] and all of the ways have their unique differences in the terms of the strut length or the angles made inside the pentagon. For this thesis, only one method is adopted to create the geometry for which the strut lengths are equal and the internal angles of the inclined struts are 24.3° and 114.3° with the horizontal (Figure 9).

2.6 Mechanical and material properties

The Cairo lattice is orthotropic, which implies that the appearance of the structure remains unchanged if it is rotated by 180° about its three orthogonal axes. For a 2D cellular material, Gibson [3] has put forth that the stiffness in the out-of-plane direction and the resistance to shears ϵ_{32}, ϵ_{31} are very great (X1,X2 are in-plane orthogonal axes and X3 is the out-of-plane axis). Also, the cellular material is assumed to undergo negligible contraction or extension when the stress field is along the X1 or X2 direction. Thus, the elastic constants required for the mechanics of the Cairo are - E_1, E_2, G, υ_1 and υ_2. Here E_1 and υ_1 are the Young's modulus and Poisson's ratio when the Cairo lattice is loaded in the X1 direction. Similarly, E_2 and υ_2 are the elastic constants when the lattice is loaded in the X2 direction. But

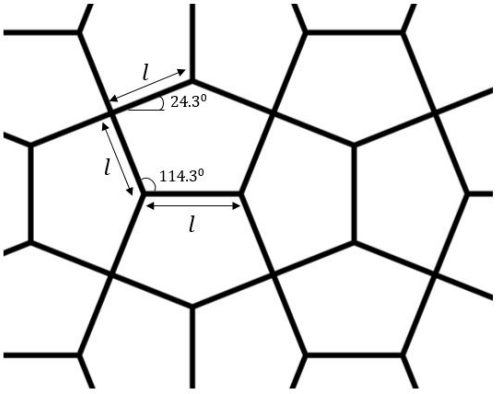

Figure 9: The Cairo tessellation with the features of the pentagon.

due to orthotropy, $E_1 = E_2$ and $\upsilon_1 = \upsilon_2$. G is the shear modulus in the X1-X2 plane.

For a lattice, the stiffness in the X1 and the X2 direction is presented as,

$$\frac{E_1^*}{E_s} = \frac{E_1^*}{E_s} = B\bar{\rho}^b \tag{9}$$

The strength in the X1 and the X2 direction is presented as,

$$\frac{\sigma_1^*}{\sigma_{ys}} = \frac{\sigma_2^*}{\sigma_{ys}} = C\bar{\rho}^c \tag{10}$$

Where B, C, b and c are the constants which would be determined in the next chapter for the Cairo lattice; σ_{ys} and E_s are the yield strength and the Youngs modulus of the solid material respectively.

In this thesis, the solid material of the members, is considered to be *linear elastic-perfectly plastic*. This implies that no strain-hardening is taken into consideration. The stress-strain response of such a behaviour is shown in Figure 10.

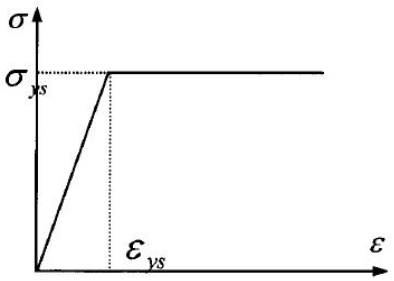

Figure 10: Linear elastic-perfectly plastic behaviour exhibited by the solid material with which the members of the Cairo lattice is made.

2.7 3D Printing - a key to the future

Additive Manufacturing (AM), or more commonly called as 3D printing, is a fairly recent production process which is gaining greater acceptance with every iteration of the technology, especially among designers for prototyping. The drivers behind this growing field is the production of complex software codes and the rapidly declining prices of electronics. The greatest advantage of this technology is in prototyping, where an object can be viewed in all its glory from the 3D modelling software and can be printing directly without the involvement of laborious work. 3D printing involves 8 main steps, right from developing the Computer Aided Drafting (CAD) model to the final product in hand (Figure 11).

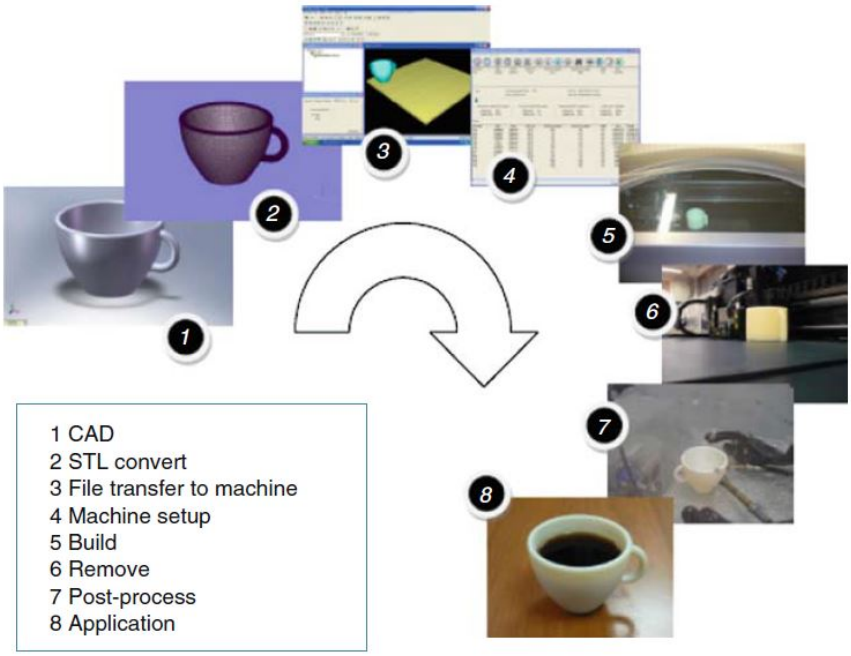

Figure 11: Stages in the 3D printing process [10].

2.7.1 Different types of 3D printing techniques

There are many factors affecting the selection of the suitable method for printing the specimen like cost and material. Some of the most commonly used methods have been present briefly below [20].

- **Vat Photopolymerization**
  With this method, a liquid photopolymer is kept in a vat and undergoes hardening due to the ultraviolet rays (UV) incident on it. This technique is more commonly termed as Sterolithography (SLA). The operation takes place in layers, such that after each layer, the platform on which the object is being printed, moves down by a layer distance to accommodate the next layer. Each layer corresponds to a cross-section of the object. This technique was invented by Charles Hull in 1986.

- **Material Jetting**
  In this technique, inkjet print heads makes the material available in the form of droplets on a built platform and makes use of UV light to harden the liquid droplets, thus slowly contributing towards the final object.

- **Binder Jetting**
  Here there are two materials used - one for the parent material in powder form from which the object is supposed to be made and the second material in liquid form which basically acts like a binder for the powder. A layer of powder is spread on the build plate and the liquid binder binds the powder material together based on the cross-section of the object. After the printing process, the loose powder is removed, thus leaving us with the finished product. But the loose powder can be reused for the next printing process. This method was first developed at Massachusetts Institute of Technology (MIT) in 1993.

- **Fused Deposition Modeling (FDM)**
  In this thesis we would be using the FDM method to manufacture the lattice for experiments. The method basically has the polymer rolled up in a reel, which is fed to a nozzle at an elevated temperature. The nozzle melts the polymer and lays it on to the build plate. But soon after exiting the nozzle, the polymer solidifies again. the travel of the nozzle can be programmed by any computer-aided manufacturing (CAM) software in the form of a G-code which holds the information about the co-ordinates in space.

- **Powder Bed Fusion**
  There are many techniques under this category, namely, Selective Laser Sintering (SLS), Selective Laser Melting (SLM), Direct Metal Laser Sintering (DMLS), Eletron Beam Melting (EBM) and Selective Heat Sintering (SHS). But the most commonly used method is SLS where a laser selectively sinters the material (plastic, metal, ceramic or glass) in their powder form, layer by layer. After a layer is completed, a new layer of powder is added to the build plate on top of the previous layer by lowering the build plate itself. The powder which is not sintered act as the support structure for the object, which is believed to be a very big advantage over the other methods like FDM or SLA. Also, this powder can be reused for next printing process. The process seems quite similar to Binder Jetting, but instead of having a liquid binder, we have a laser.

- **Sheet Lamination**
  The process deals with joining sheets of a certain material together with certain external mediums, thus creating the final object. There are two main types, namely, Ultrasonic Additive Manufacturing (UAM) and Laminated Object Manufacturing (LOM). In UAM, the sheets are made up of metals which are bound with the usage of ultrasonic welding. The commonly used metals include aluminium, copper, stainless steel and titanium. In LOM, the process remains similar, but the sheets are made up of paper and instead of using welding, an adhesive glue is used.

- **Direct Energy Deposition**
  This process is mostly used in the metal industries where a multi-axial robotic arm deposits the metals in the form of a powder or wire onto a build plate and subsequently an energy source which either can be a laser, electron beam or plasma, melts it.

2.7.2 3D printing of lattice materials

There have been various attempts in 3D printing of lattice materials with the usage of Vat Polymerization, Powder Bed Fusion (especially SLS) and FDM methods. 3D printing of cellular materials without any defects is quite difficult to achieve because of the very thin members or features. Thus, the current limitations of the 3D printers with respect to the printing quality at that minuscule size level often leads to irregularities in the structure.

Limmahakhun et al. [11] used Vat Polymerization and SLS for 3D printing the cellular structures. They found the former to be more accurate with required porosity as compared to the latter in their samples for bone tissue engineering. The polymer was composed of urethrane oligomers which required supporting structures which were made of hydroxylated wax. Cahill et al. [14] also made an attempt to employ SLS for printing polyamide (PA) and polycaprolactone (PCL) scaffolds for bone tissue engineering where they managed to print an open structure having strut diameters as low as 350 μm for the PA scaffold and 431 μm for the PCL scaffold (Figure 12). An FE comparison was done for the experimental results in which like Limmahakhun et al. [11], it was found that the mechanical properties were affected by the irregularity in the diameter of the printed struts, presence of unwanted micropores and surface roughness.

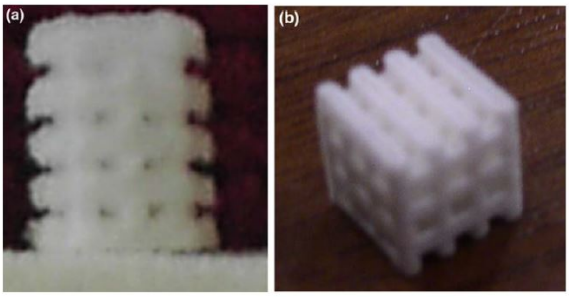

Figure 12: (a) PCL sample made from SLS technique and, (b) PA sample made from SLS technique [14].

The FDM printing technology has provided more opportunities for research, which are just not limited to the technique itself. Compton et al. [12] has put forward a fibre-filled epoxy ink for FDM based printers (Figure 13), thus providing them with greater mechanical properties. The hierarchical ink they have used exhibits stiffness which is far greater than what is achievable with thermoplastics and photo-curable resins (Vat-polymerization). Maurath et al. [15] further proposed a new ink based on ceramic capillary suspensions for the FDM printing technology. They used

tapered nozzles with diameter as low as 200 μm and 610 μm for printing hexagonal honeycombs of dimensions $20 \times 34 \times 8$ mm and $60 \times 40 \times 8$ mm respectively, having 10-20 printed layers and about 8 and 50 cells (Figure 14). In general, they found that the 3D printed honeycomb was about 2-3 times stronger than the casted specimens.

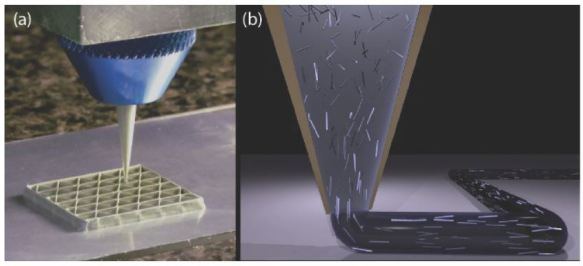

Figure 13: (a) 3D printing of a triangular honeycomb composite, (b) Alignment of high aspect ratio fillers within the nozzle during composite ink deposition [12].

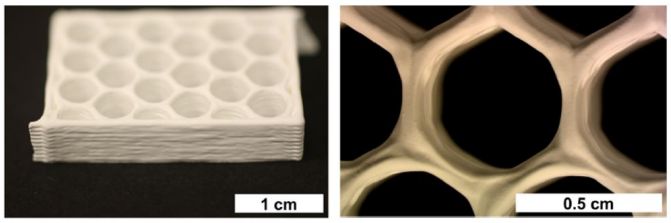

Figure 14: Hexagonal honeycomb structures, printed with a nozzle diameter of 200 μm [15].

But, the effect of FDM type of printing technology on the quality of lattice materials were investigated by Park et al. [13]. Due to the inevitable manufacturing defects like irregular strut diameter due to shrinkage, They have developed a two-step homogenization process which estimates the mechanical properties of the lattices taking into consideration the variations that might have been induced due to the additive manufacturing process. After its implementation, based on the experimentation's carried out, they observed a good accuracy with the estimated mechanical properties.

3 Analytical approach

The Cairo tessellation has a dual nodal connectivity of $Z = 4$ and $Z = 3$. Thus, the criteria for rigidity developed by Deshpande et al. [5] cannot be used directly as they were developed for *similar situated* lattices. But with the truss analysis and the matrix analysis, the Cairo lattice can be investigated for its rigidity by virtue of pure axial deformations. Ahead in the thesis, on comparing with the FE simulations, it can be verified whether the analysis methodology presented in this chapter describes the mechanics of the Cairo tessellation under periodic boundary conditions.

3.1 Relative density of the Cairo lattice

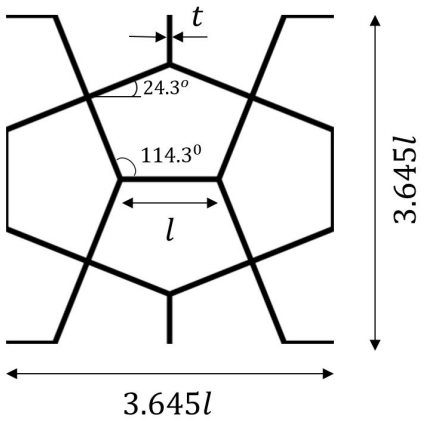

Figure 15: Unit cell for formulating the relative density of the Cairo lattice.

The volume of solid per unit cell is $20hlt$ where h is the out-of-plane thickness of the unit cell, l is the length of each member and t is their thickness. This volume is computed by considering each of the 20 members seen in Figure 15. The cross-sectional area is considered to be rectangular for simplicity. With the methodology used for creating the Cairo pentagon, all the members of the Cairo are of equal length l. The volume of the unit cell is $(3.645l)^2h$. Therefore, the relative density is given by,

$$\bar{\rho} = \frac{\rho^*}{\rho_s} = \frac{20}{13.29} \cdot \frac{t}{l} = 1.5046 \cdot \frac{t}{l} \tag{11}$$

The primary observation is that the relative density is not dependent on the out-of-plane thickness h of the lattice.

3.2 Structural analysis for forces

The forces in the members of the lattice is determined by a simple truss analysis where the members are subjected to only axial forces. The end joints of the members are taken as pin joints. In structural analysis, it is important to first determine the

determinacy of the structure. For simplification, the analysis considers a new unit cell (Figure 16), which is slightly shifted to a new position such that the boundaries of the unit cell comprises of cut-members.

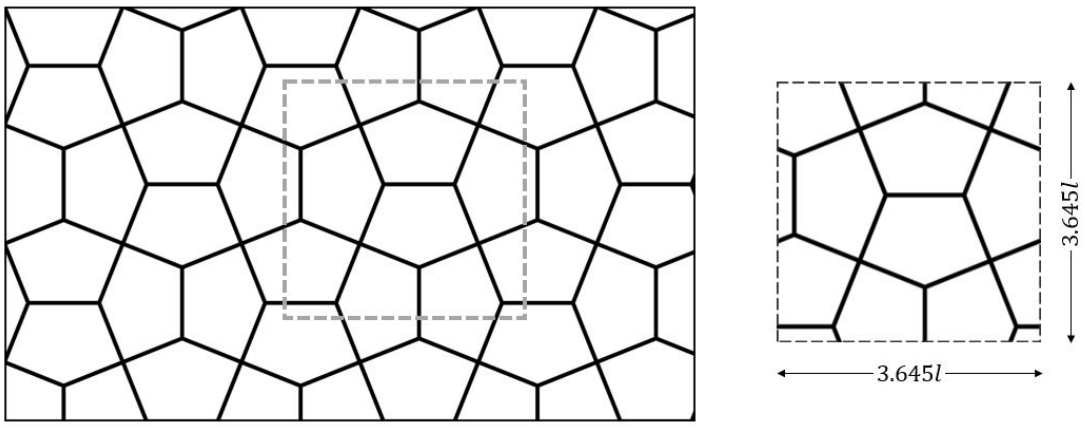

Figure 16: Unit cell for structural analysis.

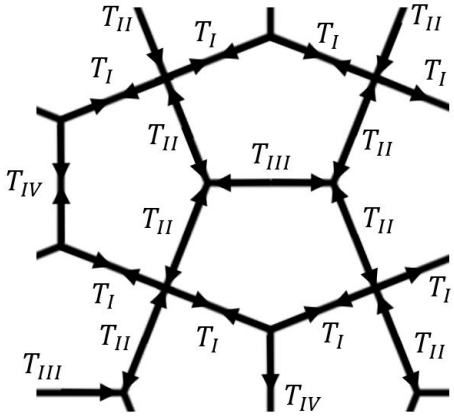

Figure 17: Forces in the members under a certain uni-axial compressive stress field.

The advantage of having a unit cell under periodicity, is the simplification of the forces. The forces in the inclined members making an angle 24.3° with the horizontal are equal in the infinite lattice (Figure 17). Similarly, for the member which makes an angle of 114.3° with the horizontal are in theory expected to carry the same forces. Let the former force be represented by a single force term, T_I and the latter be represented by T_{II}. Likewise, the forces in the horizontal members are equal, i.e. it can be represented by a single force term T_{III}. Also, the forces in the vertical members are equal and can be represented as T_{IV}.

The reaction forces, R_1, R_2, R_3 and R_4, due to periodicity is shown in Figure 18. The advantage of periodicity is taken in the reaction forces as instead of assigning a new reaction force to each of the cut-member ends, the members which are expected

to carry the same forces are given the same reaction force. With the loading in the members defined, the criteria $b + r = 2j$ is evaluated.

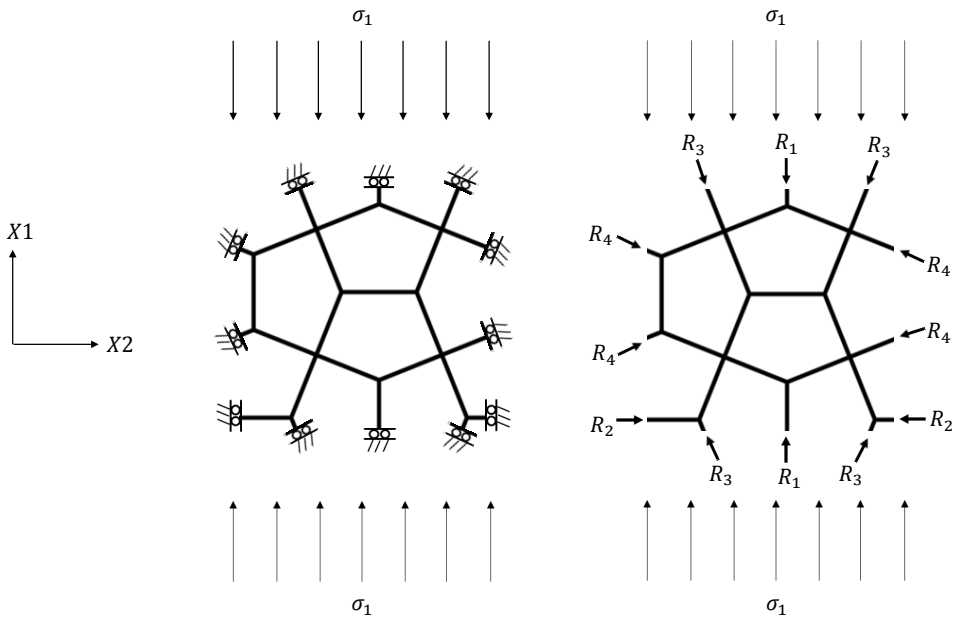

Figure 18: Reaction forces due to periodicity in a compressive stress field.

Number of members (b)	20
Number of reactions (r)	4
Number of joints (j)	12

$$b + r = 24 \tag{12}$$

$$2j = 24 \tag{13}$$

Therefore, we get $b + r = 2j$ i.e. the unit cell under *periodicity* is *statically determinate*. Method of joints is used under a uni-axial stress field in the X1 direction for formulating T_I, T_{II}, T_{III} and T_{IV} for each of the members in the unit cell as seen in Appendix A. The results are taken from Equations A15, A16, A17 and A18 as,

$\boldsymbol{T}$	**Type**
$T_I = 1.1342lh\sigma_1$	Tension
$T_{II} = -2.512lh\sigma_1$	Compression
$T_{III} = -2.0674lh\sigma_1$	Compression
$T_{IV} = 0.9335lh\sigma_1$	Tension

Table 2: Forces in the members of the Cairo tessellation under a uni-axial compressive stress field.

A uniaxial compressive stress field in the X2 direction would make the members acting in compression before, to act in tension and vice versa. The forces T_I and T_{II} will be interchanged and the same will occur with T_{III} and T_{IV}. This is due to the orthotropic nature of the Cairo lattice. The members carrying the T_{II} force are the highest stressed members.

3.3 Stiffness of the Cairo lattice

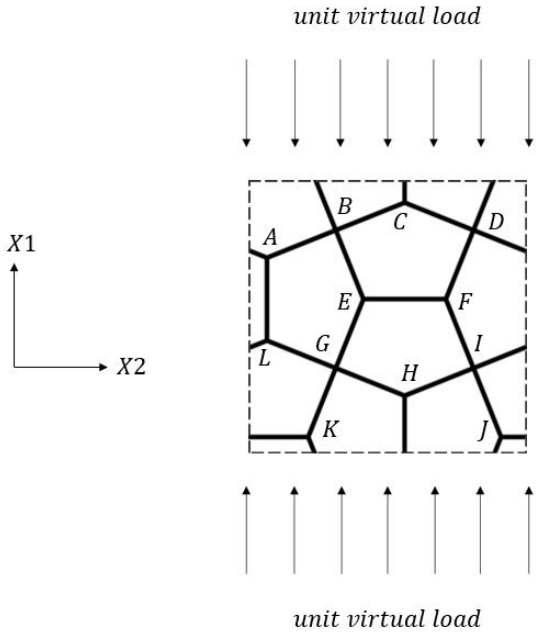

Figure 19: Unit virtual load applied to the unit cell in the X1 direction.

The virtual work is implemented for formulating the *normalized* stiffness of the Cairo lattice. The calculation for the virtual displacement due to the unit virtual load seen in Figure 19 can be found in Appendix C. From Equation B6 and Table C1, the displacement along the X1 direction due to a compressive virtual load in the X1 direction itself is,

$$u_1 = \sum_{i=1}^{m} \frac{(\delta P_v)_i P_i L_i}{E_i A_i} = 19.49445 \frac{h\sigma_1 l^2}{AE_s}$$

The strain along the X1 direction is,

$$\epsilon_1 = \frac{19.49445}{2l + 4lsin\theta} \frac{h\sigma_1 l^2}{AE_s} = 5.3467 \frac{l\sigma_1}{tE_s} \tag{14}$$

On rearranging we have,

$$\frac{E_1^*}{E_s} = 0.18703 \cdot \frac{t}{l}$$

In terms of the relative density, the stiffness *normalized* with the stiffness of the solid material for a Cairo lattice in the X1 direction and the X2 direction is,

$$\frac{E_1^*}{E_s} = \frac{E_2^*}{E_s} = 0.1243\bar{\rho} \tag{15}$$

Next, the virtual work is applied in the X2 direction of the Cairo unit cell for calculating its Poisson's ratio. The calculation can be found in Appendix D.

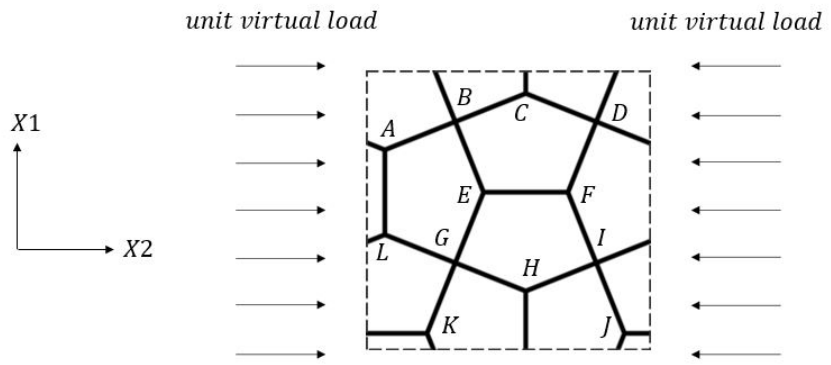

Figure 20: Unit virtual load applied to the unit cell in the X2 direction.

From Equation B6 and Table D1, the displacement along the X2 direction due to a compressive virtual load in the X2 direction itself is,

$$u_2 = \sum_{i=1}^{m} \frac{(\delta P_v)_i P_i L_i}{E_i A_i} = -14.623 \frac{h\sigma_1 l^2}{AE_s}$$

Therefore, the strain in X2 direction when the original compressive stress field is in the X1 direction can be formulated as,

$$\epsilon_2 = \frac{-14.623}{4lcos\theta} \frac{h\sigma_1 l^2}{AE_s} = -4.0111 \frac{l\sigma_1}{tE_s} \tag{16}$$

The Poisson's ratio for the lattice is given by,

$$\nu_{12}^* = \frac{-\epsilon_2}{\epsilon_1}$$

Therefore,

$$\nu_{12}^* = 0.75 \tag{17}$$

3.4 Compressive strength of the Cairo lattice

The compressive strength of the Cairo lattice is defined by the highest stressed member. From the force analysis we concluded that for a stress field along the X1 direction, the members linked to the single force term T_{II} has the maximum force. Thus, stress in those members the stress is given by,

$$\sigma_a = \frac{T_{II}}{A}$$

where, A is the cross-sectional area of the member. Therefore,

$$\sigma_a = \frac{-2.512lh\sigma_1}{ht}$$

These members would experience the yielding stress before the rest, hence it may be written $\sigma_a = \sigma_{ys}$ where σ_{ys} is the yield strength of the solid material. After rearranging,

$$\frac{\sigma_1^*}{\sigma_{ys}} = 0.3981 \cdot \frac{t}{l}$$

In terms of the relative density, the compressive strength *normalized* with the yield strength of the solid material for the Cairo lattice in the X1 direction and the X2 direction is,

$$\frac{\sigma_1^*}{\sigma_{ys}} = \frac{\sigma_2^*}{\sigma_{ys}} = 0.2646\bar{\rho} \tag{18}$$

But the Equation 18 is based on the fact that the members of the lattice undergo plastic yielding. At very low relative densities, the members are slender and elastic buckling precedes plastic yielding under uni-axial compression. The elastic buckling phenomenon is analytically governed by the Euler's critical load due to elastic buckling formulation,

$$T_{crit} = \frac{n^2\pi^2 E_s I}{l^2} \tag{19}$$

where n is a factor depending on the type of end-constraint applied to the beam and I is the area moment of inertia of the beam. It is seen that for *stretching* dominated lattices, $n \approx 2$ [1]. For simplifying the analysis, for the analytical calculation, the factor $n = 2$ is used, thus taking the joints as completely rigid.

Out of all the members in the Cairo lattice, the members carrying the T_{II} force is expected to undergo elastic buckling first when the Cairo lattice is compressed in the X1 direction. Therefore from Equations 11, 19 and A16,

$$\frac{\sigma_{el}^*}{E_s} = 0.3845\bar{\rho}^3 \tag{20}$$

Equation 20 is the analytical formulation for the elastic buckling deformation of Cairo lattices at low relative densities. An obvious question arises about the critical condition where the deformation mechanism changes from elastic buckling to plastic yielding. This is is answered by the *critical* relative density, where both the deformation modes are equally likely to occur.

The force in the critical members when subjected to an in-plane compressive stress field in the X1 direction is defined as $T_{II} = T_{crit} = ht\sigma_{ys}$ where σ_{ys} is the yield strength of the material used in the lattice. Using the yield strength in the *critical* relative density formulation, the least relative density which can undergo plastic yielding is presented. Thus, from Equation 19,

$$\left(\frac{t}{l}\right)_{crit} = \sqrt{\frac{3\sigma_{ys}}{\pi^2 E_s}}$$

Using the relative density formulation of the Cairo lattice, Equation 11, equation for critical density then becomes,

$$\bar{\rho}_{crit} = 0.8295\sqrt{\frac{\sigma_{ys}}{E_s}} \tag{21}$$

3.5 States of *self-stresses* and mechanisms

Earlier it was established that the unit cell under periodic boundary condition is *statically* determinate. But the formulation $b + r = 2j$ used does not entirely define the mechanics of a structure as it does not take into consideration the state of *self-stresses* and mechanisms in its equation. In other words, even though a structure might satisfy Maxwell's criteria for rigidity, the structure can be *statically* indeterminate or *kinematically* indeterminate or even both.

Pellegrino et al. [7] worked on it and provided us with a generalised Maxwell's equation described earlier in this thesis with the Equation 5. A matrix method has been proposed by them to calculate the number of states of *self-stresses*, s and mechanisms, m. Even though the matrix method has been designed for finite structures, from literature [8] it could be extended to infinite structures.

In order to simplify the analysis, a new unit cell has been considered (Figure 21). The figure also provides information about the node and member numbering used for the analysis.

Initially, Equation 6 is used, which needs the matrix $\mathbf{A}$, vector $\mathbf{t}$ and vector $\mathbf{f}$ to be contructed. The elements of the matrix $\mathbf{A}$ can be represented by,

$$\frac{x_i^n - x_i^m}{L_m} \tag{22}$$

Where $i = [1, 2]$ is the axis direction, $m = [1, 2...M]$ and n are joint numbers, and L_m is the length of each member. The Figure 22 is a typical example for calculating the elements of the matrix $\mathbf{A}$ at the n^{th} node to further aid towards understanding Equation 22.

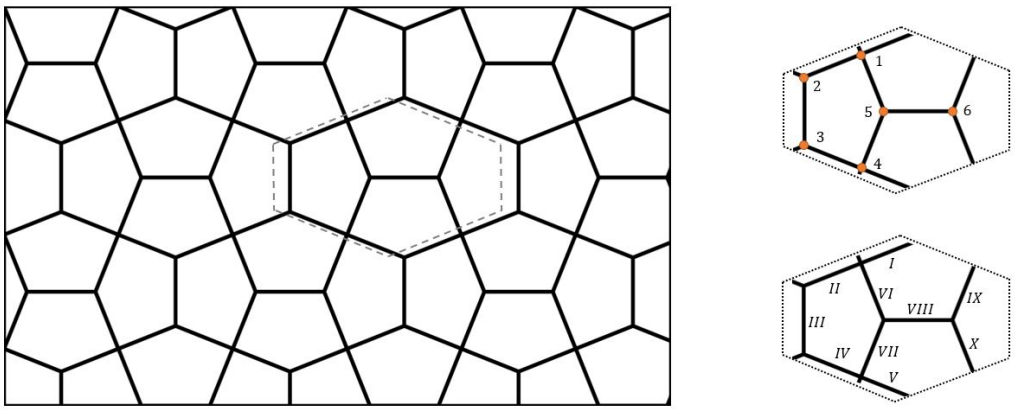

Figure 21: The unit cell used for matrix analysis. The convention used for node and member numbering can also be viewed.

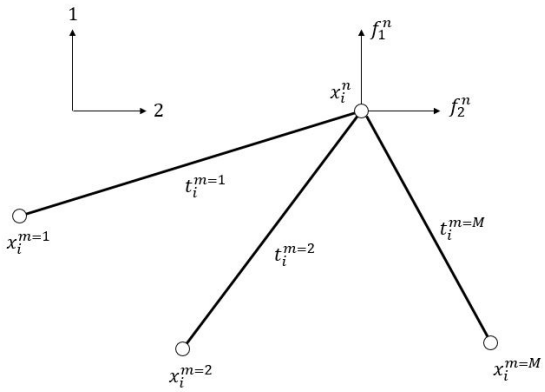

Figure 22: A joint equilibrium example at the n^{th} node based on the distances of nodes x_i^m from the node x_i^n. Also, t_i^m are the bar tensions and f_i^n are the forces at n^{th} node.

The *equilibrium* matrix **A** with the usage of Equation 22 can be written as,

$$\begin{bmatrix}
-0.91 & 0.91 & 0 & 0 & 0 & -0.41 & 0 & 0 & 0 & 0.41 \\
-0.41 & 0.41 & 0 & 0 & 0 & 0.91 & 0 & 0 & 0 & -0.91 \\
0 & -0.91 & 0 & 0 & 0.91 & 0 & 0 & 0 & 0 & 0 \\
0 & -0.41 & 1 & 0 & -0.41 & 0 & 0 & 0 & 0 & 0 \\
0.91 & 0 & 0 & -0.91 & 0 & 0 & 0 & 0 & 0 & 0 \\
0.41 & 0 & -1 & 0.41 & 0 & 0 & 0 & 0 & 0 & 0 \\
0 & 0 & 0 & 0.91 & -0.91 & 0 & -0.41 & 0 & 0.41 & 0 \\
0 & 0 & 0 & -0.41 & 0.41 & 0 & -0.91 & 0 & 0.91 & 0 \\
0 & 0 & 0 & 0 & 0 & 0.41 & 0.41 & -1 & 0 & 0 \\
0 & 0 & 0 & 0 & 0 & -0.91 & 0.91 & 0 & 0 & 0 \\
0 & 0 & 0 & 0 & 0 & 0 & 0 & 1 & -0.41 & -0.41 \\
0 & 0 & 0 & 0 & 0 & 0 & 0 & 0 & -0.91 & 0.91
\end{bmatrix}$$

The *tension* vector $\mathbf{t}$ and *load* vector $\mathbf{f}$ are given by,

$$\mathbf{t} = \begin{bmatrix} t_I \\ t_{II} \\ t_{III} \\ t_{IV} \\ t_V \\ t_{VI} \\ t_{VII} \\ t_{VIII} \\ t_{IX} \\ t_X \end{bmatrix}, \qquad \mathbf{f} = \begin{bmatrix} f_2^1 \\ f_1^1 \\ f_2^2 \\ f_1^2 \\ f_2^3 \\ f_1^3 \\ f_2^4 \\ f_1^4 \\ f_2^5 \\ f_1^5 \\ f_2^6 \\ f_1^6 \end{bmatrix}$$

The dimension of the *equilibrium* matrix $\mathbf{A}$ depends on the number of joints (joint space) and the number of bars (bar space). Here $\mathbf{A}$ has a dimension of 12×10. The dimension of the *tension* vector $\mathbf{t}$ is 10×1 and the dimension of the *load* vector $\mathbf{f}$ is 12×1. The *load* vector is represented as f_i^j where $i = [1, 2]$, signifying the axis direction X1 and X2, and $j = [1, 2, 3, 4, 5, 6]$ signifying the node numbers.

The *equilibrium* matrix $\mathbf{A}$ defines the static determinacy of a structure. The kinematic determinacy of a structure is defined by the compatibility matrix $\mathbf{B}$ or the *kinematic* matrix, for which we have an equation relating $\mathbf{B}$ with $\mathbf{e}$, a vector with bar *elongations* and $\mathbf{d}$, a vector with *displacements*. With Equation 8 it is known that the *kinematic* matrix $\mathbf{B}$ is a transpose of the *equilibrium* matrix $\mathbf{A}$. The dimension of $\mathbf{B}$ is 10×12.

The *elongation* vector, $\mathbf{e}$ and the *displacement vector*, $\mathbf{d}$ are given by,

$$\mathbf{e} = \begin{bmatrix} e_I \\ e_{II} \\ e_{III} \\ e_{IV} \\ e_V \\ e_{VI} \\ e_{VII} \\ e_{VIII} \\ e_{IX} \\ e_X \end{bmatrix}, \qquad \mathbf{d} = \begin{bmatrix} d_2^1 \\ d_1^1 \\ d_2^2 \\ d_1^2 \\ d_2^3 \\ d_1^3 \\ d_2^4 \\ d_1^4 \\ d_2^5 \\ d_1^5 \\ d_2^6 \\ d_1^6 \end{bmatrix}$$

Here, the dimension of $\mathbf{e}$ is 10×1 and the dimension of $\mathbf{d}$ is 12×1. The *displacement* vector is represented as d_i^j where $i = [1, 2]$, signifying the axis direction X1 and X2, and $j = [1, 2, 3, 4, 5, 6]$ signifying the node numbers.

At this point of time, it would be beneficial to revisit Equations 3 and 4, which relates the rank of matrix $\mathbf{A}$, r_A to the states of *self stresses*, s and the mechanisms, m. The rank r_A can be calculated by converting the matrix to an echelon form. The

detailed steps of the matrix analysis could be found in a well documented paper by Pellegrino et al. [7]. In this thesis, the results of the analysis have been presented.

Before finding the rank, r_A, the *equilibrium* matrix, **A** is augmented to an identity matrix of dimension 12×12. This particular set up is important to calculate the *left null space* of **A**.

Following the matrix operations, the rank of the *equilibrium* matrix, **A** is,

$$r_A = 8 \tag{23}$$

Therefore, from Equation 3 and Equation 4,

$$s = b - r_A = 2 \tag{24}$$

$$m = 2j - r_A = 4 \tag{25}$$

Thus, the infinite Cairo lattice has 2 states of *self-stresses* and 4 mechanisms, from which one can conclude that the lattice is *statically* and *kinematically* indeterminate. But for repetitive structures, it is not straightforward to determine the determinacy just by the number of s and m, unlike in finite trusses. In fact the similarities between the finite and infinite trusses with respect to the matrix analysis ends with the detemination of s and m. In the next paragraph, a pivotal paper has been referred which sheds more light on the determinacy of repetitive structures.

Guest et al. [8] have concluded that the matrix **A** will not be of full rank, which necessarily does not imply that the infinite truss is *statically* indeterminate. This is because, at any given time there are three types of loads at infinity, i.e tension or compression in the X1 direction, tension or compression in the X2 direction and the shear in the X1-X2 plane. Since a lattice structure is expected to carry these loads, they will appear in the number of states of *self-stresses*, s. Thus, for a repetitive structure to be *statically* determinate, the number of s should be 3, and each of them should represent the 3 types of average stresses described before. Similarly, the infinite lattice has rigid body motions in the X1 and X2 directions which feature in the number of mechanisms, m. Thus, for a lattice to be *kinematically* determinate, the number of m should be 2 and these should represent the 2 rigid body motions. A rigid body rotation is not allowed because of periodicity.

This further leads to a conclusion that no infinite truss can be *statically* and *kinematically* determinate at the same time. As an example, the Kagome lattice being *stretching* dominated, has 3 states of *self stresses* and 3 mechanisms. Though the lattice is *statically* determinate, it is not *kinematically* determinate as it has an extra internal mechanism. This extra mechanism is periodic in nature i.e. it does not cause macroscopic strains, making the Kagome *stretching* dominated [8].

On comparison with the results for the Cairo, it has 1 state of *self-stress* less and 2 mechanisms more than required for an infinite truss to be *statically* and *kinematically* determinate respectively. It is beneficial to plot the state of *self-stresses* and the mechanisms for further analysis. It should be noted that the matrix analysis directly cannot be used for determining the magnitude of s and m, rather the magnitude could be determined using a method put forward by Pellegrino [16]

shortly after the paper on matrix analysis, which uses *Singular Value Decomposition* of the *equilibrium* matrix **A**. This analysis has not been covered in this thesis, but can be taken as a recommendation for anyone who is interested to further study the Cairo lattice.

The *left null space* of **A** is,

$$\begin{bmatrix} 1 & 2.21 & 1.18 & 1.82 & 1 & 0 & 0 & 0 & 0 & 0 & 0 & 0 \\ 31.65 & 13.14 & 30.41 & 15.89 & 30.41 & 15.89 & 26.16 & 6.47 & 14.35 & 5.33 & 0 & 0 \\ 5.91 & 0 & 5.91 & 0 & 5.91 & 0 & 5.91 & 0 & 5.91 & 0 & 5.91 & 0 \\ 3.91 & 4.43 & 5.91 & 0 & 5.91 & 0 & 5.91 & 0 & 0 & 2.66 & 0 & 2.66 \end{bmatrix}$$

The *left null space* of **A** or the *null space* of **B** basically represents the mechanisms, m_i, where $i = [1, 2, 3, 4]$, signifies each of the mechanisms. A single mechanism is represented by a single row of the matrix.

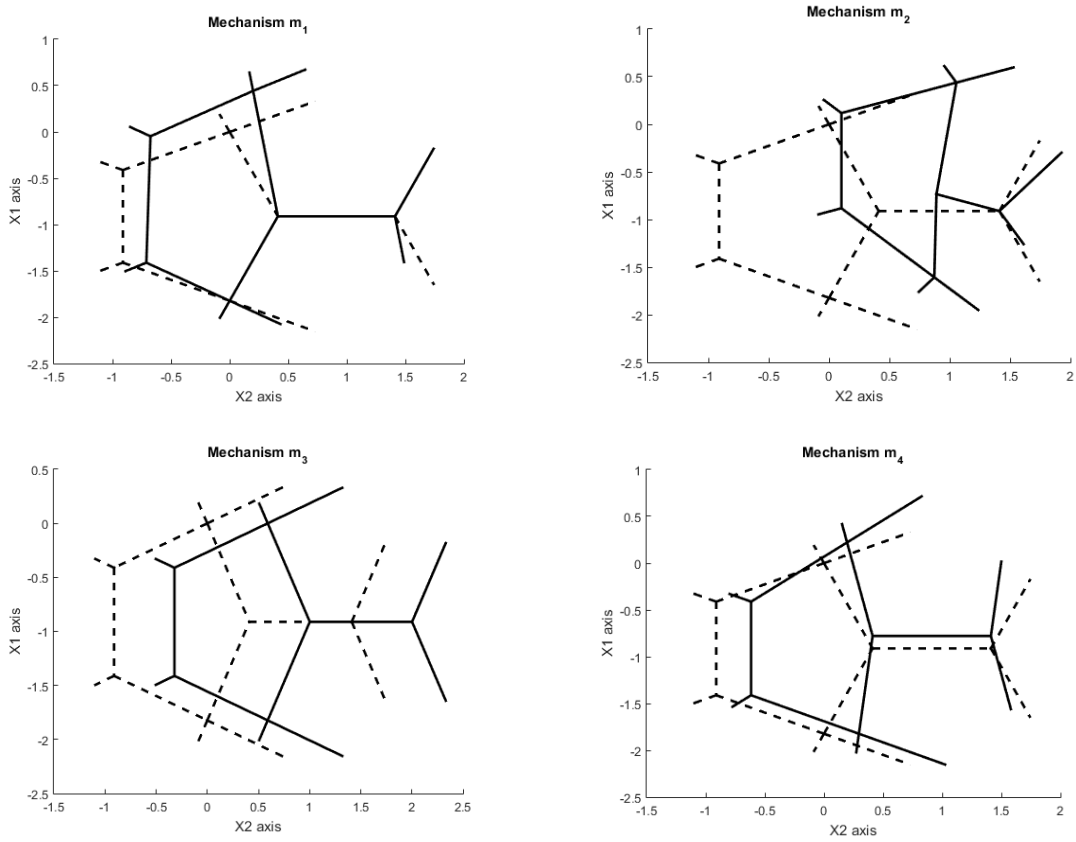

Figure 23: The 4 mechanisms in the Cairo lattice. The solid line indicates the deformation due to the mechanisms and the dashed line indicates the unit cell before deformation.

Figure 23 graphically shows the 4 mechanisms. It should be noted that mechanisms m_1, m_2, m_3 and m_4 have been scaled down by 5, 30, 10 and 20 times respectively. It is seen that m_1, m_2 and m_4 are internal mechanisms and m_3 is a

rigid body motion. The internal mechanisms make the Cairo lattice *kinematically* indeterminate.

A similar analysis can be conducted on the *kinematic* matrix **B** for identifying the states of *self-stresses*. The matrix **B** can be augmented to an identity matrix with dimension 10×10. On converting the matrix to an echelon form, we find that the rank remains unchanged. It is also proved from Equation 8 that both the matrices, **A** and **B** would have the same rank.

The simplified *left null space* of **B** or the *null space* of **A** is given by,

$$\begin{bmatrix} 1 & 1 & 0.82 & 1 & 1 & 0 & 0 & 0 & 0 & \\ 0 & 0 & 0 & 0 & 0 & 1 & 1 & 0.82 & 1 & 1 \end{bmatrix}$$

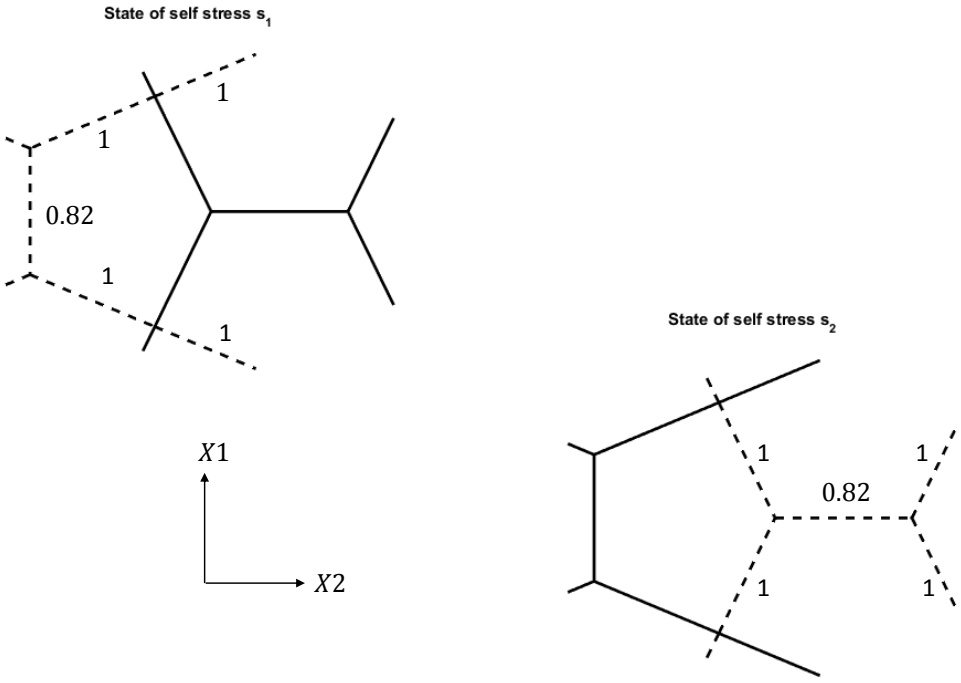

Figure 24: The 2 states of *self stress* in the Cairo lattice.

Figure 24 shows the 2 states of *self-stress*. The 2 states are represented by each of the 2 rows of the *left null space* of **B** matrix, and are noted as s_i, where $i = [1, 2]$. It is clear from the figure that the Cairo lattice has the ability to sustain the loads at infinity when they are aligned along the X1 direction or the X2 direction. But it cannot sustain shear forces. Thus, the Cairo lattice is not *statically* determinate, infact it is unstable under shear.

In summary, with the matrix analysis it has been proved that the infinite Cairo lattice is *statically* indeterminate and *kinematically* indeterminate. The method also suggests that the Cairo lattice is *stretching* dominated under pure uni-axial compressive loading but *bending* dominated under any other type of loading condition.

For being *stretching* dominated in the X1 and X2 directions, its internal mechanisms will not produce macroscopic strains i.e. the internal mechanisms of the Cairo has to be periodic in nature.

3.6 Summary

The relative density of the Cairo lattice is given by the Equation 11, which is a function of the thickness and the length of the members. The stiffness of the lattice is given by the Equation 15 when the lattice is loaded in uni-axial compression in either of the two (X1 or X2) orthogonal directions. The Poisson's ratio of the Cairo lattice is 0.75. The compressive strength of the lattice under the same uni-axial loading condition is defined by Equation 18. The *normalized* stiffness and the *normalized* strength is the same for the Cairo when either loaded in X1 or X2 direction due to orthotropy.

The *critical* criterion for the relative density has been defined. For *stretching* dominated lattices it has been observed that at very low relative densities they undergo elastic buckling and at high relative densities they undergo plastic yielding. The *critical* relative density which differentiates these two deformation modes is given by Equation 21. Subsequently, the formulation for elastic buckling deformation mode is given by Equation 20.

There are 2 states of *self-stresses* and 4 mechanisms in the infinite Cairo lattice, essentially making the lattice *statically* and *kinematically* indeterminate as it has 1 less states of *self-stress* representing shear and 3 internal mechanisms. The 2 states of *self-stresses* show the ability of the Cairo to sustain purely uni-axial loading in either X1 or X2 direction. But, the lattice is unstable against shear. Apart from the 3 internal mechanisms, the 4^{th} mechanism is a rigid body mechanism.

Even though, the Cairo lattice is *statically* and *kinematically* indeterminate, the state of *self-stresses* can have a stiffening effect on the mechanisms ([7],[31]) essentially justifying the unit exponent for the relative density in the *normalized* stiffness and the *normalized* strength equations. With the theoretical analysis, the infinite Cairo lattice is expected to be *stretching* dominated under pure uni-axial compressive force with the internal mechanisms being periodic in nature. But for any other loading condition, the infinite Cairo tessellation is expected to be *bending* dominated with the mechanisms producing macroscopic strains.

4 FE analysis of periodic Cairo unit cells

The mechanics for stiffness and strength developed for the infinite Cairo lattice in the previous chapter are verified by FE analysis of a unit cell with periodic boundary conditions in this chapter.

4.1 Geometry

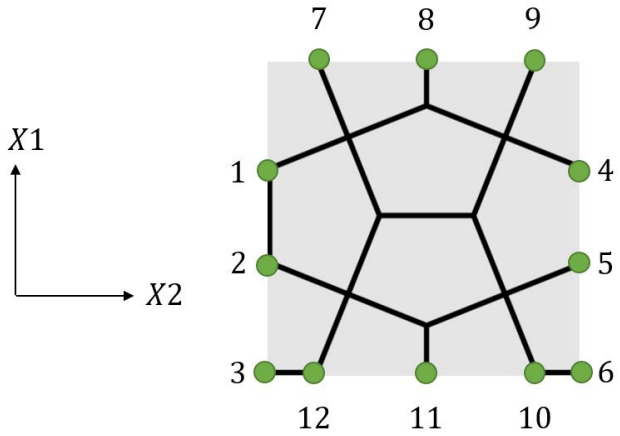

Figure 25: Geometry of the periodic unit cell with node numbering for the constraint equations.

A unit cell is the smallest representation of a tessellation, which when stacked against each other, forms the tessellation itself. The computational cost and time can significantly be reduced by the usage of a unit cell in FE simulations. Also, practically it is impossible to model an infinite lattice tessellation using an FE solver without the help of a unit cell subjected to periodic boundary conditions.

Abaqus CAE 6.14 has been used for conducting the FE simulations. For the model, the length of all the strut is 20 mm. Thus, the unit cell size computes to 72.9 mm $\times$ 72.9 mm. For simulating the various relative densities, the thickness of the members are varied but their lengths are kept constant.

4.2 Boundary conditions and nodal constraints

A displacement controlled boundary condition is applied to the unit cell. Here, the top edge is provided by a strain, the left and the bottom edges are provided with roller support such that the former is allowed to move only in the X1 direction and the latter is allowed to move only in the X2 direction (Figure 25). For the simulations, a strain of 0.05 is applied.

With periodicity, the effect of the surrounding infinite lattice is taken into consideration. In order to maintain periodicity, a set of constraints have been set up between the numbered nodes seen in Figure 26. There are primarily three types of constraints employed - a follower node follows the leader node in the X1 direction, a

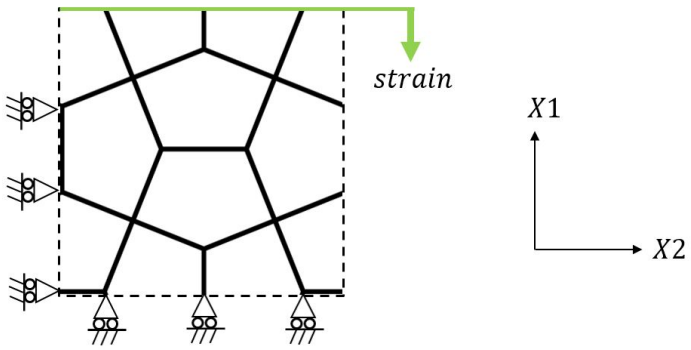

Figure 26: Boundary condition for the periodic unit cell under displacement control.

follower node follows the leader node in the X2 direction and the follower node has the same rotation as the leader node about the X3 direction (out-of-plane axis).

Let u_i^n be the displacement and ϕ_i^n be the rotations at the nodes, where $i = [1, 2, 3]$ represents the three orthogonal axis directions and $n = [1, 2, ...12]$ represents the node numbers at the cell walls. The constraint equations are,

$$u_1^1 - u_1^4 = 0 \; ; \quad \phi_3^2 - \phi_3^5 = 0 \; ;$$

$$u_1^2 - u_1^5 = 0 \; ; \quad \phi_3^{12} - \phi_3^7 = 0 \; ;$$

$$u_2^6 - u_2^5 = 0 \; ; \quad \phi_3^3 - \phi_3^6 = 0 \; ;$$

$$u_2^{12} - u_2^7 = 0 \; ; \quad \phi_3^{11} - \phi_3^8 = 0 \; ;$$

$$u_2^{11} - u_2^8 = 0 \; ; \quad \phi_3^1 - \phi_3^4 = 0 \; ;$$

$$u_2^{10} - u_2^9 = 0 \; ; \quad \phi_3^{10} - \phi_3^9 = 0 \; ;$$

$$u_2^5 - u_2^4 = 0$$

4.3 Non-linear FE simulations for strength

A fine mesh with 20 elements per member of the Cairo unit cell was utilized for the FE simulations. The resulting mesh includes 400 beam elements of type B21 for the entire model. The analysis is being carried out with the NLGEOM feature switched on. The NLGEOM takes into consideration geometrical non-linearity which might occur due to large deformations such as elastic buckling. Here, the load is applied in the form of steps based on the time increments requested. The material is considered to be Aluminium with Youngs modulus, $E = 70000$ MPa; Poisson's ratio, $\nu = 0.3$ and the yield strength, $\sigma_{ys} = 280$ MPa.

With the application of the displacement controlled boundary condition and the nodal constraints, the stress in the lattice is calculated by recording the peak reaction force on the upper edge of the unit wall in the X1 direction. If the reaction forces were to be calculated at the left and the right edges, the summation would turn out be zero, essentially proving that the stress field is purely uni-directional. This reaction force is divided by the cross-sectional area of the entire unit cell $(3.646 \times l) \times h$, here $l = 20$ mm and $h = 1$ mm.

As the relative density of the lattice keeps on increasing, the thickness of the members increases. This increase has an effect on the deformation mode of the lattice. At very low relative densities, it is expected that the lattice could sustain forces as long as the elastic buckling load is reached. After a certain *critical* relative density, the deformation mode changes to plastic yielding. With the analysis for strength, this section captures the elastic and plastic deformation modes, plots their stress-strain response and shows their stress contour.

A selected number of relative densities have been simulated within the range of 0.001 to 0.25. The strength of these lattices have been normalized with the yield strength and is unique to the Cairo lattice.

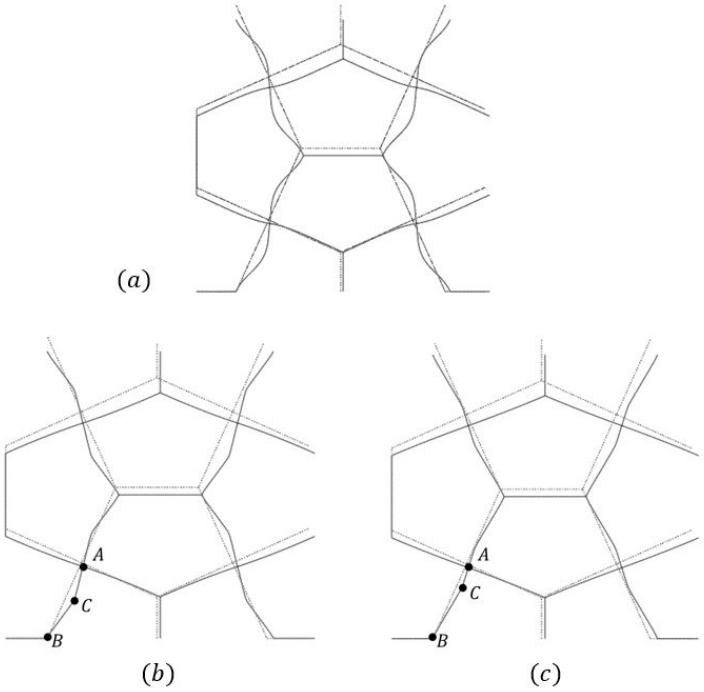

Figure 27: (a) Elastic buckling deformation mode for a relative density of 0.0105 at a strain of 0.05. (b) Formation of plastic hinges at locations A, B and C for a relative density 0.0316 at a strain of 0.05. (c) Plastic yielding deformation mode where the location of the plastic hinge C is moving closer to the joint with $Z = 4$ for a relative density of 0.1895 and at a strain of 0.05. (The dotted line represents the un-deformed unit cell and the solid line represents the deformed unit cell).

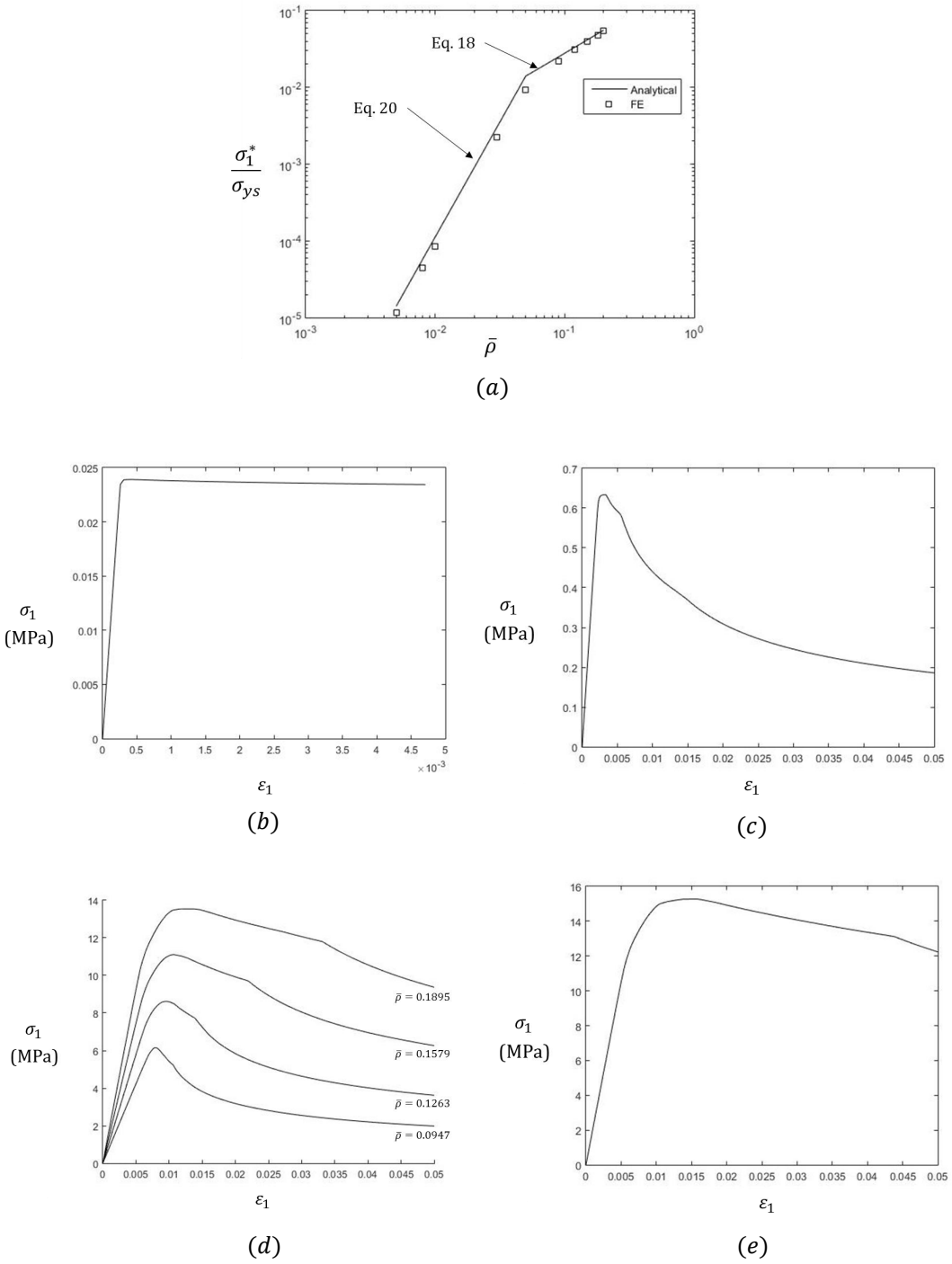

Figure 28: (a) Analytically *normalized* strength compared with FE results; The stress-strain response for relative densities of (b) 0.0105, (c) 0.0316, (d) 0.0947, 0.1263, 0.1579, 0.1895 and (e) 0.2106. The relative densities 0.0105 and 0.0316 undergo elastic buckling whereas the remaining undergo plastic yielding.

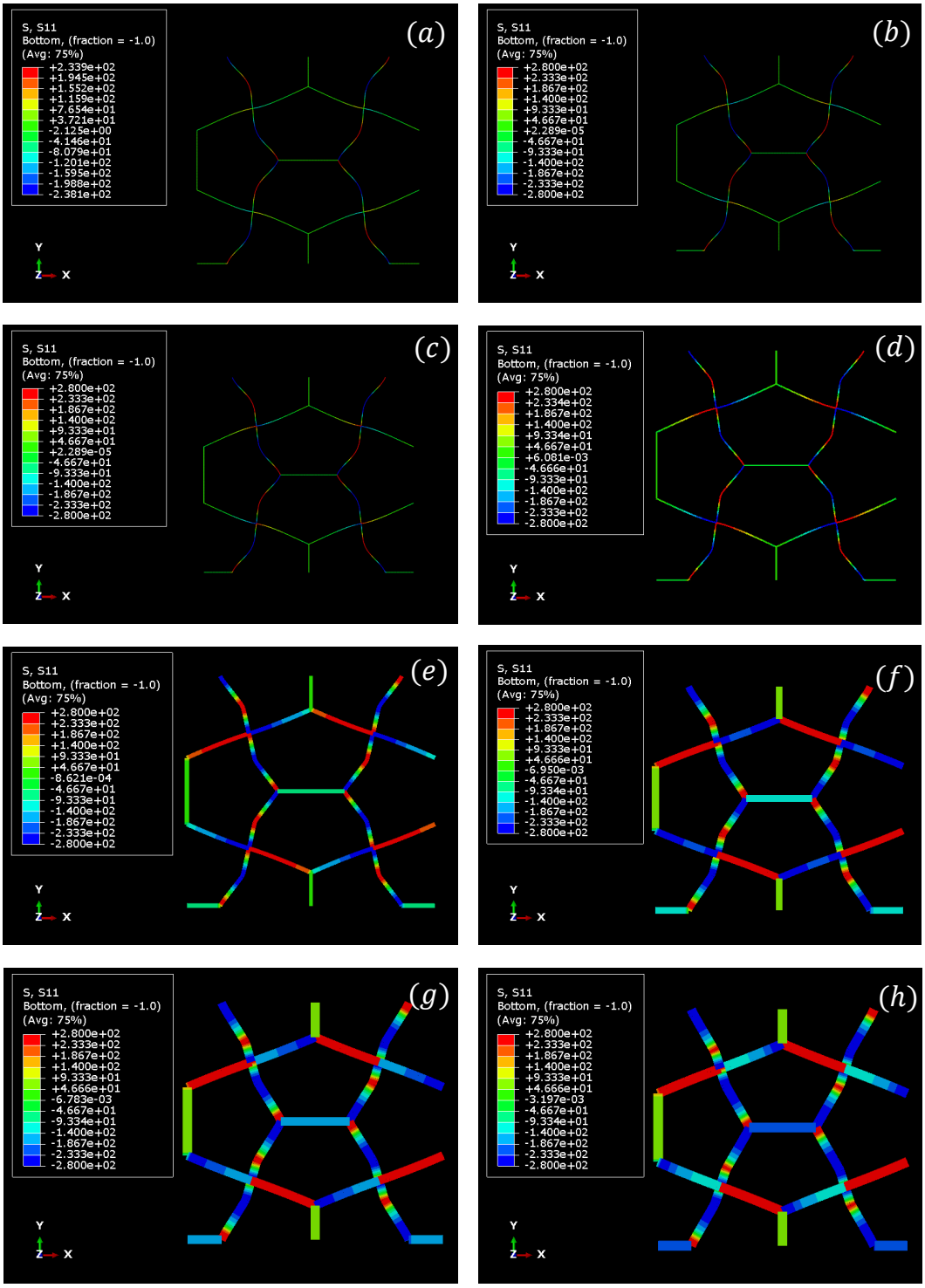

Figure 29: S11 stress contour (MPa) at a strain of 0.05 for relative densities (a) 0.0052 (b) 0.0084 (c) 0.0105 (d) 0.0316 (e) 0.0948 (f) 0.1579 (g) 0.1895 and (h) 0.2106. The relative densities 0.0052, 0.0084, 0.0105 and 0.0316 undergo elastic buckling whereas the remaining undergo plastic yielding.

The unit cell initially deforms elastically when the members carrying the T_{II} force has attained the elastic buckling load after a compressive stress field is applied in the X1 direction. This deformation mode is seen in Figure 27a and the corresponding stress-strain response in Figure 29b. For a relative density of 0.0105, the peak load that could be sustained by the unit cell was observed to be 1.74369 N, from the non-linear FE analysis. The Euler buckling equation 19 can be employed to calculate the elastic buckling load for a member carrying the T_{II} force as 1.5784 N. The difference in the elastic buckling load is due to the factor n taken as 2 in the Euler buckling formula. This difference can also be seen in the *normalized* strength plot in the Figure 28a for the elastic buckling line. When n is taken as 2, the end constraints of the member are considered to be fixed, which is a good approximation in *stretching* dominated lattices [1]. Even though, the deformation type of the Cairo has not yet been established, the factor $n = 2$ is accepted since, the analytical analysis are focused on the deformation mode being axial extension/contraction. It is observed that for very low relative densities, the Cairo lattice achieves a plateau state post the elastic buckling peak load. This makes the Cairo lattice with very low relative density an interesting candidate for energy absorbers [5]. With the increase in the relative density, the plateau region becomes less noticeable.

Using Equation 21, the *critical* relative density of the Cairo lattice based on the material properties used for Aluminium in this simulation is 0.0525. It has been observed that with the increase in the relative density and strain, plasticity is induced at the *nearly* rigid joints ($n \approx 2$) and the members with the T_{II} force. As we get closer to the *critical* relative density, softening of the stress strain response due to energy release as a result of plasticity is more visible (Figure 29c). Figure 29h provides an example of a typical Cairo lattice undergoing plastic yielding as the primary deformation mechanism after the *critical* relative density has been reached. The stress-strain response for the various relative densities and their corresponding S11 stress contour can be seen in Figures 28 and 29.

With the Cairo lattices, initially plastic hinges starts to appear almost mid way on the inclined struts comprised of the T_{II} force (Figure 27b) and later with the increase in the relative density, they make their way towards the node with connectivity of 4 (Figure 27c). In terms of solid mechanics, with the increase in the bending moment due to the high thickness (high relative density) of the lattice, the section of the Euler-Bernoulli beam undergoes substantial rotational deformation at the sites of plastic hinges as no more moments can be taken.

4.4 Non-linear FE simulations for stiffness

Just like the *normalized* strength, the *normalized* stiffness is a dimensionless parameter used for comparing the stiffness's of the various tessellations. The theoretical *normalized* stiffness seen in Equation 15, is compared with the FE results. The comparison is shown in Figure 30.

In the FE analysis, with the usage of *beam* elements, the effects of beam bending can be recorded as well. With the Figure 30, it can be seen that at higher relative densities, the FE plot starts to deviate from the analytical line. As the thickness of

the beam keeps on increasing, the contribution of bending of the beams towards the mechanics which were initially developed for pure axial deformations also increases.

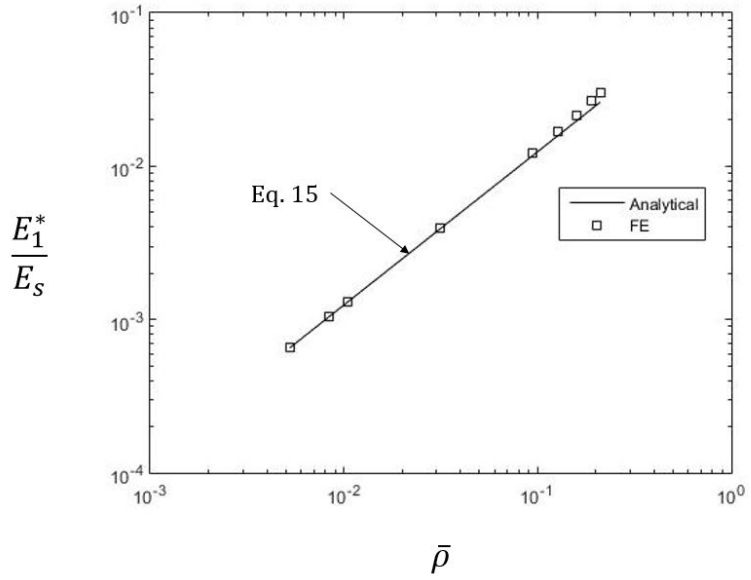

Figure 30: *Normalized* stiffness plotted against the relative density on a log-log scale based on FE and analytical analysis.

As an example, in Figure 31a, it is seen that for a relative density of 0.0105, the stress distribution in the inclined member carrying the T_{II} force is fairly uniform throughout its length. But at a higher relative density of 0.2106, a variation in the stress distribution can be seen. In the case of very low relative densities, the bending moments are small as the beam readily undergoes elastic buckling due to its slenderness. But at higher relative densities, when the primary deformation mode is plastic yielding, the resistance to bending increases, inducing very large bending moments. Due to these large moments we see a big gradient for the stress distribution at higher relative densities from smaller strains itself.

But even with the deviation, the exponent of the relative density is 1.0339 from FE, a number well below the required 2 for being classified as a *bending* dominated lattice. In other words, the beam bending does not make the Cairo lattice *bending* dominated. In conclusion, the mechanics were developed with the assumption that the Cairo will have axial deformation as its primary deformation mode. The FE results co-relate with the analytical line with good accuracy. Thus, with confidence it can be said that the Cairo lattice is *stretching* dominated when the average stresses are purely either along the X1 direction or the X2 direction. But, this result is not conclusive to state whether the Cairo lattice is *stretching* dominated in all possible average stress fields.

Next the Poisson's ratio is verified, where from FE it is seen for a relative density of 0.2106, the ratio is 0.748 which when compared to the theoretical ratio 0.75 proves to be of good accuracy. The displacements used for the computation of the Poisson's ratio are shown in Figure 32 and the analytical value is referred from Equation 17.

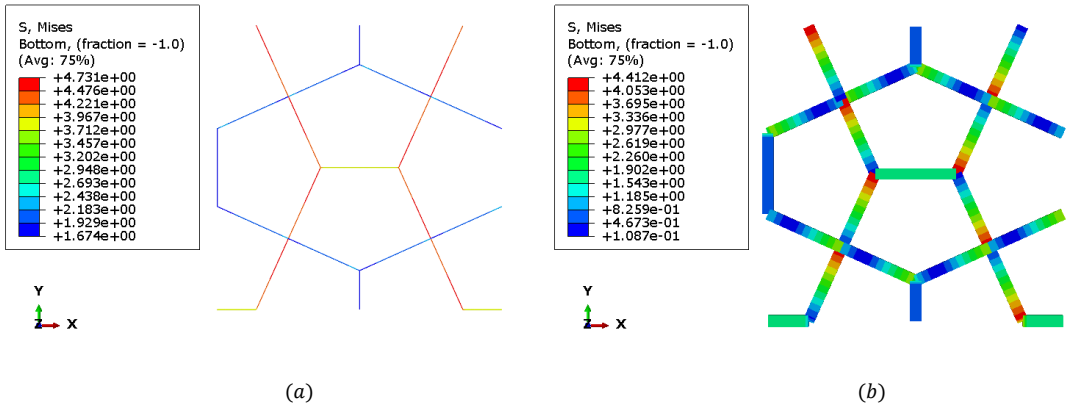

Figure 31: Von Mises stress (MPa) distribution in the inclined member carrying the T_{II} force in the linear elastic regime at a strain of 0.007% for a relative density (a) 0.0105 and (b) 0.2106.

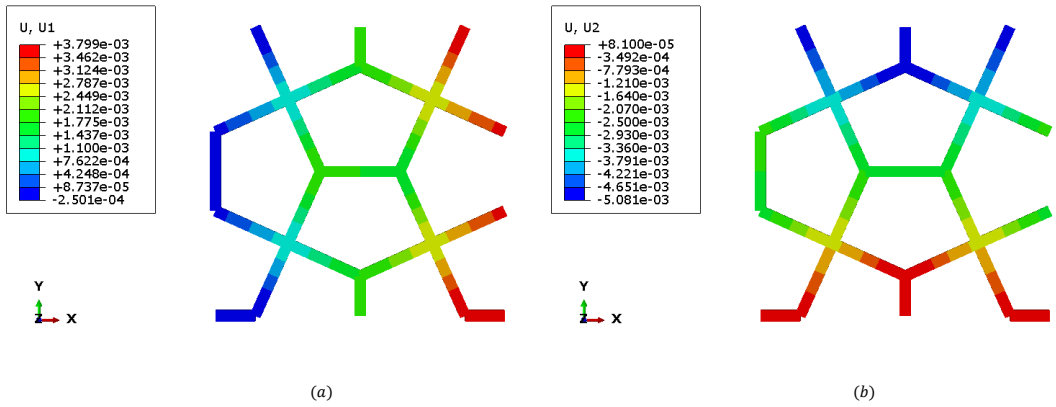

Figure 32: (a) Displacement along the X2 direction in millimeters when the relative density is 0.2106 at a 0.007% strain. (b) Displacement along the X1 direction in millimeters when the relative density is 0.2106 at a 0.007% strain.

4.5 Summary

On the application of periodic boundary conditions it is seen that the FE analysis is in good agreement with the analytical predictions. This further verifies our assumption of the Cairo lattice primarily being *stretching* dominated under a uni-axial stress field. The truss analysis can thus be applied for developing the mechanics of this tessellation. At higher relative densities (> 0.1) beam bending significantly effects the mechanics but it does not compromise the strength and the stiffness of the Cairo lattice. With the next chapter, the developed mechanics will be studied for their applicability in a finite Cairo lattice along with experiments.

5 Experimental approach

5.1 Compression of 2×3 Cairo lattice

The mechanics developed for the infinite Cairo lattice is studied for its validity by comparing them with the response of a finite Cairo lattice. For maintaining periodicity, it is imperative to have as many unit cells stacked together as possible. But due to the manufacturing limitations, the finite Cairo lattice selected has unit cells stacked together in a 2×3 configuration. The term 2×3 implies that the lattice has a maximum of 3 unit cells stacked horizontally (columns) and 2 unit cells stacked vertically (rows). The manufacturing limitations include, the size of the printing bed for the FDM based Ultimaker 3D printers and the size of the nozzle.

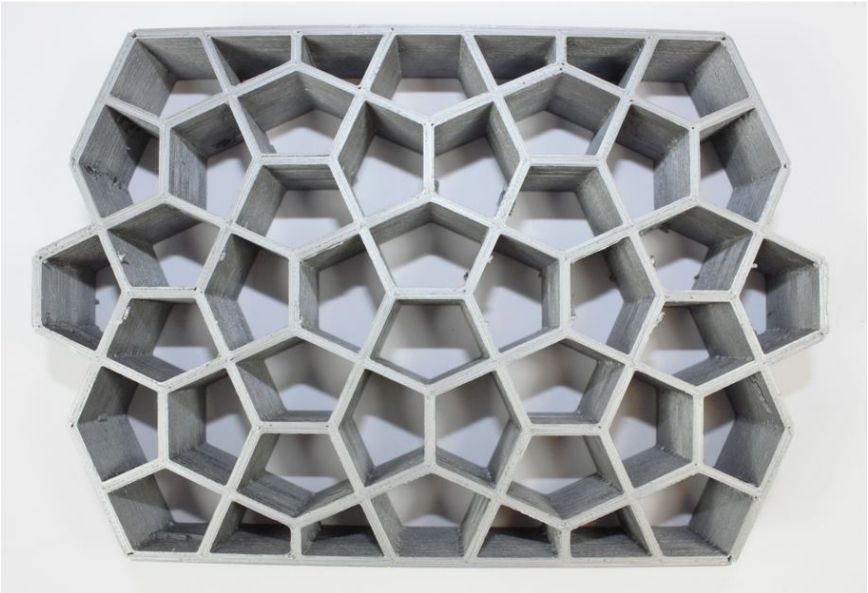

Figure 33: 2×3 Cairo lattice of relative density 0.22 made with PLA using an FDM based 3D printer.

The 2×3 Cairo lattice took about 39 hours to print with the printing bed temperature at 65°C and the nozzle temperature at 210°C. The infill density was set to 100%. The mass of the printing lattice is 132.354 g. The length of all the struts is 15 mm and their theoretical thickness is 1.9939 mm. The size of the specimen is 109.36 mm $\times$ 164.04 mm. An error of 1% to 2% was measured for the thickness of the struts. This error was mainly generated due to the surface irregularities affecting the vernier caliper reading. During the tests, the specimen is compressed at a strain rate of 0.0004 s^{-1}.

The non-linear FE set-up for the 2×3 Cairo lattice can be found in Appendix G. The material properties for the FE analysis is obtained from tensile testing of dog-bone specimens presented in Appendix E. The FE analysis of the 2×3 Cairo lattice shows a significant decrease in the strength when compared to the experimental response (Figure 34). Though the effect of the printing bed temperature on

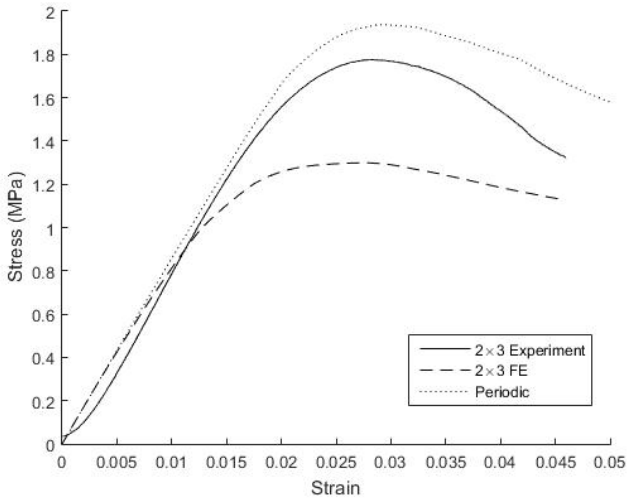

Figure 34: Comparison of the experimental and FE stress strain response of the 2×3 Cairo lattice with the periodic response of the Cairo unit cell for a relative density of 0.2

the mechanical properties of the PLA was studied seperately, evidence is found in literature that it might have an effect. Srithep et al. [41] studied the effect of time and temperature on PLA for its tensile strength and observed an increase of 17% and 26% when the PLA specimen were kept at a temperature of 80°C for 30 minutes and 60°C for 31 hours respectively.

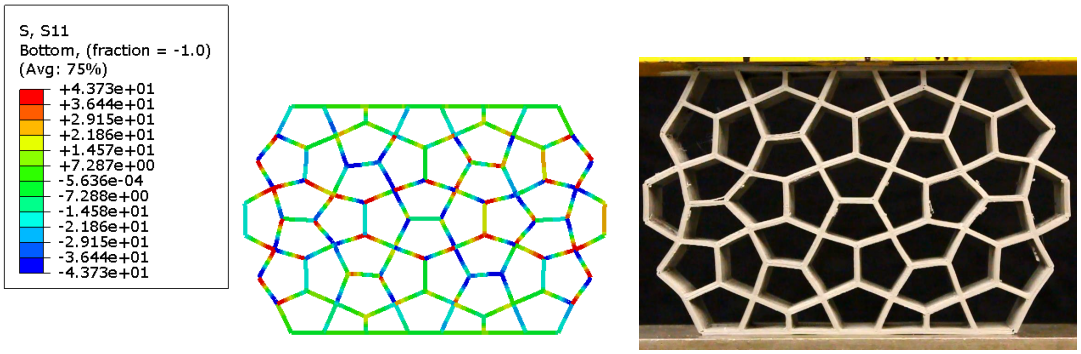

Figure 35: Strain producing mechanisms shown in the FE model and also captured during the experiments at a strain of 0.035 for a 2×3 Cairo lattice with a relative density of 0.2 (The unit of stress is MPa). The FE set-up for the model is in Appendix G.

But the more interesting observation is the difference between the periodic FE analysis and the 2×3 model FE analysis which are provided with the same material

properties in the Abaqus CAE 6.14 software. The deformation mode of the unit cells in the 2×3 lattice does not represent periodicity (Figure 35). As an example, the bottom two unit cells does not have a deformation mode that is expected for a Cairo lattice of relative density of 0.2106 under periodicity (Figure 29h). The deformation modes of the bottom two unit cells in the Figure 35 resembles more closely to the mechanism m_1 in Figure 23. The reduction in the strength of the 2×3 FE model when compared with the periodic model hints towards the mechanism to be acting as strain producing mechanisms i.e. they induce macroscopic strains in the members of the lattice.

Another example of the strain producing mechanisms in a finite Cairo model can be observed in the compression of a 9×10 finite Cairo lattice as well. The mechanisms m_1, m_3 and m_4 which were calculated by the matrix analysis in the Section 3.5 are mapped on the deformation diagram in Figure 36. These mechanisms in the infinite Cairo lattice are expected to be periodic, but are strain producing in the finite Cairo lattice even under uni-axial compression. As a result of these strain producing mechanisms, the deformation modes of elastic buckling and plastic yielding of the struts due to periodicity are not being observed. A finite 1×1 Cairo model will be studied in the next section for visualizing these deformation modes as they would take place in an infinite tessellation.

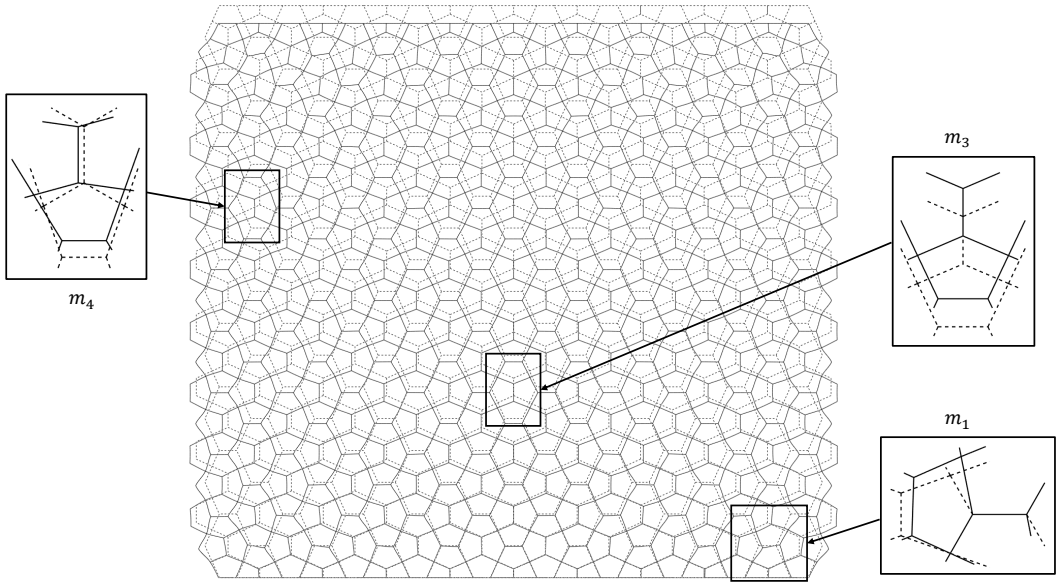

Figure 36: Mechanisms m_1, m_3 and m_4 mapped on a 9×10 finite Cairo lattice under uni-axial compression.

5.2 Compression of 1×1 Cairo lattice

In the previous section, it is seen that the deformation mode of plastic yielding in the struts carrying the T_{II} force for a 2×3 finite Cairo lattice with a relative density of 0.2 were not present due to the strain producing mechanisms. In order to visualize

the plastic yielding and the elastic buckling deformation mode which are expected in an infinite Cairo tessellation, a 1×1 Cairo model will be studied.

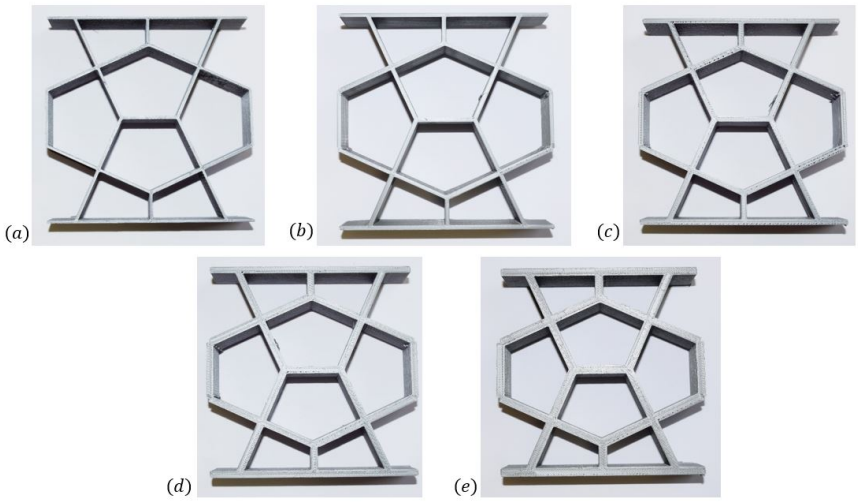

Figure 37: PLA specimens of 1×1 Cairo model with relative densities (a) 0.07 (b) 0.1 (c) 0.14 (d) 0.18 and (e) 0.22

The models used for the experimental analysis have been manufactured with the Ultimaker 3D printers with length of each strut as 25 mm (Figure 37). The size of the specimen is 91.12 mm $\times$ 91.12 mm and the out-of-plane thickness is 20 mm. The specimen with a relative densities 0.22 and 0.18 were printed together on the same printing bed which was set at a temperature of 75°C and the nozzle temperature at 220°C. The printing time was about 31 hours. The higher bed temperature was to improve the adhesion of the brim layer on the bed. The specimens with a relative density of 0.14 and 0.1 took about 16 hours to print with a bed temperature of 65°C. A lower bed temperature was opted as the adhesion of the brim layer layer was not a problem. Lastly, the specimen with a relative density of 0.07 was printed alone which took about 5 hours to be printed with the bed temperature of 65°C and the nozzle temperature of 210°C. The infill density is again 100%.

Their masses are 19.111 g, 28.609 g, 35.741 g, 48.483 g and 57.612 g for the relative densities in their increasing order. The post-processing of the printed specimens included removal of the brim layer and sanding the extra filaments which extruded due to the travel of the nozzle. The thicknesses of the struts measured with a vernier caliper shows an error in the range of 1% to 3% from the theoretical value. The specimens have been compressed at a strain rate of 0.0005 s^{-1}.

The non-linear FE set-up of 1×1 Cairo lattice can be found in Appendix H. Figure 38 compares the experimental results with the FE model of the 1×1 Cairo lattice and the FE results of a unit cell subjected to periodic boundary conditions. The very first observation is the increase in stiffness for the 1×1 Cairo model from the periodic model due to the extended upper and lower horizontal bars. It is also observed that the slope of the linear elastic region for the 1×1 experimental Cairo specimens are almost similar to the FE analysis of the same model. The experimental

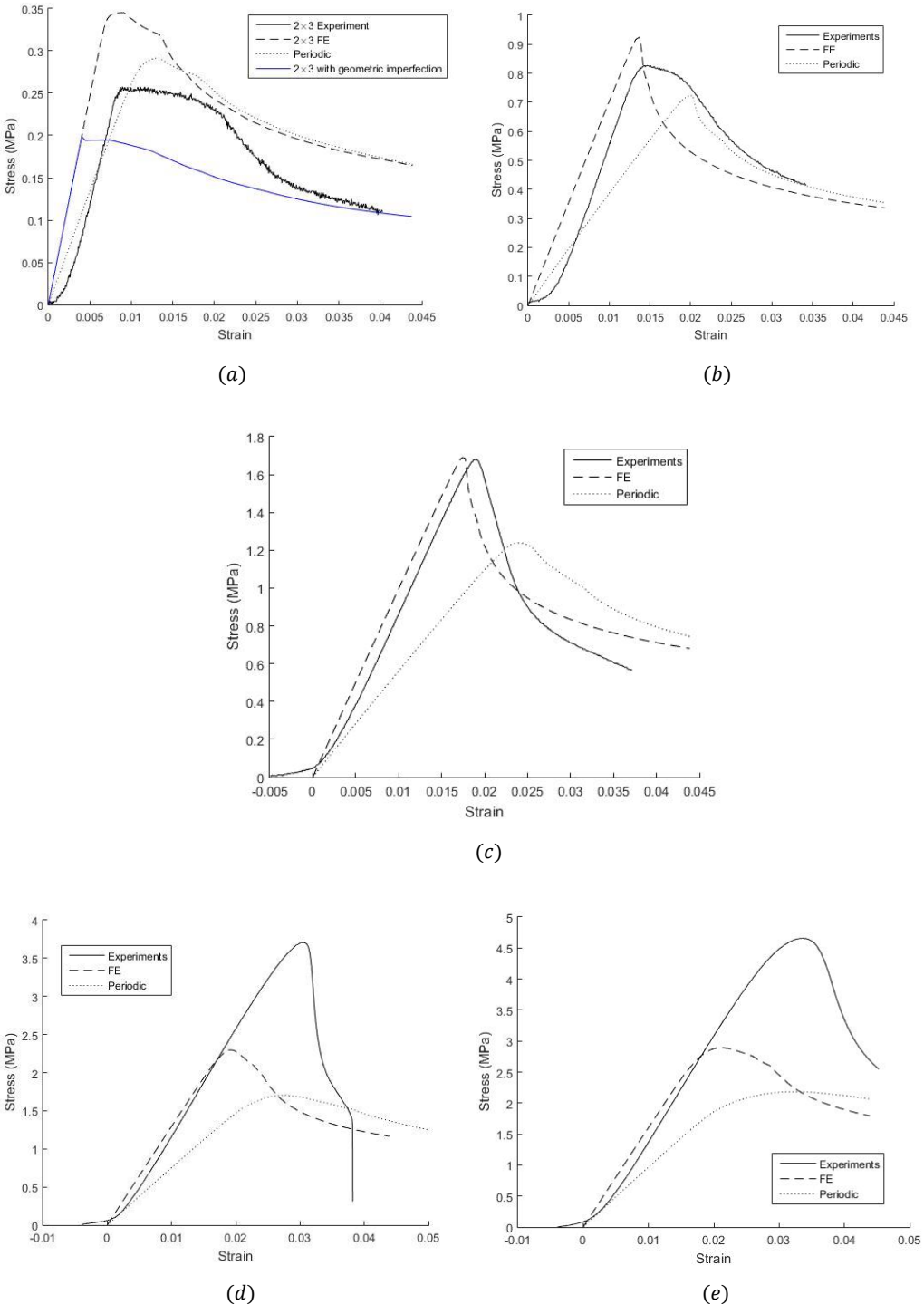

Figure 38: Comparative stress-strain plots for the 1×1 Cairo model with relative densities (a) 0.07, (b) 0.1, (c) 0.14, (d) 0.18 and (e) 0.22. A geometric imperfection of scale factor 0.005 based on the elastic buckling analysis has been shown for a relative density of 0.07.

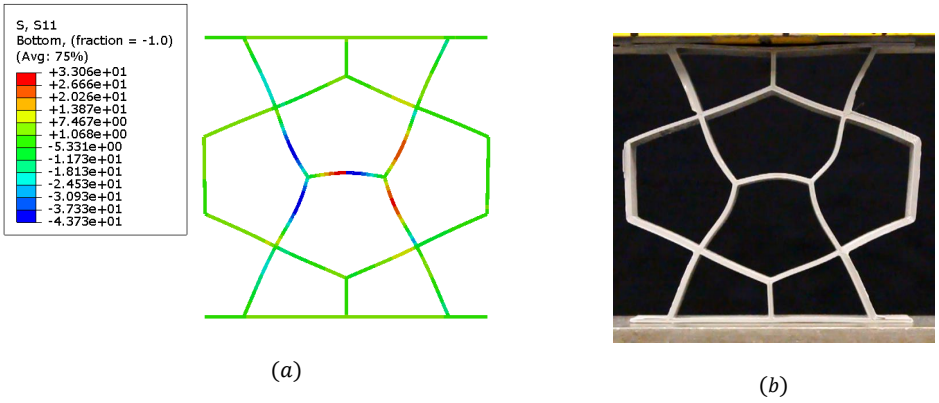

(a)

(b)

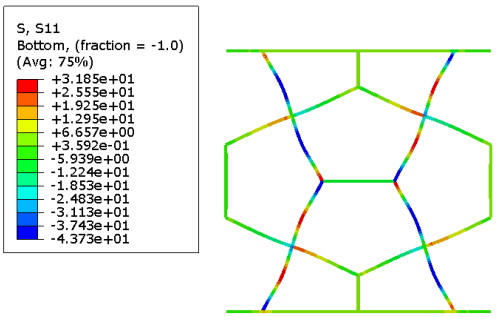

(c)

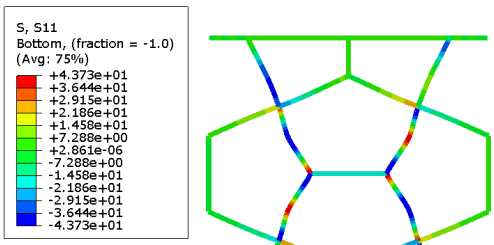

(d)

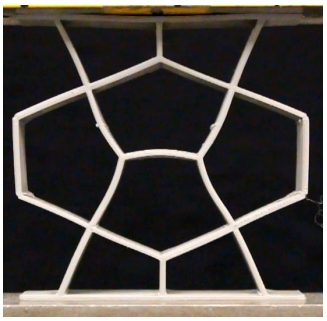

(e)

Figure 39: (a) FE with imperfections for relative density 0.07 at strain 0.004 (b) Experimental deformation for relative density 0.07 at strain 0.01 (c) FE for relative density 0.07 at strain 0.01 (d) FE for relative density 0.1 at strain 0.014 (e) Experimental deformation for relative density 0.1 at strain 0.018 (The unit for the stress is MPa). The FE set-up of the 1×1 model is in Appendix H.

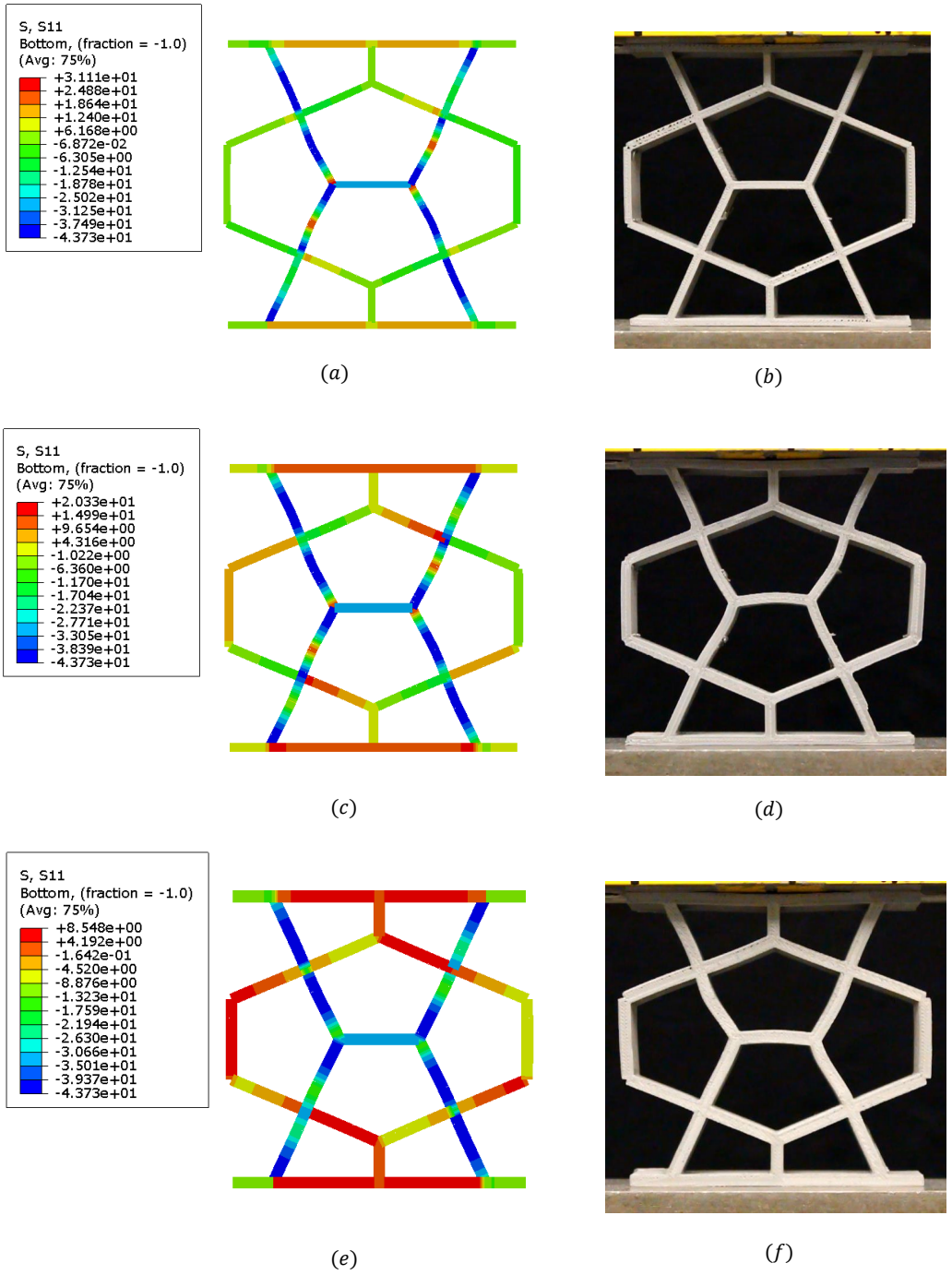

Figure 40: (a) FE for relative density 0.14 at strain 0.018 (b) Experimental deformation for relative density 0.14 at strain 0.02 (c) FE for relative density 0.18 at strain 0.02 (b) Experimental deformation for relative density 0.18 at strain 0.032 (d) FE for relative density 0.22 at strain 0.025 (e) Experimental deformation for relative density 0.22 at strain 0.037 (The unit for the stress is MPa). The FE set-up of the 1×1 model is in Appendix H.

strength for the specimens with a relative density of 0.07 and 0.1 is less than the FE strength, primarily because of the imperfections due to the shrinkage of the PLA during manufacturing and the void spaces in between the layers.

For taking manufacturing irregularities into consideration, inclusion of geometric imperfections in the FE model of the 1×1 Cairo lattice softens the stress-strain response below the experimental curve by almost 25% for the lattice with a relative density of 0.07 even when the lowest scale factor of 0.005 where the imperfection actually has an effect is used (Figure 38a). Hence, the usage of geometric imperfections based on the elastic buckling analysis were not incorporated in the analysis ahead. But the deformation mode due to the imperfections is very similar with the central horizontal bar elastically buckling (Figures 39a and 39b).

The FE and the experimental results of the 1×1 Cairo model for a relative density of 0.14 is in good agreement (Figure 38c). Again it is observed that the 1×1 model is stiffer and stronger than the periodic model. The FE contour and the experimental deformation closely correlate with each other (Figures 40a and 40b). For higher relative densities of 0.18 and 0.22, the experimental strength is higher than the FE strength of the 1×1 Cairo model even though the slope of the linear elastic region i.e. stiffness is almost the same (Figures 38d and 38e).

The 5 dogbone specimens took about 12 hours to be printed. Thus, the higher relative densities of 0.18 and 0.22 spends considerably more amount of time than the dogbone specimen on the heated bed of the Ultimaker 3D printer. As a matter of fact, the bed temperature was 60°C for the dogbone specimens but was 75°C for the 1×1 Cairo model of relative densities 0.18 and 0.22, which is infact higher than the glass transition temperature of PLA. This indirectly can be leading to the increase in the strength of the PLA for the higher relative densities by about 38% and 34% for relative densities 0.18 and 0.22 respectively [41]. The effect of FDM printing technology on the mechanical properties of polymer based lattices is a recommendation for future work.

In Figure 38d, the drop in the stress for the post plastic buckling response is due to the breaking of an inclined strut as a result of manufacturing imperfections. The FE contour and the experimental deformation mode just after the peak load for the 1×1 Cairo model is shown in Figures 39 and 40. The elastic buckling and plastic buckling of the inclined struts eventually lead to the formation of plastic hinges. The location of these hinges are presented in Figure 41. It is observed that the imperfections in the specimens influence the location of the hinge. In a periodic infinite lattice, a plastic hinge would not be observed in the central horizontal members as they tend to always remain straight when the stress field is purely uniaxial.

The *normalized* stiffness the *normalized* strength of the 1×1 Cairo lattice is compared with the analytically formulated *normalized* stiffness and *normalized* strength in Chapter 3 for PLA. The FE simulation for a unit cell with PLA material properties can be found in Appenix F. At higher relative densities, the strength of the 1×1 Cairo lattice is higher than theory (Figure 42). This can be attributed to the increase in strength due to prolonged heat applied to the specimen during manufacturing. At lower relative densities, the strength is below the theory and the existence of manufacturing imperfections can be considered as a candidate for the

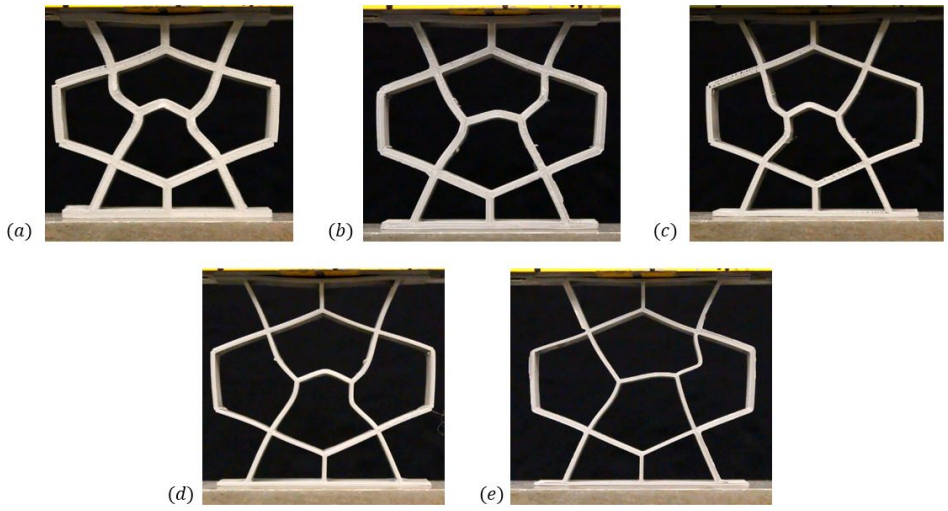

Figure 41: Formation of plastic hinges for relatives of (a) 0.22 (b) 0.18 (c) 0.14 (d) 0.1 (e) 0.07.

behaviour, but more investigations are required on the effects of imperfections.

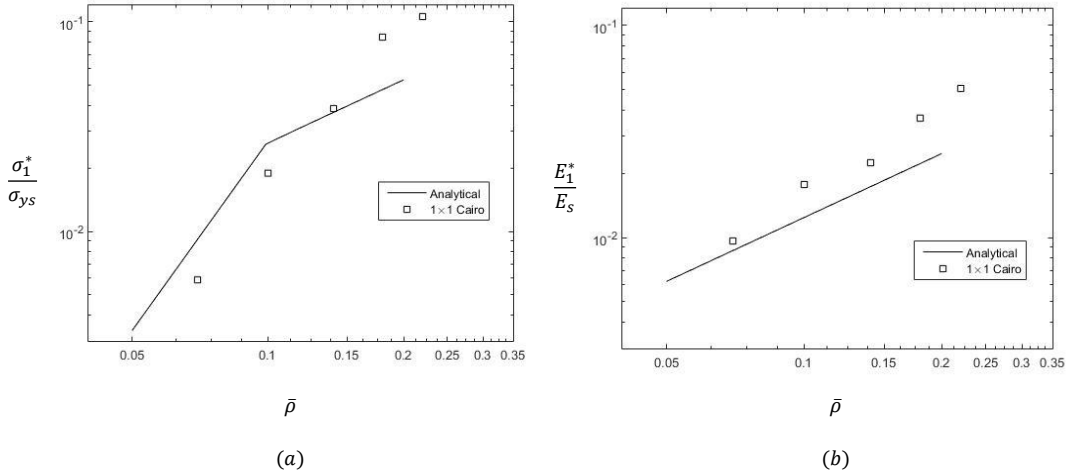

Figure 42: (a) Comparison of the *normalized* strength plot of the 1×1 Cairo specimen with the analytical expressions. (b) Comparison of the *normalized* stiffness plot of the 1×1 Cairo specimen with the analytical expression.

5.3 Compression of 2×3 Cairo lattice with patching

With this section, an attempt is made by intuitively placing patching bars to regain the strength of the 2×3 Cairo model and consecutively observe the plastic yielding deformation mode for a relative density of 0.2.

The Kagome lattice is *statically* determinate but *kinematically* indeterminate. For a finite Kagome lattice, this was solved by Hutchinson et al. [28] by adding

patch bars. They used Maxwell's generalized equation for determining the number of patch bars to be used in a finite Kagome lattice in order to make it *statically* and *kinematically* determinate at the same time where it needed 9 patch bars for the configuration seen in Figure 43.

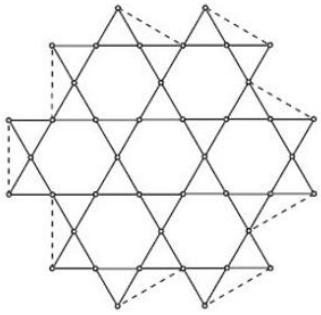

Figure 43: Patching scheme (Dotted lines) for a finite Kagome lattice. [28].

The 2×3 Cairo model used in this thesis has 127 members and 82 joints i.e. $b = 127$ and $j = 82$. Based on the generalized Maxwell's rule, Equation 5, for $k = 3$ (considering 3 kinematic constraints in the finite model), $s - m = -34$. As the infinite Cairo lattice has 2 states of *self-stresses*, there would be a need of 36 patch bars to make the finite Cairo lattice *statically* and *kinematically* determinate. Such a huge number of patch bars would change the entire topology of the Cairo lattice. An intuitive method was rather opted to implement patching of the 2×3 Cairo lattice based on the motion of the joints in Figure 35. The primary aim was to implement less number of patching bars as possible to avoid the motion of the joints, simultaneously regaining the strength of the lattice.

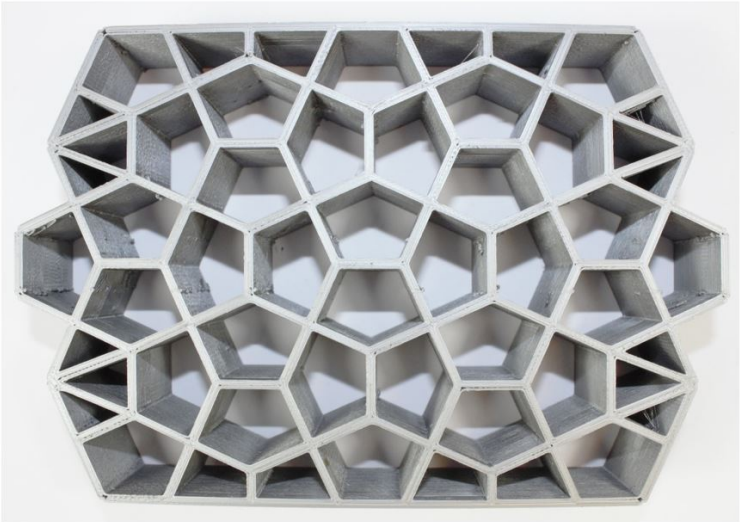

Figure 44: 2×3 Cairo model with patching bars in the pentagons at the left and the right edges.

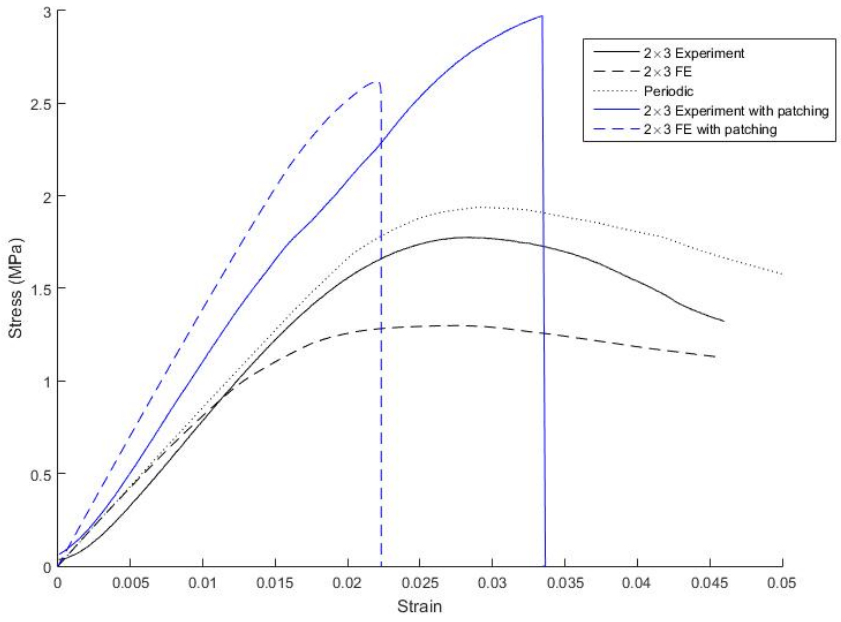

Figure 45: Comparison of the 2×3 Cairo experimental and FE lattice with patching, without patching and periodicity for a relative density of 0.2.

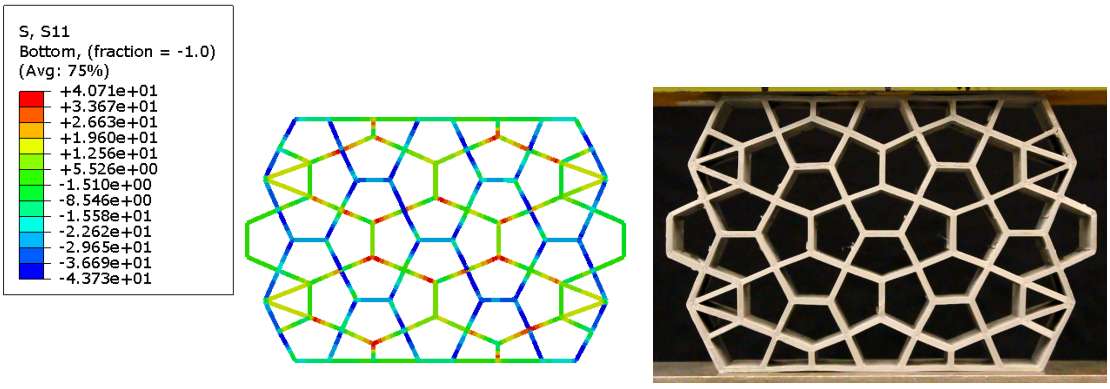

(a) (b)

Figure 46: FE model and experimental deformation of the 2×3 finite Cairo lattice with patch bars at strain 0.022 and 0.033 respectively (The unit of stress is MPa). The FE set-up for the 2×3 model with patching is in Appendix I.

The 2×3 Cairo lattice with patch bars has the same relative density of 0.2 as the model without patch bars (Figure 44). The strut length is kept 15 mm and the size of the entire lattice is again 109.36 mm $\times$ 164.04 mm. The 2×3 Cairo lattice with patch bars took 43 hours to print with the printing bed temperature at 65^oC and the nozzle temperature at 210^oC. The specimen was set at 100% infill density. The

mass of the specimen is 143.625 g. These specimens undergo similar compression like the 2×3 model without patching. The specimen is shown in Figure 44.

The non-linear FE setup for the 2×3 Cairo lattice with patching can be found in Appendix I. After patching, the strength and the stiffness of the 2×3 experimental model increases when compared with the experimental specimen without patching (Figure 45). In fact patching makes it stronger that periodicity itself. The patching scheme inhibits the mechanisms in terms of the joint displacements which otherwise were producing macroscopic strains and softening the response (Figures 35 and 46).

The post peak load collapse for the 2×3 Cairo lattice with patching is due to the breakage during the experiments (Figure 47). It is seen with the Ultimaker printers that the corners of the specimen have high porosity - mainly because of material shrinkage on cooling and the travel route of the nozzle head. If the breakage is closely observed, it originates from the top left corner and travels at 45° downwards. Due to the lack of sufficient material at these corners, the lattice ruptures at these places, The inclined fracture path symbolizes the presence of shear which aggravated the damage. An example of the gap at the corners is shown in Figure 47 for the top right corner. The energy released from the breakage of the corner was seen to be enough to fracture the entire shearing plane. The patching bars try to bring the finite 2×3 Cairo lattice back to periodicity, but it would be wise if after adding the patch bars, a structural analysis using the matrix method is conducted to see if the states of *self-stress* and the mechanisms have been altered, and if it is - is it for the better.

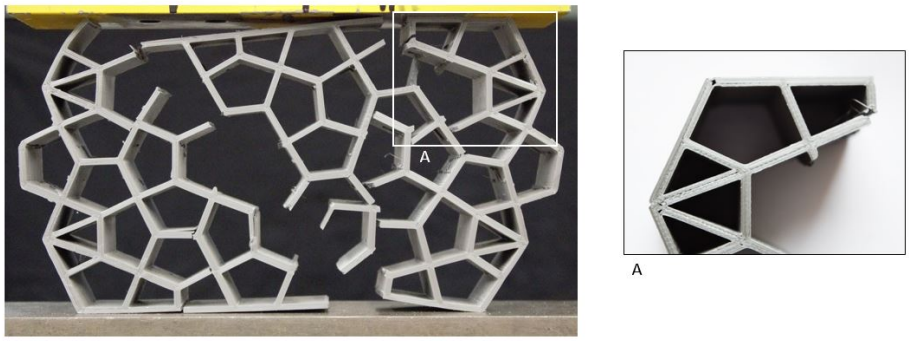

Figure 47: Breakage of the 2×3 Cairo finite lattice during compression testing at a strain of 0.033. The box 'A' shows one of the gaps at the corners of the specimen where the breakage started.

The stiffening of the 2×3 Cairo lattice with the addition of 8 patching bars rather than the recommended 36 based on the Maxwell's generalized equation for rigidity can possibly be attributed to the concept of *tensegrity*. Buckminster Fuller [38] introduced the concept of *tensegrity* (Tension-integrity) in structures where a set of rigid bodies in compression are stable due to strings in tension, thus making it a *pre-stressed* structure. Their uniqueness lies in the fact that, even though the structure is made of strings and rigid bars, their induced tensions and compressions does not make it a mechanism due to their state of stress. Calladine [39] further

proposed that in trusses, the strings can be replaced by rigid rigid bars similar to the ones in compression and put-forth the idea that the states of *self-stress* induced in the truss have the ability to make a structure *stiff* and eliminate mechanisms, similar to *tensegrity* structures, even if Maxwell's rule states otherwise. Calladine even stated that Maxwell was very well aware of the existence of such structures but classified them as structures with lower order stiffness. Elsayed [31] in his PhD, presented the idea of *tensegrity* in lattice materials where he mentions that the states of *self-stress* in a lattice can render it stiff. The role of patching in a finite Cairo lattice which has states of *self-stresses* needs to be studied further for its stiffening effect on the mechanisms and the applicability of the *tensegrity* concept.

5.4 Manufacturing defects with Fused Deposition Modeling

The FDM type of printers are largely used for prototyping - especially machines like the Ultimaker which are low cost as compared to the other industrial 3D printers. With this thesis, one of the interests was to determine if such prototyping 3D printers can today be used for making lattices especially for structural applications. Cheaper manufacturing costs would eventually lead to wider acceptance of the lattices in the industry.

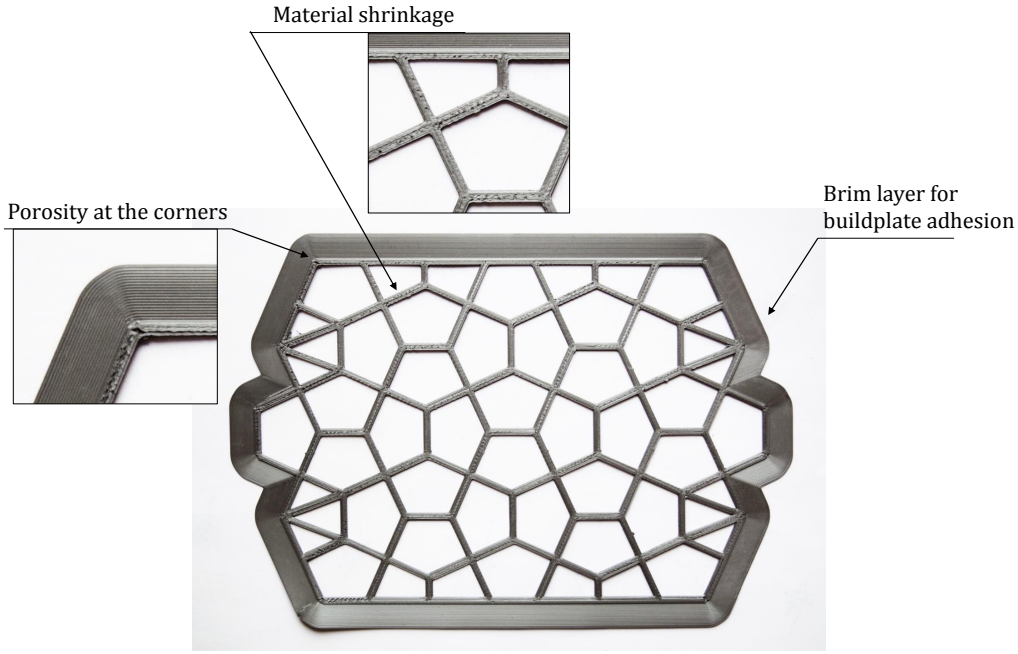

Figure 48: Defects in the 2×3 Cairo lattice at a section of the out-of-plane thickness. The brim layer is not a defect, but enhances the specimen adhesion to the buildplate.

The primary defects faced while manufacturing the Cairo lattice include porosity at the extreme corners of the specimen and the gaps due to the shrinkage of the solid material on cooling as was already seen in the previous sections. These gaps later may act as stress concentration regions when the lattice is loaded. These defects

are shown in Figure 48, which is a section of the out-of-plane thickness of the 2×3 Cairo lattice with patching.

The same defects of porosity were found within the struts of the 1×1 Cairo model due to the shrinkage of the PLA after exiting the heated nozzle (Figure 49). This shrinkage is observed in all the specimens, but are more prominent in the higher relative densities as with the increase in the thickness of the struts, more material is available for shrinkage. It was found with time that these defects though can be lessened, are inevitable with the Ultimaker 3D printers.

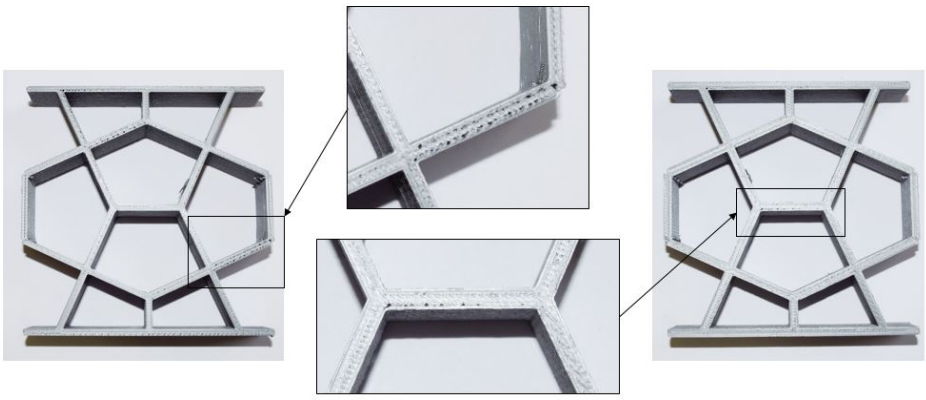

Figure 49: Defects in terms of porosity within the struts for the specimens with a relative density of 0.14 (left) and a relative density of 0.22 (right) for the 1×1 Cairo lattice.

5.5 Summary

The 2×3 Cairo lattice was seen to have a lower strength than the predicted strength. Evidence of macroscopic strain producing mechanisms were found in the deformed lattice from FE analysis as well as from the experiment of this Cairo lattice. The mechanisms that were presented in Section 3.5 are expected to be non-strain producing as it has been seen with the *normalized* strength expression, the *normalized* stiffness expression and their respective FE comparison in Figures 28a and 30, that the infinite lattice behaves *stretching* dominated under pure uni-axial compression. This in turn does not make the lattice itself *stretching* dominated under all loading conditions as Cairo is expected to not have any resistance to shear based on its states of *self-stress*. But even under uni-axial compression, the expected periodic mechanisms are producing macroscopic strains in the finite 2×3 and the 9×10 Cairo lattice primarily due to the lack of periodicity at the free edges.

Although the elastic buckling and the plastic yielding deformation modes were observed in the 1×1 Cairo model, the location of the deformations were affected by the manufacturing defects. The manufacturing process may also affect the response of the lattice by strengthening the PLA by virtue of prolonged heat exposure on the heated bed of the FDM printers. But more investigation is required to arrive

on a definitive conclusion. The slope of the strength plot for the 1×1 model is very similar to analytically predicted strength, essentially presenting the *stretching* dominated behaviour of the Cairo lattice under uni-axial compression. The slope of the experimental stiffness is greater than the analytically predicted stiffness due to the extended upper and lower bars in the experimental model.

A patching scheme can make a finite lattice *statically* and *kinematically* determinate. Instead of the Maxwell's generalized rule for rigidity, an intuitive method was implemented to add the patching bars in the 2×3 Cairo model due to the high number of patch bars suggested by the former method (36 bars). An increase in the strength and the stiffness was observed after patching. Deeper investigation is necessary for the implementation of patching in finite lattices, with a strong mathematical foundation.

6 Discussion

Based on the Maxwell's generalized rule for rigidity which was further modified by Pellegrino and Calladine [7] where it takes into consideration the states of *self stresses* and mechanisms, the *necessary* condition but not the *sufficient* condition for rigidity in case of 2D planar structures, is a connectivity, $Z = 4$. It has been further found that the the *necessary* and the *sufficient* condition for rigidity in 2D frameworks is $Z = 6$ [5]. But such a connectivity rule is until now proven to be valid for *similarly situated* lattices. Even though the Cairo lattice is not a *similarly situated* lattice, but with periodicity it exhibits *stretching* dominated behaviour under purely uni-axial stress fields.

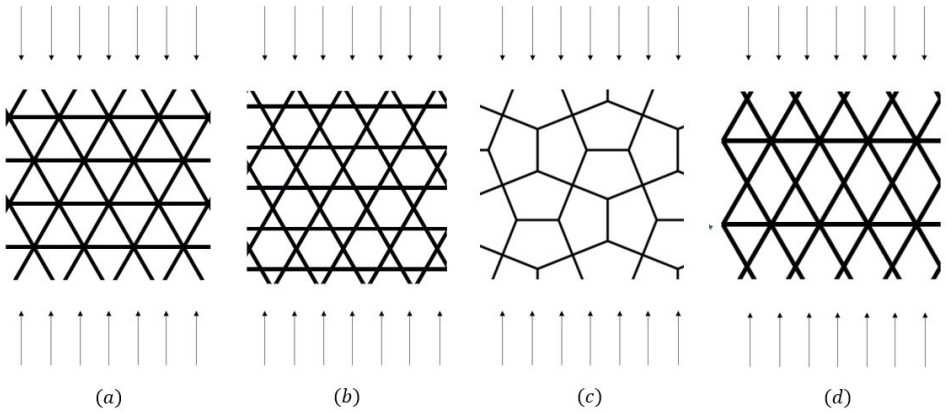

Figure 50: Uni-axial stress field applied to (a) triangular, (b) Kagome, (c) Cairo and (d) diamond lattices.

On comparison with some of the most common *stretching* dominated lattices that are *similar situated* such as the triangular cell, mixed cell, Kagome cell and diamond cell, there are two primary observations, that the Cairo lattice does not have a member which runs throughout the length of the finite lattice and there are no triangulation's as well (Figure 50). The former adds to the rigidity in *stretching* dominated lattices because their main role in the structure is to ensure the integrity of the lattice structure and the latter contributes to the rigidity with the idea that the Maxwell's rule was fundamentally based on the fact that one needs to add two bars and one joint to an already triangulated structure to form a new structure to be *statically* determinate as is expected for stretching dominated lattices. In the absence of these commonly seen features in *stretching* dominated lattices, the Cairo tessellation is certainly unique.

The strength response of the infinite Cairo lattice is compared with the other *stretching* dominated lattices such as triangular, Kagome and diamond for PLA (Figure 51). The plots for the *normalized* strength and *normalized* stiffness for a PLA based Cairo tessellation under periodicity can be seen in Appendix F. It is observed that the elastic buckling response of the Cairo and the Kagome is quite closely matched with the Cairo being stronger by 4.8%. But at relative densities

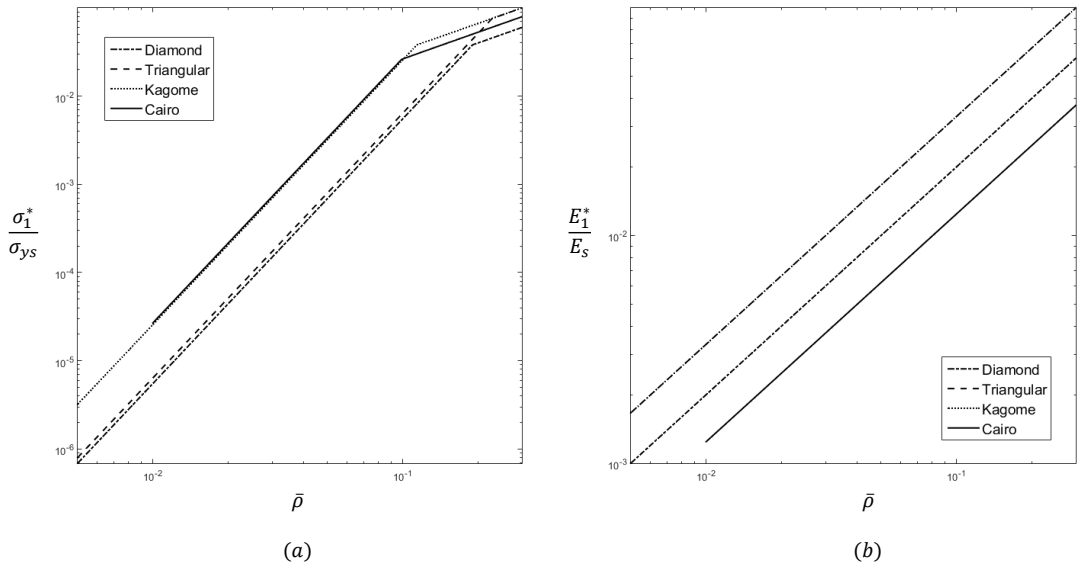

Figure 51: Comparison of the infinite Cairo lattice with infinite diamond, Kagome and triangular lattice for (a) *normalized* strength and (b) *normalized* stiffness.

above the *critical* value, the plastic yielding strength of the Kagome is higher by 20% than the Cairo. Even though the triangular lattice has higher plastic yielding strength than the Cairo, the latter has higher elastic buckling strength by 76%. The Cairo also has higher strength in both the deformation regions than the diamond lattice. In terms of stiffness, the Cairo exhibits the least stiffness among the other three *stretching* dominated tessellations presented here.

But, the three lattices except the Cairo, can truly be considered *stretching* dominated as they are able to take shear along with the uni-axial stress field [1]. On the contrary, the Cairo does not have resistance to shear as was seen in Section 3.5. This makes the Cairo with its two types of nodal connectivity, $Z = 3$ and $Z = 4$, *stretching* dominated only under special cases. Such a behaviour is closely exhibited by the square lattice which is *stretching* dominated only under uni-axial stress field.

The Kagome lattice with $Z = 4$ and has pure periodic mechanisms which makes it *stretching* dominated as it does not produce any macroscopic strains. Whereas, the triangular lattice with $Z = 6$ and has no mechanisms at all which also makes it *stretching* dominated. The triangular-triangular lattice has $Z = 4$ but has strain producing mechanisms, which makes it *bending* dominated. The special cases includes the square and the hexagonal honeycomb with $Z = 4$ and $Z = 3$ respectively, which are classified as the lattices falling in the transition zone. This is because they can collapse either by strain producing mechanisms or periodic mechanisms depending on the external loading condition [28].

The infinite Cairo lattice with dual nodal connectivity has periodic mechanisms under pure uni-axial stress field as the lattice remains *stretching* dominated under such a loading condition, but in finite lattices, the same periodic mechanisms become

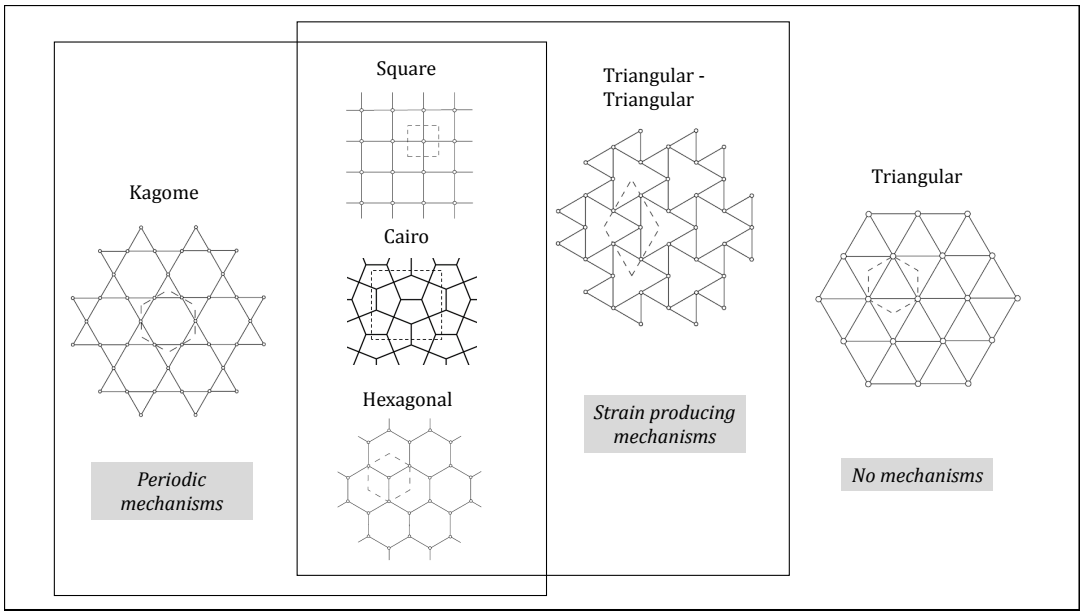

Figure 52: Venn diagram of common planar pin jointed lattices based on the type of mechanisms they induce.

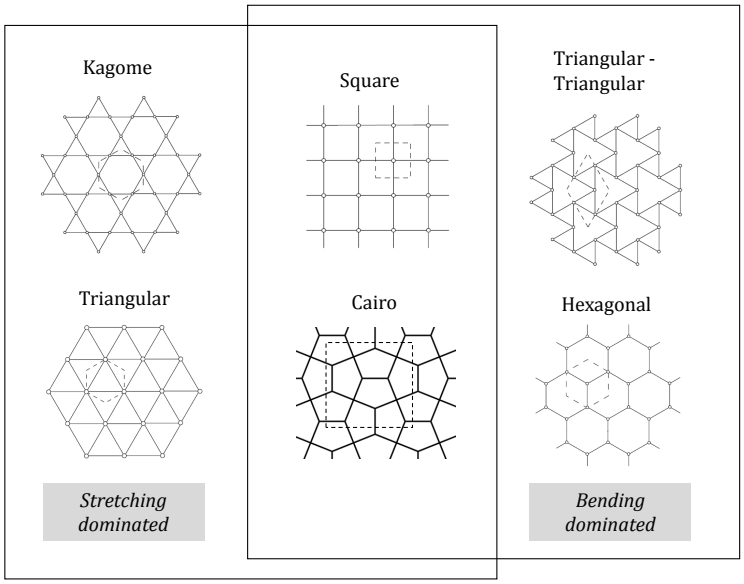

Figure 53: Venn diagram of common planar pin jointed lattices based on the deformation mode.

strain producing mechanism leading to a softened response. If a Venn diagram is proposed, based on the induced mechanism, the Cairo lattice can be positioned in the sub-space for lattices which exhibits both periodic and strain producing mechanism, under the square tessellation (Figure 52). Based on the deformation mode, the Cairo can be categorized in the common space for *stretching* and *bending* dominated lattices (Figure 53). This makes the Cairo a unique tessellation to study further.

7 Conclusion

The Cairo lattice exhibits behaviour quite similar to the square honeycomb lattice, where it is *stretching* dominated only under uni-axial compressive stress field. Under periodicity, the Cairo lattice has a strength similar to the Kagome, as a matter of fact stronger in the elastic buckling region. The Cairo is stronger than the diamond tessellation in both the deformation modes and stronger than the triangular lattice only in the elastic buckling deformation mode. Thus, the infinite Cairo lattice with its two dual nodal connectivity of $Z = 3$ and $Z = 4$ performs on par with the other *stretching* dominated lattices. But it is found to be very difficult to obtain such rigidity in finite Cairo lattices due to the strain producing mechanisms. It can be seen that the rigidity can be regained back by the usage of patch bars. The technique has not been studied extensively for their efficiency, and is a worthy research question on its own.

In this thesis, the mechanics of the Cairo lattice has been developed for its strength and stiffness. The equations for the forces in the struts under uni-axial compression are formulated, the Poisson's ratio defined, the deformation modes of elastic buckling and plastic yielding studied, and a *critical* criterion of the relative density which differentiates the two deformation modes has been established for the Cairo tessellation. FE simulations have been carried out for the Cairo lattice under periodicity and a very good agreement can be found between the analytical and the FE results. But at relative densities higher than 0.1 it is found that the stiffness is influenced by the bending of the struts quite significantly, which currently the mechanics does not take into consideration. The bending behaviour rather presents the Cairo tessellation to be stronger than predicted.

Matrix analysis was implemented to study of the states of *self-stresses* and mechanisms in the Cairo lattice. The infinite Cairo lattice was found to have 2 states of *self-stress* and 4 mechanisms. The former represented the uni-axial stress field that the lattice could sustain, but the lack of the state of *self-stress* for shear makes the Cairo *statically* indeterminate. Among the 4 mechanims, the Cairo lattice has 1 rigid body mechanism and 3 internal mechanisms. The presence of internal mechanisms make the Cairo *kinematically* indeterminate as well. The 2 states of *self-stress* has a stiffening effect on structure such that under uni-axial compression the internal mechanisms are not present in the infinite Cairo lattice, essentially making the lattice *stretching* dominated under such a loading condition. In other words, the internal mechanisms does not lead to macroscopic strains under pure uni-axial compression. But in any other loading condition, the internal mechanisms is expected to induce macroscopic strains and the lattice is then predicted to be *bending* dominated.

But in the finite Cairo lattice, under uni-axial compression, the expected non-strain producing mechanisms are actually leading to macroscopic strains due to the lack of periodicity. Also, the comparison of the FE and experimental results of the 1×1 and 2×3 Cairo lattice showed that the manufacturing time and temperature can have an effect on the strength of the lattice, especially at higher relative densities where the lattice is bound to spend more time on the heated bed of FDM based 3D printers. The increase in the strength of polymers due to the FDM method of

manufacturing is a research topic recommended for further studies.

Cairo with its dual nodal connectivity and the subsequent softening in the finite lattices, can at the present point of time limit its applications until an optimal patching scheme is presented. If the patching scheme implemented is successful, it is expected for the Cairo lattice to be classified as one of the strongest planar tessellations on par with the Kagome and the triangular lattice, thus finding wide applications in the space industry, automobile industry or even in the medical field.

8 Recommendations for future research

Patching scheme

Hutchinson et al. [28] provided a patching scheme for a finite lattice to make it *statically* and *kinematically* determinate. This scheme is based on adding patch bars depending on the number of mechanisms by Maxwell's generalized equation for rigidity. As was seen earlier, with the Cairo lattice it is practically not possible to add the patch bars based on this method because of the huge number of the patching which basically changes the fundamental topology of the Cairo lattice itself. The patching scheme used in this thesis is purely intuitive by observing the motion of the joints in the finite lattice. But further research is definitely recommended to suggest a patching scheme, as a recommendation based on the stiffening effect of the states of *self-stresses* on the mechanisms in the lattice.

Effect of manufacturing time and temperature on the material properties

For FDM as a manufacturing method for lattices, the dependence of the material properties on the time and temperature of manufacturing needs to be investigated. A methodology that can be implemented would be to use the ASTM D638-02a standard for dog-bone specimens printed at various temperatures of the printing bed, preferably above the glass transition temperature. The printing time can also be increased in order to see the prolonged effect of the temperature on the stiffness and the strength of PLA.

Study for determinacy

The matrix method by Pellegrino et al. [7] cannot be readily used for infinite lattices, but can be used to study the finite lattices. There have been methods suggested for repetitive structures based on the matrix analysis itself such as the Bloch's theorem which could be used for the Cairo lattice to further analyze its rigidity [4]. Further, the study on shearing is also recommended to verify the prediction that the Cairo lattice is *bending* dominated under any other loading state than uni-axial stress fields.

References

[1] Wang, A.-J and McDowell, D.L. *In-Plane Stiffness and Yield Strength of Periodic Metal Honeycombs*, Journal of Engineering Materials and Technology 126(2),137-156, 2004.

[2] Fleck, N.A; Deshpande, V.S and Ashby, N.F. *Micro-architectured materials:past, present and future*, Proceedings of the Royal Society 466, 2495-2516, 2010.

[3] Gibson, L.J. *The elastic and plastic behaviour of cellular materials*, PhD Thesis. University of Cambridge, 1981.

[4] Hutchinson, R.G. and Fleck, N. A. *The structural performance of the periodic truss*, Journal of the Mechanics and Physics of Solids 54(4), 756-782, 2006

[5] Deshpande, V. S; Ashby, M. F and Fleck, N. A. *Foam topology bending versus stretching dominated*, Acta Materialia 49(6), 1035-1040, 2001

[6] Maxwell, J. C. *On the calculation of equilibrium and stiffness of frames*, Philosophical Magazine 27(182), 294-299, 1864

[7] Pellegrino, S. and Calladine, C. R. *Matrix analysis of statically and kinematically indeterminate frameworks*, International Journal of Solid Structures 22(4), 409-428, 1985

[8] Guest, S.D and Hutchinson, J. W *On the determinacy of repetitive structures*, Journal of the Mechanics and Physics of Solids 51, 383-391, 2002

[9] Gibson, L.J. and Ashby, N.A. *Cellular solids: Structure and properties*, Cambridge University Press, 1999

[10] Gibson, I.; Rosen, D. and Stucker, B.; *Additive Manufacturing Technologies. 3D Printing, Rapid Prototyping and Direct Digital Manufacturing*, Springer, 2015

[11] Limmahakhun, S.; Oloyede, A.; Sitthiseripratip, K.; Xiao, Y. and Yan, C. *3D-printed cellular structures for bone biomimetic implants*, Additive Manufacturing 15, 93-101, 2017

[12] Comptom, B.G. and Lewis, J.A. *3D-Printing of Lightweight Cellular Composites*, Journal of Advanced Materials 26(34), 5930-5935, 2014

[13] Park, S.; Rosen, D.W.; Choi, S. and Duty, C.E. *Effective mechanical properties of lattice material fabricated by material extrusion additive manufacturing*, Additive Manufacturing 1-4, 12-13, 2014

[14] Cahill, S.; Lohfeld, S. and McHugh, P.E. *Finite element predictions compared to experimental results for the effective modulus of bone tissue engineering scaffolds fabricated by selective laser sintering*, Journal of Materials Science: Materials in Medicine 20(6), 1255-1262, 2009

[15] Maurath, J. and Willenbacher, N. *3D printing of open-porous cellular ceramics with high specific strength*, Journal of the European Ceramic Society 37(15), 4833-4842, 2017

[16] Pellegrino. S *Structural Computations with the Singular Value Decomposition of the Equilibrium Matrix*, International Journal of Solid Structures, Vol. 30, No. 21, pp. 3025-3035, 1993

[17] Ashby, M.F *Materials selection in mechanical design*, Elsevier Butterworth-Heinemann 2011. 4th ed

[18] Ashby, M.F *The properties of foams and lattices*, Philosophical Transactions of The Royal Society - Mathematical, Physical and Engineering Sciences 364(1838), 15-30, 2005

[19] ASTM Standard D638-02a, 2002, *Standard Test Method for Tensile Properties of Plastics*, ASTM International, 2003

[20] Manfredi, N. *Lightweight Structures: topology optimization and 3D printing*, Laurea Magistrale Thesis, University of Pavia, 2015

[21] Christensen, R.M. *Mechanics of cellular and other low-density materials*, International Journal of Solids and Structures 37(1-2), 91-104, 2000

[22] Overaker, D.W.; Cuitiño, A.M. and Langrana, N.A. *Effects of morphology and orientation on the behavior of two-dimensional hexagonal foams and application in a re-entrant foam anchor model*, Mechanics of Materials 29(1), 43-52, 1998

[23] Ashby, M.F.; Mehl Medalist, R.F. *The mechanical properties of cellular solids*, Metallurgical and Materials Transactions A 14(9), 1755-1769, 1983

[24] Grenestedt, J.L. *Influence of wavy imperfections in cell walls on elastic stiffness of cellular solids*, Journal of the Mechanics and Physics of Solids 46(1), 29-50, 1998

[25] Warren, W.E. and Kraynik, A.M. *Foam Mechanics: The Linear Elastic Response of Two-Dimensional Spatially Periodic Cellular Materials*, Mechanics of Materials 6(1), 27-37, 1987

[26] Chen, D.H. and Yang, L. *Analysis of equivalent elastic modulus of asymmetrical honeycomb*, Composite Structures 93(2), 767-773, 2011

[27] Gibson, L.J.; Ashby, M.F.; Schajer, G.S. and Robertson, C.I. *The mechanics of two-dimensional cellular materials*, Proceedings of the Royal Society A - Mathematical, Physical and Engineering Sciences 382(1782), 25-42, 1982.

[28] Hutchinson, R.G. and Fleck, N.A. *Microarchitectured cellular solids – the hunt for statically determinate periodic trusses*, Plenary lecture presented at the 75th Annual GAMM Conference, Dresden, Germany, 22–26 March 2004

[29] Deshpande, V.S.; Fleck, N.A. and Ashby, M.F. *Effective properties of the octet-truss lattice material*, Journal of the Mechanics and Physics of Solids 49(8), 1747-1769, 2001

[30] Tantikom, K.; Suwa, Y. and Aizawa, T. *In-Plane Compression Response of Regularly Cell-Structured Materials*, Materials Transactions 45, 509-515, 2003

[31] Elsayed, M.S.A *Multiscale Mechanics and Structural Design of Periodic Cellular Materials*, PhD thesis, McGill University, 2010

[32] Phani, S.A. and Fleck, N.A. *Elastic Boundary Layers in Two-Dimensional Isotropic Lattices*, Journal of Applied Mechanics 75(2), 2008

[33] Zhang, Y.H.; Qiu, X.M. and Fang, D.N. *Mechanical Properties of two novel planar lattice structures*, International Journal of Solids and Structures 45(13), 3751-3768, 2008

[34] Chen, D. and Ushijima, K. *Deformation of Honeycomb with Finite Boundary Subjected to Uniaxial Compression*, Metals 3(4), 343-360, 2013

[35] Tankasala, H.C.; Deshpande, V.S. and Fleck, N.A. *Tensile response of elasto-plastic lattices at finite strain*, Journal of the Mechanics and Physics of Solids, 2017

[36] Chen, C.; Lu, T.J. and Fleck, N.A. *Effect of imperfections on the yielding of two-dimensional foams*, Journal of the Mechanics and Physics of Solids 47(11), 2235-2272, 1999

[37] Lockerbie, J. *Arabic/Islamic geometry 02 [online]*, viewed on 12 August 2017, Available at: http://catnaps.org/islamic/geometry2.html

[38] Fuller, R.B. *US Patent 3 063 521 Tensile Integrity Structures*, United States Patent Office, 1962

[39] Calladine, C.R. *Buckminster Fuller's "Tensegrity" Structures and Clerk Maxwell's Rules for the Constructure of Stiff Frames*, Internaltion Journal Solids Structures 14(2), 161-172, 1978

[40] *Polylactic acid [online]*, viewed on 20 August 2017, Available at: https://en.wikipedia.org/wiki/Polylactic_acid

[41] Srithep, Y.; Nealey, P. and Turng, L *Effects of Annealing Time and Temperature on the Crystallinity and Heat Resistance Behavior of Injection-Molded Poly(lactic acid)*, Polymer Engineering and Science 53(3), 580-588, 2013

[42] Chopra, P. *Effective Mechanical Properties of Lattice Materials*, M.Sc Thesis, The University of British Columbia, 2011

[43] Torquota, S.; Gibiansky, L.V.; Silva, M.J. and Gibson, L.J. *Effective mechanical and transport properties of cellular solids*, International Journal of Mechanical Sciences 40(1), 71-82, 1998

A Method of joints for member forces in Cairo

For determining the forces, the two equilibrium equations ($\Sigma F_1 = 0$ & $\Sigma F_2 = 0$) are considered at certain nodes as well as for the entire unit cell. As the truss is expected to only take axial forces, the third equilibrium equation $\Sigma M = 0$ for the moments is not taken into consideration. The stress field is considered to be along the X1 direction.

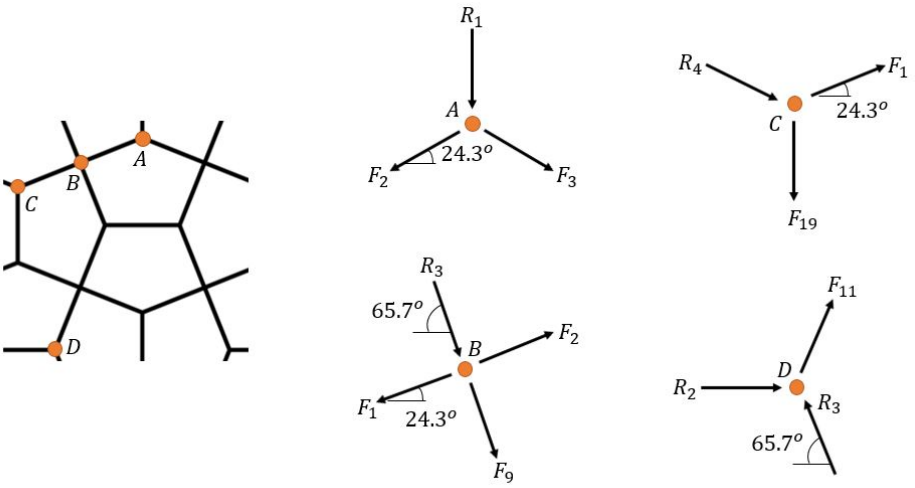

Figure A1: Reactions at Nodes A, B, C and D.

Initially with reference to Figure A1, *Node A* is considered. The equilibrium equations at that node are,

$$R_1 = -2 \cdot T_I \cdot sin(24.3) \tag{A1}$$

$$R_1 = -T_{IV} \tag{A2}$$

Equation A1 is obtained from the vertical equilibrium reaction. The horizontal equilibrium is not possible at this node. Equation A2 is based on the fact that reaction R_1 and the members with the force T_{IV} are identical.

From Equation A1 and Equation A2, we have,

$$T_{IV} = 2 \cdot T_I \cdot sin(24.3) \tag{A3}$$

Considering *Node B*, the vertical equilibrium equation leads to,

$$R_3 = -T_{II} \tag{A4}$$

Similarly, the reactions at *Node C* and *Node D* are,

$$R_4 = -T_I \tag{A5}$$

$$R_4 = -\frac{T_{IV}}{2 \cdot sin(24.3)} \tag{A6}$$

$$R_2 = -2 \cdot T_{II} \cdot cos(65.7) \tag{A7}$$

$$R_2 = -T_{III} \tag{A8}$$

From Equation A7 and Equation A8, we have,

$$T_{III} = 2 \cdot T_{II} \cdot cos(65.7) \tag{A9}$$

The horizontal equilibrium equation for the entire unit cell is given by,

$$R_2 + 2 \cdot R_4 \cdot cos(24.3) = 0 \tag{A10}$$

Substituting Equation A7 and Equation A6 in the above equation, we have

$$-2 \cdot T_{II} \cdot cos(65.7) - \frac{T_{IV}}{sin(24.3)} \cdot cos(24.3) = 0 \tag{A11}$$

Substituting Equation A3 in Equation A11,

$$-T_{II} \cdot cos(65.7) - T_I \cdot cos(24.3) = 0 \tag{A12}$$

The vertical equilibrium equation for the entire unit cell is given by,

$$R_1 + 2 \cdot R_3 \cdot sin(65.7) = (4lcos(24.3)) \cdot h\sigma_1 \tag{A13}$$

The right hand side term in Equation A13 is the force in the unit cell due to the stress field σ_1 along the X1 direction.

From substituting Equation A1 and Equation A4 into Equation A13, we have,

$$-T_I \cdot sin(24.3) - T_{II} \cdot sin(65.7) = 2lh - lcos(24.3) \cdot \sigma_1 \tag{A14}$$

From Equation A12, Equation A14,

$$T_I = 1.1342lh\sigma_1 \tag{A15}$$

$$T_{II} = -2.512lh\sigma_1 \tag{A16}$$

And from Equation A9 and Equation A16,

$$T_{III} = -2.0674lh\sigma_1 \tag{A17}$$

From Equation A3 and Equation A15,

$$T_{IV} = 0.9335lh\sigma_1 \tag{A18}$$

B Virtual work for truss deflections

Based on the principal of virtual forces, the total external work is equal to the total internal work for every system of virtual forces and stresses that satisfy the equilibrium equation,

$$\Sigma \delta F_i u_i = \int \delta \sigma_{ij} \epsilon_{ij} dv \tag{B1}$$

where, $\delta\sigma_{ij}$ are the virtual stresses caused due to the virtual forces δF_i. And, ϵ_{ij} are the true strains due to the displacements u_i.

The unit load method based on the principal of virtual forces is employed in this thesis to calculate the stiffness of the Cairo lattice analytically. Under the action of a system of forces $F_1, F_2, \ldots, F_n$ and another system of virtual forces $\delta F_1, \delta F_2, \ldots, \delta F_n$ leading to displacements $u_1, u_2, \ldots, u_n$ and virtual displacements $\delta u_1, \delta u_2, \ldots, \delta u_n$ respectively, for a cantilever beam as an example, the above equilibrium equation can be written as,

$$\frac{1}{2}\sum_{i=1}^{n} F_i u_i = \int_0^L \frac{P^2 ds}{2EA} + \int_0^L \frac{M^2 ds}{2EI} + \int_0^L \frac{V^2 ds}{2AG} \tag{B2}$$

$$\frac{1}{2}\sum_{i=1}^{n} \delta F_i \delta u_i = \int_0^L \frac{\delta P_v^2 ds}{2EA} + \int_0^L \frac{\delta M_v^2 ds}{2EI} + \int_0^L \frac{\delta V_v^2 ds}{2AG} \tag{B3}$$

Where, P, M, V, δP_v, δM_v and δV_v are the axial force, bending moment, shearing force, virtual axial force, virtual bending moment and virtual shearing force respectively. Also, E, A, G and I represent the modulus of elasticity, cross-sectional area, shear modulus and moment of inertia respectively. The elemental length of the beam is given as ds.

The *principal of superposition* states that the deflection at a point in a structure when produced by several loads acting simultaneously can be determined by superimposing deflections at the same point produced by loads acting individually. By the usage of *conservation of energy*, a term $\sum_{j=1}^{n} \delta F_i u_i$ which represents the work done by virtual forces leading to real displacements, is added to the principal of superposition. Subtracting the resulting equation from Equation B2 and Equation B3, gives us,

$$\sum_{j=1}^{n} \delta F_i u_i = \int_0^L \frac{\delta P_v P ds}{EA} + \int_0^L \frac{\delta M_v M ds}{EI} + \int_0^L \frac{\delta V_v V ds}{AG} \tag{B4}$$

For plane trusses, the internal forces are axial. Therefore Equation B4 can be re-written as,

$$\sum_{j=1}^{n} \delta F_i u_i = \int_0^L \frac{\delta P_v P ds}{EA} \tag{B5}$$

If the cross-sectional area remains constant and on the application of a unit virtual load, Equation B5 can be re-arranged as,

$$u_j = \sum_{i=1}^{m} \frac{(\delta P_v)_{ij} P_i L_i}{E_i A_i} \tag{B6}$$

where m is the number of members.

C Virtual work for Cairo unit cell (X1 direction)

Member	**Virtual Load** $(\delta P_v)_i$	**Actual Load** P_i	$\frac{L_i}{A_i E_i}$	$\frac{(\delta P_v)_i P_i L_i}{E_i A_i}$
AB	0.31114	$1.1342 \cdot lh\sigma_1$	$\frac{l}{AE_s}$	$0.352895 \frac{h\sigma_1 l^2}{AE_s}$
BC	0.31114	$1.1342 \cdot lh\sigma_1$	$\frac{l}{AE_s}$	$0.352895 \frac{h\sigma_1 l^2}{AE_s}$
CD	0.31114	$1.1342 \cdot lh\sigma_1$	$\frac{l}{AE_s}$	$0.352895 \frac{h\sigma_1 l^2}{AE_s}$
DA	0.31114	$1.1342 \cdot lh\sigma_1$	$\frac{l}{AE_s}$	$0.352895 \frac{h\sigma_1 l^2}{AE_s}$
LG	0.31114	$1.1342 \cdot lh\sigma_1$	$\frac{l}{AE_s}$	$0.352895 \frac{h\sigma_1 l^2}{AE_s}$
GH	0.31114	$1.1342 \cdot lh\sigma_1$	$\frac{l}{AE_s}$	$0.352895 \frac{h\sigma_1 l^2}{AE_s}$
HI	0.31114	$1.1342 \cdot lh\sigma_1$	$\frac{l}{AE_s}$	$0.352895 \frac{h\sigma_1 l^2}{AE_s}$
IL	0.31114	$1.1342 \cdot lh\sigma_1$	$\frac{l}{AE_s}$	$0.352895 \frac{h\sigma_1 l^2}{AE_s}$
BE	-0.6891	$-2.512 \cdot lh\sigma_1$	$\frac{l}{AE_s}$	$1.731019 \frac{h\sigma_1 l^2}{AE_s}$
EG	-0.6891	$-2.512 \cdot lh\sigma_1$	$\frac{l}{AE_s}$	$1.731019 \frac{h\sigma_1 l^2}{AE_s}$
GK	-0.6891	$-2.512 \cdot lh\sigma_1$	$\frac{l}{AE_s}$	$1.731019 \frac{h\sigma_1 l^2}{AE_s}$
KB	-0.6891	$-2.512 \cdot lh\sigma_1$	$\frac{l}{AE_s}$	$1.731019 \frac{h\sigma_1 l^2}{AE_s}$
DF	-0.6891	$-2.512 \cdot lh\sigma_1$	$\frac{l}{AE_s}$	$1.731019 \frac{h\sigma_1 l^2}{AE_s}$
FI	-0.6891	$-2.512 \cdot lh\sigma_1$	$\frac{l}{AE_s}$	$1.731019 \frac{h\sigma_1 l^2}{AE_s}$
IJ	-0.6891	$-2.512 \cdot lh\sigma_1$	$\frac{l}{AE_s}$	$1.731019 \frac{h\sigma_1 l^2}{AE_s}$
JD	-0.6891	$-2.512 \cdot lh\sigma_1$	$\frac{l}{AE_s}$	$1.731019 \frac{h\sigma_1 l^2}{AE_s}$
AL	0.25607	$0.9335 \cdot lh\sigma_1$	$\frac{l}{AE_s}$	$0.239041 \frac{h\sigma_1 l^2}{AE_s}$
HC	0.25607	$0.9335 \cdot lh\sigma_1$	$\frac{l}{AE_s}$	$0.239041 \frac{h\sigma_1 l^2}{AE_s}$
EF	-0.56715	$-2.0674 \cdot lh\sigma_1$	$\frac{l}{AE_s}$	$1.172526 \frac{h\sigma_1 l^2}{AE_s}$
JK	-0.56715	$-2.0674 \cdot lh\sigma_1$	$\frac{l}{AE_s}$	$1.172526 \frac{h\sigma_1 l^2}{AE_s}$
$\sum$				$19.49445 \frac{h\sigma_1 l^2}{AE_s}$

Table C1: Virtual work method for determination of displacement in X1 direction. The virtual load is computed using the force equation described in Appendix A when subjected to a unity force.

D Virtual work for Cairo unit cell (X2 direction)

Member	**Virtual Load** $(\delta P_v)_i$	**Actual Load** P_i	$\frac{L_i}{A_i E_i}$	$\frac{(\delta P_v)_i P_i L_i}{E_i A_i}$
AB	-0.6891	$1.1342 \cdot lh\sigma_1$	$\frac{l}{AE_s}$	$-0.78158\frac{h\sigma_1 l^2}{AE_s}$
BC	-0.6891	$1.1342 \cdot lh\sigma_1$	$\frac{l}{AE_s}$	$-0.78158\frac{h\sigma_1 l^2}{AE_s}$
CD	-0.6891	$1.1342 \cdot lh\sigma_1$	$\frac{l}{AE_s}$	$-0.78158\frac{h\sigma_1 l^2}{AE_s}$
DA	-0.6891	$1.1342 \cdot lh\sigma_1$	$\frac{l}{AE_s}$	$-0.78158\frac{h\sigma_1 l^2}{AE_s}$
LG	-0.6891	$1.1342 \cdot lh\sigma_1$	$\frac{l}{AE_s}$	$-0.78158\frac{h\sigma_1 l^2}{AE_s}$
GH	-0.6891	$1.1342 \cdot lh\sigma_1$	$\frac{l}{AE_s}$	$-0.78158\frac{h\sigma_1 l^2}{AE_s}$
HI	-0.6891	$1.1342 \cdot lh\sigma_1$	$\frac{l}{AE_s}$	$-0.78158\frac{h\sigma_1 l^2}{AE_s}$
IL	-0.6891	$1.1342 \cdot lh\sigma_1$	$\frac{l}{AE_s}$	$-0.78158\frac{h\sigma_1 l^2}{AE_s}$
BE	0.31114	$-2.512 \cdot lh\sigma_1$	$\frac{l}{AE_s}$	$-0.78158\frac{h\sigma_1 l^2}{AE_s}$
EG	0.31114	$-2.512 \cdot lh\sigma_1$	$\frac{l}{AE_s}$	$-0.78158\frac{h\sigma_1 l^2}{AE_s}$
GK	0.31114	$-2.512 \cdot lh\sigma_1$	$\frac{l}{AE_s}$	$-0.78158\frac{h\sigma_1 l^2}{AE_s}$
KB	0.31114	$-2.512 \cdot lh\sigma_1$	$\frac{l}{AE_s}$	$-0.78158\frac{h\sigma_1 l^2}{AE_s}$
DF	0.31114	$-2.512 \cdot lh\sigma_1$	$\frac{l}{AE_s}$	$-0.78158\frac{h\sigma_1 l^2}{AE_s}$
FI	0.31114	$-2.512 \cdot lh\sigma_1$	$\frac{l}{AE_s}$	$-0.78158\frac{h\sigma_1 l^2}{AE_s}$
IJ	0.31114	$-2.512 \cdot lh\sigma_1$	$\frac{l}{AE_s}$	$-0.78158\frac{h\sigma_1 l^2}{AE_s}$
JD	0.31114	$-2.512 \cdot lh\sigma_1$	$\frac{l}{AE_s}$	$-0.78158\frac{h\sigma_1 l^2}{AE_s}$
AL	-0.56715	$0.9335 \cdot lh\sigma_1$	$\frac{l}{AE_s}$	$-0.52943\frac{h\sigma_1 l^2}{AE_s}$
HC	-0.56715	$0.9335 \cdot lh\sigma_1$	$\frac{l}{AE_s}$	$-0.52943\frac{h\sigma_1 l^2}{AE_s}$
EF	0.25607	$-2.0674 \cdot lh\sigma_1$	$\frac{l}{AE_s}$	$-0.5294\frac{h\sigma_1 l^2}{AE_s}$
JK	0.25607	$-2.0674 \cdot lh\sigma_1$	$\frac{l}{AE_s}$	$-0.5294\frac{h\sigma_1 l^2}{AE_s}$
$\sum$				$-14.623\frac{h\sigma_1 l^2}{AE_s}$

Table D1: Virtual work method for determination of displacement in X2 direction. The virtual load is computed using the force equation described in Appendix A when subjected to a unity force.

E Determination of material properties for PLA

Before the experiments are carried out and compared with the FE results, it is imperative to first acquire the correct material properties of the PLA used in this thesis, as the properties vary slightly depending on the variation of the manufacturing process. The ASTM standard D638-02a is used for determining the tensile properties of polymers [19]. The dog-bone specimen is shown in Figure E1.

Figure E1: Dog-bone specimen according to ASTM D638-02a [19]

The dog-bone specimens are printed using the Ultimaker 2 Extended. The build-plate temperature was set to 60°C and the temperature of the nozzle was 220°C. The infill density had been set to 100%. A total of 5 specimens were printed. The cross-sectional areas are measured with a vernier caliper and it was observed that for a specimen printed using the Ultimaker, warping and contraction of the polymer after the heated bed is cooled, leads to differences of about 1% - 2% in measurement. The result of these differences is reflected in the engineering stress-strain plot for all the 5 specimens as seen in Figure E2. The dog-bone specimens were subjected to a strain rate of 0.001 s^{-1}. From the experiments, the average yield strength is 43.72 MPa and the average Youngs modulus is 3057.51 MPa.

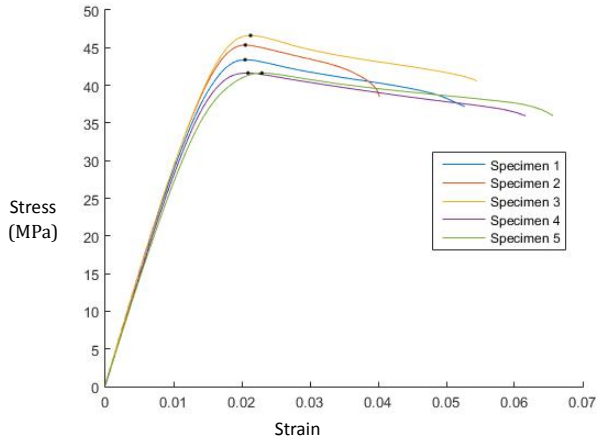

Figure E2: Stress-strain response of the 5 dog-bone specimens. The black dot represents the yielding strength considered for the specimen in accordance with the measurement recommendation made in the ASTM standard.

F Non-linear FE analysis of a PLA based Cairo unit cell

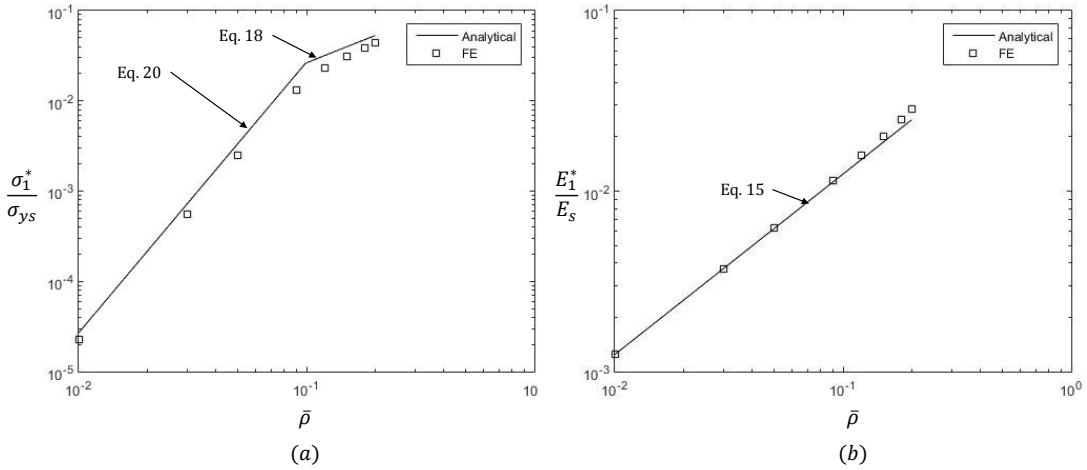

Figure F1: Analytical and FE comparison of the infinite Cairo lattice made from PLA for (a) Stiffness and (b) Strength.

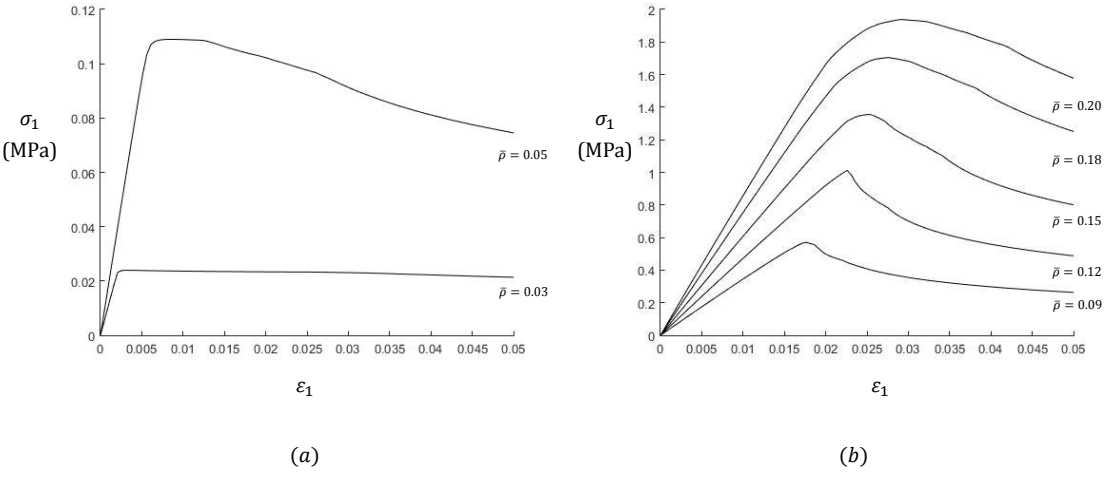

Figure F2: Stress strain response of a PLA based Cairo lattice with relative densities (a) 0.03, 0.05 (b) 0.09, 0.12, 0.15, 0.18, 0.20.

PLA is a biodegrable plastic as it is derived from natural resources such as corn starch and sugar cane. In the 3D printing community, they are widely used due to their low cost of manufacturing - making PLA one of the highest produced bioplastic. The melting temperature of PLA is around 173°C - 178°C, but has a fairly low glass transition temperature of about 60°C - 65°C [40].

The material properties of the PLA used for making the experimental specimens has been obtained in Appendix E. The material is linear elastic and perfectly plastic in nature. The boundary conditions and the loading conditions remain the same as with the unit cell analyzed in Chapter 4. The comparative plot for the FE and the analytical solution for stiffness and strength is shown in Figure F1. Also, the stress strain response of the various relative densities are shown in Figure F2. The *critical* relative density is 0.099 when the infinite Cairo lattice is made from PLA.

G Non-linear FE set-up for 2×3 Cairo lattice

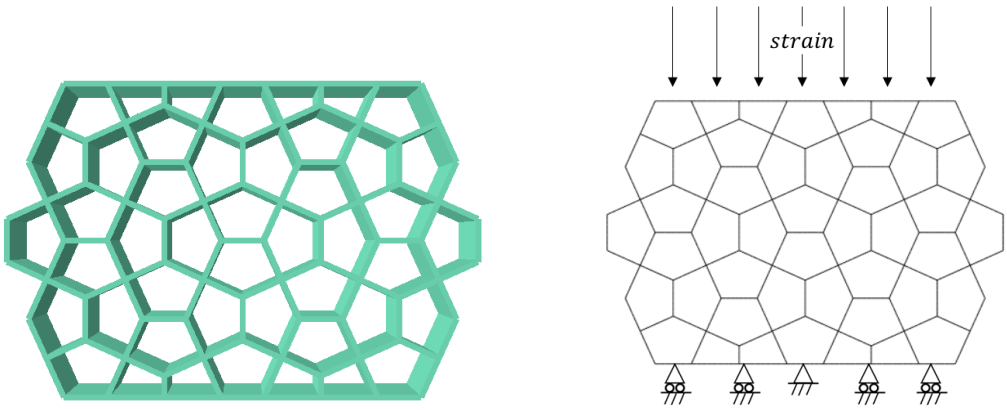

Figure G1: (a) The 2×3 Cairo lattice; (b) Boundary conditions for 2×3 Cairo lattice.

The 2×3 Cairo lattice (Figure G1a) has a relative density of 0.2, with a strut length of 15 mm and an out-of-plane thickness of 30 mm. The higher out of plane thickness was selected to ensure that the dominant deformation mode is not out-of-plane buckling during the experimental tests.

The boundary conditions are seen in Figure G1b where the base of the lattice is allowed to move in the horizontal direction with the central node fixed to avoid any rigid body motion. The loading is applied under displacement control.

The Standard solver of the Abaqus CAE 6.14 software is used again for this analysis with NLGEOM. The yield strength and the Young's modulus are taken as 43.72 MPa and 3057.508 MPa respectively. The determination of the material properties for PLA can be found in Appendix E.

H Non-linear FE set-up for 1×1 Cairo lattice

The notation 1×1 basically implies that the lattice has just 1 column and 1 row of the unit cell. This lattice is a physical significance of a unit cell mainly created to observe the elastic buckling and plastic yielding deformation mode in the highest stressed members.

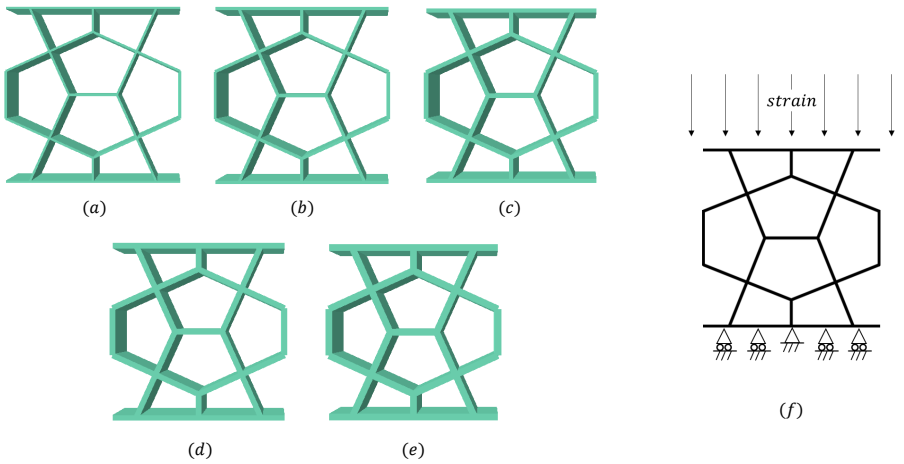

Figure H1: FE model for the 1×1 Cairo with relative densities (a) 0.07 (b) 0.1 (c) 0.14 (d) 0.18 and (e) 0.22 (f); Boundary conditions for the FE model.

The relative densities of 0.07, 0.1, 0.14, 0.18 and 0.22 respectively has been modelled with the thicknesses of the struts as 1.1631 mm, 1.6618 mm, 2.3262 mm, 2.9908 mm and 3.6554 mm respectively. These relative densities along with their boundary condition selected for this analysis are shown in Figure H1. For avoiding rigid body motions, the horizontal motion for the central node of the base has been restricted. The extended upper and lower walls which other wise are not present in the Cairo tessellation serve two purposes - to provide the lateral resistance to motion as would have been experienced by the unit cell under periodicity and to ensure that the maximum stress is generated in the inclined members carrying T_{II} force.

The material properties for the PLA used for manufacturing the specimens is taken from Appendix E. The out-of-plane thickness has been set as 20 mm in order to prevent out-of-plane buckling during the experiments. The length of each strut is 25 mm. The size of the specimen is 91.12 mm $\times$ 91.12 mm. The Standard solver of the Abaqus CAE software with NLGEOM has been used for this analysis. The solver follows the Newton-Raphson's method to determine the expected load-displacement response.

I Non-linear FE set-up for 2×3 Cairo lattice with patching

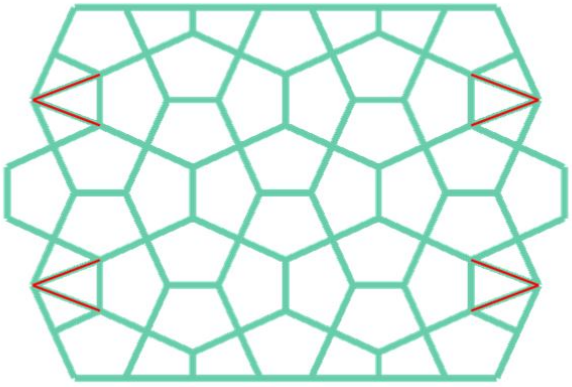

Figure I1: FE model of patch bars (red) added to the 2×3 lattice intuitively.

The 2×3 Cairo lattice with patch bars (Figure I1a) has the same relative density of 0.2 as the model without patch bars. The strut length is kept 15 mm and the size of the entire lattice remains unchanged. The thickness of the patch bars is the same as the thickness of the other struts. The out-of-plane thickness, material properties, loading condition and the boundary conditions are the same as was applied in Appendix G for the 2×3 Cairo lattice without patch bars. The solver used is again Abaqus Standard with NLGEOM.